Université de Lille 1 Sciences et Technologies
Laboratoire de Mécanique de Lille (UMR CNRS 8107)
Ecole Doctorale SPI Lille Nord-de-France
Année 2015-N^{o} d'ordre: 41761

THESE

pour obtenir le grade de
Docteur de L'Université de Lille 1 Sciences et Technologies

Discipline: Génie Civil
Présentée par

Mingyao LI

Contribution à la modélisation multi-échelle du comportement mécanique des matériaux rocheux

Soutenue publiquement le 29 Juin 2015
devant le jury composé de

A. GIRAUD	Professeur Université de Lorraine	Rapporteur
D. LYDZBA	Professeur Université Polytechnique Wroclaw Pologne	Rapporteur
JB. COLLIAT	Professeur Université Lille 1	Examinateur
D. KONDO	Professeur Université Paris 6	Examinateur
W.Q. SHEN	Maîtres de conférences Université Lille 1	Co-encadrant
J.F. SHAO	Professeur Université Lille 1	Directeur de thése

I would like to dedicate this thesis to

my loving parents

Acknowledgements

The accomplishment of this dissertation would not have been possible without the help and support from some very special people during my doctoral studies at Laboratoire de Méchanique de Lille (LML) in Université de Lille 1.

I would like firstly to express my gratefully and sincerely gratitude to my advisor, Professor Jianfu Shao, for his invaluable guidance, helpful suggestions and patience during my entire research. Fruitful suggestions always motivated me to research more deeply and further, and it is a great honor for me to be one of his students.

I would also like to acknowledge my co-encadrant, Dr. Wanqing Shen, for his helpful guidance and discussion to enable me to develop an deep understanding of many subjects and to advance my research, and most importantly for his friendship.

I am deeply grateful for the comments and modifications from Professor Albert Giraud, Professor Darusz Lydzba as the reviewers of the manuscript of my dissertation. My sincerely gratitude goes to Professor Djimédo Kondo as the president and Professor Jean-Baptiste Colliat as the member of the defense jury.

Great thanks also goes to my colleagues in my laboratory for their assistance and enlightening conversations during my doctoral research. They are Dr. Jia Yun, Dr. Bian Hanbing, and Dr. Xie Shouyi for all the kind help and valuable advice. It is my pleasure to work with Dr. Liu Zaobao, Dr. Zhang Yu, Dr. Zheng Lifeng in the same office and thanks for their help and memorable conversations for these years. I would also thank to Dr. Cheng Long, Wu Qier, Yao Chi, Zeng Tao, Qi Mei, Liu Lin, Ghorbanbeigi Hamid ...

Special thanks to Mr. Matthieu Marquillie for his help of the optimization on my numerical codes with parallel computing and computational assistance.

Finally, I owe a great deal of appreciation to my parents for their unconditional support and encouragement during my academic career. Their enduring love and confidence in me have been my source of strength.

Abstract

The objective of this work is to study the effects of microstructures on the macroscopic mechanical behaviors of heterogeneous geomaterials. Taking advantage of the Fast Fourier Transforms (FFT) based numerical method, the complex microstructures of geomaterials can be considered as close as possible to the real microstructure and a full field micromechanical analysis of strain and stress can be provided at the microscopic scale. This feature overcomes the strong assumptions on microstructure by traditional homogenization approaches. Matrix-inclusion type composites with different microstructure are firstly investigated. The influences of inclusion shape, size, distribution and orientation on the effective behavior are fully studied. Then it is applied to the Callovo-Oxfordian argillite which is modeled as an elastoplastic matrix reinforced by linear elastic quartz and calcite spherical grains. With a non-associated plastic flow rule in the matrix, the effects of mineral grains are explicitly taken into account. The model is further extended by introducing the progressive damage process due to the growth of microcracks. After that, the pore effects (shapes, sizes, orientations and distributions) on the effective behavior of porous materials are considered with a specific application to the typical porous geomaterial sandstone. Furthermore, the deterioration around the pores and the interacted regions are simulated with a simple damage criterion for pore evolution and the degradation phenomenon is fully exhibited. The comparisons between the numerical results and experimental data verify the efficiency and accuracy of the FFT based method for heterogeneous geomaterials.

Keywords: Homogenization, Fast Fourier Transform, Plasticity, Damage, Clayed rocks, Heterogeneous materials

Résumé

L'objectif de ce travail est d'étudier les effets de microstructures sur les comportements mécaniques macroscopiques des géomatériaux hétérogènes. Profitant de la méthode numérique basée sur la Transformée de Fourier Rapide (TFR), les microstructures complexes de géomatériaux peuvent être simulées aussi proche que possible de la vraie microstructure. Avec des calculs en champ complet, les contraintes et les déformations locales sont fournies à l'échelle microscopique. Cette caractéristique permet de surmonter les hypothèses fortes sur la microstructure par des approches traditionnelles d'homogénéisation. Matrix-inclusion composites avec microstructures différentes sont d'abord étudiés. Les influences de la forme, la taille, la distribution et l'orientation des inclusions sur le comportement macroscopique sont prises en compte. Ensuite, ce modèle numérique basé sur TFR est appliqué à l'argilite du Callovo-Oxfordien qui est traitée comme une matrice élastoplastique renforcé par des grains élastiques de quartz et de calcite. Avec une règle d'écoulement non associé dans la matrice, les effets de grains sphériques de minéraux sont explicitement pris en compte. Ce modèle est en outre étendu par la considération du processus de détérioration progressive due à la croissance de microfissures. Après cela, les effets de pores (formes, tailles, orientations et distributions) sur le comportement effectif de matériaux poreux sont considérés. A titre d'exemple, un géomatériau poreuse typique-grès a été étudié en détail. En outre, la détérioration autour des pores et des régions interagies sont simulées avec un critère simple d'endommagement pour l'évolution des pores et le phènomène de dégradation est entièrement exposé. Les comparaisons entre les résultats numériques et les données expérimentales vérifient l'efficacité et la précision de cette méthode numérique basée sur TFR pour les géomatériaux hétérogènes.

Mots-clés: Homogénéisation, Transformation de Fourier rapide, plasticité, Endommagement, Argillite, matériaux hétérogènes

General introduction

During last decades, the heterogeneous geomaterials (soils, rocks, cementitious materials) have been widely used and studied in many engineering structures. For example, clayey rocks have been extensively investigated in many countries as a potential geological barrier for underground radioactive waste disposal and sequestration of residual gas. Clayey rocks also constitute the cap rock of many oil and gas reservoirs. On the other hand, shales are investigated as reservoir rocks for the optimal exploration of shale gas. In all these applications, it is crucial to characterize and describe both short and long term hydromechanical behaviors of clayey rocks, in particular plastic deformation, damage process and pore evolution as well as permeability evolution. As a representative clayey rock, extensive laboratory studies have been conducted on the Callovo-Oxfordian (COX) claystone from the underground research laboratory of Andra, the French National Agency for radioactive waste management (Andra, 2005, 2012). Basically, the inelastic mechanical behaviors of the COX claystone can be characterized by the plastic deformation and microcrack induced damage in the clay matrix and at interfaces. The macroscopic responses are strongly influenced by its mineral compositions and the water saturation degree due to the presence of swelling clay minerals such as smectite. Time-dependent behaviours have also been investigated thorough creep tests and as a first approximation can be attributed to viscoplastic deformation and subcritical propagation of microcracks of the clay matrix. Based on experimental results, different kinds of macroscopic constitutive models have first been proposed to describe the elastic, plastic, viscoplastic and damage behaviors of the COX claystone, for instance (Chiarelli et al., 2003; Hoxha et al., 2007; Shao et al., 2006). These macroscopic models can generally capture the overall responses of the material but fail to properly taking into account effects of micro-structure. For example, the macroscopic models are not able to explicitly describe the effects of mineral compositions and spatial distribution of mineral inclusions. In order to improve and complete the macroscopic models, an important effort has been made during the last years

on the development of micro-mechanical models based on various homogenization techniques. Concerning clayey rocks, several micro-macro models have also been proposed, for instance (Abou-Chakra Guéry et al., 2008; Shen et al., 2013b, 2012c). In these models, the claystone has been represented as a three phase composite constituted by a clay matrix and quartz and calcite grains. The clay matrix has been further considered as a porous medium composed of a solid phase and spherical pores (Shen et al., 2013b, 2012c). Some other models have been proposed for modeling the time-dependent behaviours of the claystone (Bikong et al., 2015; Huang et al., 2015; Huang and Shao, 2013; Huang et al., 2014). The models provide an interesting alternative way for modeling heterogeneous rock like materials taking into account effects of micro-structures. However, in order to obtain analytical or semi-analytical formulations, strong assumptions were generally introduced on the description of microstructure. For instance, all mineral inclusions and pores were assumed to be of spherical form and randomly embedded in the solid phase. The real microstructure of most rock like materials is obviously more complex than this simplified representation. In view of not only validating analytical micro-mechanical models but also studying effects of microstructure on macroscopic behaviors, it is needed to develop numerical simulations based a realistic description which should be as close as possible to the real microstructure.

For this purpose, we propose here to apply a numerical method based on the Fast Fourier Transform (FFT). This mathematical technique was successfully applied by Moulinec and Suquet (1994, 1998) as an alternative approach of the finite element method to compute the effective properties of composite materials with a periodic microstructure. This approach was further improved by an accelerated scheme to improve its computational efficiency (Eyre and Milton, 1999; Michel et al., 1999, 2000) and to extend its ability to voids and rigid inclusions (Michel et al., 2001). The main advantage of FFT approach is ability to efficiently consider non-regular geometrical forms of microstructure due to the fact that no volumetric meshing is needed since the heterogeneous material field is discretized into a series of grid points. Different mechanical properties can be assigned on each point according to its location inside the heterogeneous micro-structure. The overall responses at the macroscopic scale are then obtained by the volumetric average on the unit cell of the local stress and strain fields at the microscopic scale (Hill, 1963; Li and Wang, 2008).

The main objective of this thesis is to make use of the FFT based method to study

the heterogeneous geomaterials by taking into account effects of mcrostructure. The organization of this research is as follows:

Chapter 1 reviews briefly the basic principles of homogenization approaches in respect of the analytical and numerical homogenization methods for studying the effective behaviors of heterogeneous materials.

Chapter 2 is devoted to formulate the numerical method based on fast Fourier transforms (FFT) in the aspects of mathematical fundamentals and the numerical algorithm. The basic scheme is reviewed based on a local problem and the procedure of implementation of the numerical calculation is fully explained with the discretization of microstructure. The comparison of the accelerated schemes are discussed and the convergence rate are tested and veryfied for strain based formulations. An elastoplastic model is established as a benchmark for a two-phase material consisting of elastoplastic matrix with perfectly elastic inclusions. The results are compared with the work of (Moulinec and Suquet, 1998) as a validation. The application is extended to the porous materials and compared with the FEM solution obtained from Abaqus as well as some typical numerical homogenization approaches on matrix-inclusion type composites.

Chapter 3 aims to present the numerical treatment of microstructures by the FFT method and to study the effects of microstructure on the macroscopic response of the nonlinear matrix-inclusion type composites. Different microstructures will be studied, for example, matrix reinforced by one centered spherical/ellipsoidal inclusion, or randomly distributed inclusions, to show the inclusion shape, size and orientations effects. The isotropic and anisotropic behaviors are studied and the influence of sample orientation is discussed.

Chapter 4 is devoted to apply the FFT method to investigate the effective mechanical behaviors of rock like materials by taking into account effects of microstructure. A class of rock materials is considered as a continuous matrix phase embedded within mineral inclusions where one or several constituent phases exhibit a nonlinear inelastic behavior. The proposed numerical model is firstly veryfied by comparing numerical results with reference solutions obtained by direct finite element simulations. It will be then applied to a typical clayey rock consisting of an elastic-plastic clay matrix reinforced by linear elastic quartz and calcite grains. The proposed numerical model is further extended by including the progressive damage process due to the growth of micro-cracks. Comparisons between numerical results and experimental data will be presented to assess the efficiency of the

numerical model.

Chapter 5 applies the FFT based method to analyze the effect of microstructure on the effective behaviors of random porous geomaterials such as void shapes, sizes, orientations and distributions, *etc*. A compressible matrix with one spherical or ellipsoidal void is considered to investigate the effects of void shape on the overall behavior of porous geomaterial. More complex microstructures is considered to show the influence of void sizes, orientations and distributions. A simple damage model is proposed to describe the material softening behavior due to induced damage process and its evolution.

Chapter 6 concludes the research of making use of FFT method on the heterogeneous geomaterials and some recommendations for future research are stated.

Contents

List of symbols

Tensor operations

a Scalar[1]

$\boldsymbol{a}/a_i$ Vector[2]

$\boldsymbol{\sigma}/\sigma_{ij}$ Second order tensor

$\mathbb{A}/A_{ijkl}$ Forth order tensor

$\boldsymbol{\sigma}\cdot\boldsymbol{n} \Leftrightarrow \sigma_{ij}n_j$ Dot product

$\mathbb{L} : \boldsymbol{\varepsilon} \Leftrightarrow L_{ijkl}\varepsilon_{kl}$ Double-dot product

$< f >$ Average of field f

$f * g$ Convolution product

$\mathcal{F}/\mathcal{F}^{-1}$ Fourier transform/Inverse Fourier Transform

$\boldsymbol{\Gamma}/\boldsymbol{G}$ Green's operator

Main variables

$\boldsymbol{n}$ Normal vector

f_r Quantity in rth phase

ξ Frequency in Fourier space

[1] In symbolic notation, italic letters (*e.g.* f, g, ...) denote scalar, bold italic letters (*e.g.* $\boldsymbol{u}$, $\boldsymbol{n}$, ...) vectors, bold greek letters (*e.g.* $\boldsymbol{\sigma}$, $\boldsymbol{\varepsilon}$, ...) second order tensors, uppercase bold italic letters (*e.g.* $\mathbb{A}$,$\mathbb{C}$, ...) forth order tensors.

[2] In indicial notation, the components of tensors denoted by those letters with subscripts (*e.g.* a_i, σ_{ij}, L_{ijkl}, ...)

$\hat{a}$ Quantity in Fourier space

$\bar{a}$ Average field

a^* Periodic field

Main tensor fields

$\boldsymbol{u}/u_i$ Microscopic displacement

$\boldsymbol{\varepsilon}/\varepsilon_{ij}$ Microscopic strain

$\boldsymbol{\sigma}/\sigma_{ij}$ Microscopic stress

$\boldsymbol{S}/S_{ij}$ Deviator stress

σ_m Microscopic mean stress

σ_{eq} Microscopic equivalent stress

$\boldsymbol{\Sigma}/\bar{\sigma}$ Macroscopic stress[3]

$\boldsymbol{E}/\bar{\varepsilon}$ Macroscopic strain

Σ_m Macroscopic mean stress

Σ_{eq} Macroscopic equivalent stress

Material parameters

E Young's modulus

ν Poisson ratio

k Bulk modulus

G/μ Shear modulus

f Porosity

Forth order tensor

$\mathbb{C}^{hom}$ Homogenized quantity

[3]Macroscopic fields denoted by uppercase greek letters (*e.g.* $\boldsymbol{\Sigma}/\Sigma_{ij}$) or average fields of lowercase greek letters (*e.g.* $\bar{\sigma}$, $\bar{\varepsilon}$), and microscopic fields indicated by lowercase Greek letters(*e.g.* $\boldsymbol{\sigma}/\sigma_{ij}$)

$\mathbb{C}$ Elastic stiffness tensor

$\mathbb{L}$ Tangent stiffness tensor

$\mathbb{A}$ Localization tensor

$\mathbb{P}$ Hill's tensor

$\mathbb{S}^{E}$ Eshelby tensor

Chapter 1

Introduction to homogenization methods for heterogeneous materials

In many engineering structures, the heterogeneous materials have been widely used and studied. For example, the concrete is the most common used heterogeneous material with a complex microstructure. At the mesoscale, the concrete is composed of cement paste and aggregate particles. The Callovo-Oxfordian (COx) claystone has been investigated in France for the geological disposal of radioactive waste. The COx claystone is composed of clay minerals, calcite grains, quartz grains and minor minerals. The volumetric fractions and the distributions of these mineral inclusions, aggregate particles and pores have important influences on the macroscopic mechanical behavior of the studied heterogeneous material. In order to consider these effects and take into account the complex microstructure, many analytical and numerical homogenization methods have been proposed.

Voigt (1889) and Reuss (1910) firstly studied the effective properties by assuming uniform strain and uniform stress within the composite medium. And their estimates are theoretically considered as the upper and lower bounds for the overall properties of heterogeneous materials. The Eshelby's inclusion method (Eshelby, 1957) was regarded as a fundamental approach to determine the overall behaviors of the heterogeneous materials. Based on the solution of the Eshelby's equivalent inclusion problem, different linear homogenization schemes have been proposed as analytical solutions (Dilute scheme, Mori-Tanaka scheme and Self-consistent scheme). Among the numerical homogenization methods, Hill's tangent incremental approach (Hill, 1965) is an useful one to solve the non-linear homogenization problems (Abou-Chakra Guéry et al., 2008; Huang et al., 2014; Jiang et al., 2009;

Shen et al., 2012c). The Transformation Field Analysis (TFA) method was proposed in (Dvorak, 1992; Dvorak and Benveniste, 1992) to consider the local field variables as piecewise uniform to overcome the difficulty of large number of macroscopic internal variables. The more accurate and closer to reality method, Non-uniform Transformation Field Analysis (NTFA), was proposed by (Michel and Suquet, 2003, 2004) to assume the local field as non-uniform by considering a finite set of plastic modes. A numerical method based on fast Fourier transforms (FFT) was established in Moulinec and Suquet (1994) to determine the overall and local response of composites. The limitations of the FEM for complex micro-structures and high computational cost caused by a mass of mesh for the complex configuration were overcame by the new method. However, the rate of convergence of the "basic" scheme mentioned in (Moulinec and Suquet, 2003) is basically proportional to the contrast of Young's modulus between the phases of composites. The accelerate scheme (Eyre and Milton, 1999) extended by grid refinement to improve the performance of the original scheme. The infinite contrast case, *e.g.* porous materials or containing rigid inclusions, was proposed in Michel's work based on Augmented Lagrangian Method (Michel et al., 2000, 2001). Bilger et al. (2005) investigated the overall and local response of porous media on different classes of micro-structure corresponding to different spatial distributions of voids. And some research on crack propagation based on FFT method was studied as well (Li et al., 2012).

In this chapter, the basic principles of homogenization approaches will be briefly reviewed in respect of the analytical and numerical homogenization methods investigating the effective behaviors of nonlinear heterogeneous materials.

1.1 Basic principles of homogenization methods

1.1.1 Microstructure and Representative volume element

In the filed of micromechanics, the intent is to obtain the effective properties of composite materials from the microscopic ones on a *Representative Volume Element* (R.V.E.). The R.V.E. is introduced to represent the properties of the whole field of the composite material as the classical concept for the multiscale analysis. It is required to be the smallest sample containing sufficient information of the whole field of the composite materials. The characteristic sizes of heterogeneous constituents (d), of R.V.E. (l) and of structure (L) should satisfy some conditions for the separation of

scales. With respect to the characteristic size of R.V.E., the one of the heterogeneous constituent should be sufficient small ($d << l$) so that their number is enough to make the average on this R.V.E. meaningful. On the other hand, the characteristic size of the structure should be larger enough than the one of R.V.E.($l << L$) to be analyzed analytically or numerically. In this case, the studied structure can be seen as a homogeneous continuous medium.

The procedure of chosen the R.V.E is illustrated in Fig.1.1 from the macroscopic scale and microscopic scale with a typical hetergonenesou material, so-called COx claystone. The microstructure of the COx claystone is complex with multiple mineral grains and clayed matrix (see the figure of macroscopic scale in Fig.1.1). At the mesoscale, three main phases are observed: 40% to 50% of clay minerals, 20% to 27% of calcite and 23% to 25% of quartz. A small quantity of other minerals such as pyrite, mica, dolomite, halite and gypse are also identified.

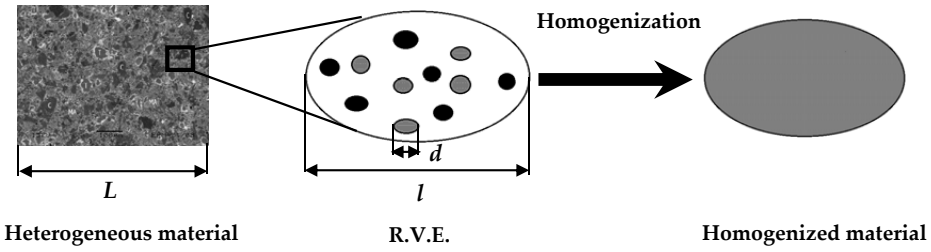

Fig. 1.1 Representative and homogenization procedure.

1.1.2 Boundary conditions and average theorem

The objective of the micromechanical homogenization is to find the homogenized or effective medium of a non-homogeneous material. Consider a R.V.E occupied a domain $\boldsymbol{V}$ with the elastic tensor $\mathbb{C}(\boldsymbol{x})$ and boundary $\partial \boldsymbol{V}$, the mechanical behavior of each material point is precisely known within the R.V.E. The local constitutive equations, compatibility conditions and equilibrium equations are expressed as follows:

$$\boldsymbol{\sigma}(\boldsymbol{x}) = \mathbb{C}(\boldsymbol{x}) : \boldsymbol{\varepsilon}(\boldsymbol{x}), \qquad \boldsymbol{\varepsilon}(\boldsymbol{x}) = \frac{1}{2}\left(\boldsymbol{u}(\boldsymbol{x}) + \boldsymbol{u}(\boldsymbol{x})^T\right), \qquad \nabla \cdot \boldsymbol{\sigma}(\boldsymbol{x}) = \boldsymbol{0} \qquad \forall x \in \boldsymbol{V}, \tag{1.1}$$

where $\boldsymbol{x}$ is the spatial coordinates of the material point, and determines its individual material properties at the microscopic scale.

In order to solve the mechanical system, boundary conditions have to be applied

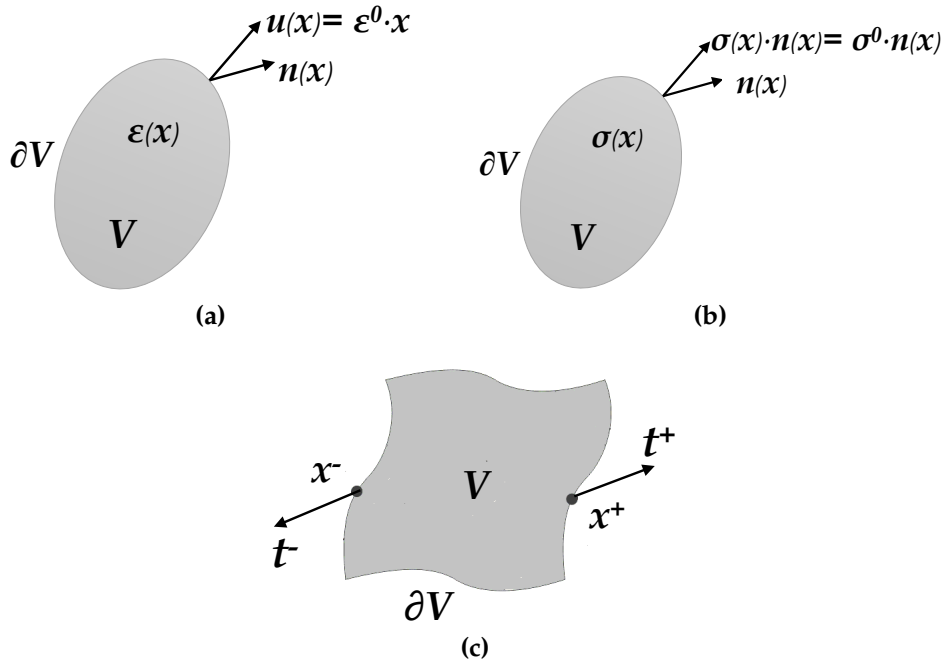

Fig. 1.2 Boundary conditions.: (a) Affine displacement on a R.V.E; (b) Uniform stress on a R.V.E.; (c) Periodic boundary condition on an unit cell.

on the R.V.E. to close the problem. From the view of macroscopic scale, the R.V.E can be considered as a homogeneous material. In other words, the affine displacement or uniform stress prescribed on the boundary of the R.V.E will generate a uniform stress or strain on the whole field. On the other hand, at the microscopic scale the strain and stress fields are non-homogeneous due to the heterogeneity of the microstructure. The purpose is to find the *homogenized* properties of non-homogeneous material at the macroscopic level. Hence, three types of boundary conditions are considered, uniform strain and uniform traction for general structures, and periodic boundary conditions for periodic structures.

-Uniform strain

As is shown in Fig. 1.2a a uniform strain $\boldsymbol{\varepsilon}^0$ is prescribed on the boundary $\partial \boldsymbol{V}$:

$$\boldsymbol{u}(\boldsymbol{x}) = \boldsymbol{\varepsilon}^0 \cdot \boldsymbol{x}, \qquad \forall \boldsymbol{x} \in \partial \boldsymbol{V}, \tag{1.2}$$

the average of microscopic strain within the R.V.E. is defined as:

$$\langle \boldsymbol{\varepsilon} \rangle = \frac{1}{V} \int_V \boldsymbol{\varepsilon}(\boldsymbol{x}) dV = \boldsymbol{\varepsilon}^0, \qquad \forall \boldsymbol{x} \in \boldsymbol{V}, \tag{1.3}$$

and it is proved that the average of microscopic strain within the R.V.E is equal to the prescribed strain on the boundary. Then, the generated macroscopic stress is defined by:

$$\langle \boldsymbol{\sigma} \rangle = \frac{1}{V} \int_V \boldsymbol{\sigma}(\boldsymbol{x}) dx, \tag{1.4}$$

thus the effective strain-stress relation for composite can be related via a function f:

$$\langle \boldsymbol{\sigma} \rangle = f(\boldsymbol{\varepsilon}^0). \tag{1.5}$$

-Uniform stress

The R.V.E. is imposed a uniform stress $\boldsymbol{\sigma}^0$ on the boundary $\partial \boldsymbol{V}$ (Fig. 1.2b):

$$\boldsymbol{\sigma}(\boldsymbol{x}) \cdot \boldsymbol{n}(\boldsymbol{x}) = \boldsymbol{\sigma}^0 \cdot \boldsymbol{n}(\boldsymbol{x}), \qquad \forall \boldsymbol{x} \in \partial \boldsymbol{V}, \tag{1.6}$$

and the average of microscopic stress on the whole R.V.E. is

$$\langle \boldsymbol{\sigma} \rangle = \frac{1}{V} \int_V \boldsymbol{\sigma}(\boldsymbol{x}) dV = \boldsymbol{\sigma}^0, \qquad \forall \boldsymbol{x} \in \boldsymbol{V}, \tag{1.7}$$

It is demonstrated that the average of microscopic stress within the R.V.E is equal to the prescribed stress on the boundary. Then, the strain filed resulted by the imposed stress field is defined by averaging the microscopic strain on the whole R.V.E.:

$$\langle \boldsymbol{\varepsilon} \rangle = \frac{1}{V} \int_V \boldsymbol{\varepsilon}(\boldsymbol{x}) dx, \tag{1.8}$$

and the homogenized strain-stress relation is associated with a function g:

$$\langle \boldsymbol{\varepsilon} \rangle = g(\boldsymbol{\sigma}^0). \tag{1.9}$$

-Periodic strain

For a periodic composite, the R.V.E can be replaced by a unit cell and periodic boundary conditions are required. As a periodic strain field $\boldsymbol{\varepsilon}^0$ is applied on the boundary of the unit cell $\partial \boldsymbol{V}$, the actual strain field is decomposed into two terms:

$$\boldsymbol{\varepsilon}(\boldsymbol{x}) = \boldsymbol{\varepsilon}^0 + \boldsymbol{\varepsilon}^*(\boldsymbol{x}), \qquad \boldsymbol{\varepsilon}^* \text{ is periodic}, \tag{1.10}$$

where $\boldsymbol{\varepsilon}^*$ is the strain caused by the heterogeneity of the composite material. Applying the volume average operator, it is proved that the average of microscopic strain is still equal to the prescribed affine displacement $\boldsymbol{\varepsilon}^0$:

$$\langle \boldsymbol{\varepsilon} \rangle = \frac{1}{V} \int_V \boldsymbol{\varepsilon}(\boldsymbol{x}) d\boldsymbol{V} = \boldsymbol{\varepsilon}^0, \qquad \forall \boldsymbol{x} \in \boldsymbol{V}. \tag{1.11}$$

In fact, the periodic term $\boldsymbol{\varepsilon}^*$ is vanished after averaging the microscopic strain on the unit cell and has no effect on the overall behavior of the composite material.

$$\langle \boldsymbol{\varepsilon}* \rangle = \frac{1}{V} = \int_V \boldsymbol{\varepsilon}*(\boldsymbol{x}) d\boldsymbol{V} = \mathbf{0}, \quad \forall x \in \boldsymbol{V}. \tag{1.12}$$

Then, the produced stress is defined via Eq. (1.4), and the overall strain-stress behavior is determined with a function F:

$$\langle \boldsymbol{\sigma} \rangle = F(\boldsymbol{\varepsilon}^0). \tag{1.13}$$

Note that the macroscopic values are known according to their boundary conditions regardless of the microscopic properties and distributions. With the average propositions for different boundary conditions, the *Hill's lemma* can be derived directly in Eq.(1.14), *i.e* the average of the microscopic internal work is equal to the internal work at macroscopic scale:

$$\langle \boldsymbol{\sigma}_{ij} : \boldsymbol{\varepsilon}_{ij} \rangle = \langle \boldsymbol{\sigma}_{ij} \rangle : \langle \boldsymbol{\varepsilon}_{ij} \rangle, \tag{1.14}$$

and it satisfies the energy condition in the framework of the effective properties of composite materials.

From the microscopic view, the corresponding field is induced within the R.V.E. as the boundary conditions applied and it is proved that the boundary value is identical with the average of the resulted field. After resolving the average of the corresponding field, the effective strain and stress relation is determined. In the following, the averaged strain and stress is denoted as $\boldsymbol{E}$ and $\boldsymbol{\Sigma}$ instead of $\langle \varepsilon \rangle$ and $\langle \boldsymbol{\sigma} \rangle$ as well as the boundary conditions $\boldsymbol{\varepsilon}^0$ and $\boldsymbol{\sigma}^0$. Thus, the effective constitutive relation is expressed as:

$$\boldsymbol{\Sigma} = \mathbb{C}^{hom} : \boldsymbol{E}, \tag{1.15}$$

where $\mathbb{C}^{hom}$ denotes the homogenized elastic tensor to be determined.

1.1.3 Determination of macroscopic response

As the R.V.E is defined and the boundary conditions are known, the macroscopic response is able to be determined. Consider a N-phase composite material occupied a domain V with the elastic stiffness tensor $\mathbb{C}(\boldsymbol{x})$. Each phase occupied a subdomain V_r with a volume fraction f_r ($r = 1,...,N$) characterized by a function $\chi_r(x)$ and its volume fraction f_r:

$$\chi_r(x) = \begin{cases} 1 & \text{if } x \in V_r, \\ 0 & \text{otherwise}, \end{cases} \qquad \text{with } f_r = \langle \chi_r \rangle. \tag{1.16}$$

The symbol $\langle \cdot \rangle$ denotes the average of a field ϕ over a domain, for example, an individual phase V_r:

$$\langle \phi_r \rangle = \frac{1}{V_r} \int_{V_r} \chi(x) f_r(x) dx. \tag{1.17}$$

therefore, the average on the whole field is defined:

$$\langle \phi \rangle = \sum_{r=1}^{N} f_r \langle \phi_r \rangle. \tag{1.18}$$

The average field over the entire field of composite is considered as the macroscopic field. In other words, the average operator associates the microscopic with macroscopic level. The average filed on the whole R.V.E. represents the uniform value within a homogeneous materials of the same size as the R.V.E.

The average stress and strain fields in each phase are defined by:

$$\boldsymbol{\sigma}_r = \frac{1}{V_r} \int_{V_r} \boldsymbol{\sigma}(\boldsymbol{x}) d\boldsymbol{x}, \quad \boldsymbol{\varepsilon}_r = \frac{1}{V_r} \int_{V_r} \boldsymbol{\varepsilon}(\boldsymbol{x}) d\boldsymbol{x}, \qquad \forall \boldsymbol{x} \in V_r. \tag{1.19}$$

Applying the volume average (Eq.1.18) on the whole field V, the microscopic level (stress $\boldsymbol{\sigma}$ and strain $\boldsymbol{\varepsilon}$) and macroscopic level (stress $\boldsymbol{\Sigma}$ and strain $\boldsymbol{E}$) are associated as:

$$\langle \boldsymbol{\sigma}(\boldsymbol{x}) \rangle = \sum_{r=1}^{N} f_r \boldsymbol{\sigma}_r = \boldsymbol{\Sigma}, \qquad \langle \boldsymbol{\varepsilon}(\boldsymbol{x}) \rangle = \sum_{r=1}^{N} f_r \boldsymbol{\varepsilon}_r = \boldsymbol{E}. \tag{1.20}$$

Consider the case that a uniform strain boundary condition is applied, and it is known that the boundary value (known) is identical to the average of the strain on the whole field. As the macroscopic stress is known the homogenized stiffness

tensor is able to computed. For this purpose a localization tensor $\mathbb{A}(\boldsymbol{x})$ is introduced to relate the local strain and the macroscopic strain:

$$\boldsymbol{\varepsilon}(\boldsymbol{x}) = \mathbb{A}(\boldsymbol{x}) : \langle \boldsymbol{\varepsilon}(\boldsymbol{x}) \rangle = \mathbb{A}(\boldsymbol{x}) : \boldsymbol{E}. \tag{1.21}$$

It is noted that the localization tensor $< \mathbb{A} >= \mathbb{I}$ and $\mathbb{I}$ denotes the forth order unit tensor in component form: $I_{ijkl} = \frac{1}{2}(\delta_{ik}\delta_{il} + \delta_{il}\delta_{jk})$ with the Kronecker delta δ_{ij}.

Therefore, the macroscopic stress reads as:

$$\langle \boldsymbol{\sigma}(\boldsymbol{x}) \rangle = \langle \mathbb{C}(\boldsymbol{x}) : \mathbb{A}(\boldsymbol{x}) \rangle : \boldsymbol{E} \quad \Leftrightarrow \quad \boldsymbol{\Sigma} = \mathbb{C}^{hom} : \boldsymbol{E}. \tag{1.22}$$

and the homogenized elastic tensor $\mathbb{C}^{hom}$ is given accordingly by

$$\mathbb{C}^{hom} = \langle \mathbb{C} : \mathbb{A} \rangle. \tag{1.23}$$

As the means of the locolization tensor $\mathbb{A}_r$ are known at each phase r on the N phases composite medium, the macroscopic elastic tensor is given by:

$$\mathbb{C}^{hom} = \sum_{r=0}^{N} f_r \mathbb{C}_r : \mathbb{A}_r, \tag{1.24}$$

where f_r denotes the volume fraction of the rth phase. It can be also expressed in an alternative form:

$$\mathbb{C}^{hom} = \mathbb{C}_0 + \sum_{r=1}^{N} f_r (\mathbb{C}_r - \mathbb{C}_0) : \mathbb{A}_r, \tag{1.25}$$

in which $\mathbb{C}_0$ is the elastic constant of the matrix.

It is obvious in Eq.(1.25) that the strain concentration tensor $\mathbb{A}_r$ in each phase is the solution of the homogenization problem. However, the exact expression of $\mathbb{A}_r$ cannot be given analytically for most of composite with various microstructures.

The exact solution of the effective properties of composite materials is almost intractable to determine (only for certain regular microstructure with linear constitutive behavior). The optimal way is to find the approximate solution or the range to provide the best estimate, so-called the bounds, according to some parameters characterizing the microstructure, for example, the volume fraction of each constituent. For this purpose, many homogenization approaches have been developed. In the following, some of the typical analytical linear homogenization approaches and

numerical methods are reviewed.

1.2 Analytical homogenization methods

This section summarizes the analytical homogenization approaches for the heterogeneous materials. The most classical schemes are reviewed briefly due to the fundamental importance in many cases.

1.2.1 The Voigt and Reuss bounds

The primary effort was performed by Voigt (1889) and Reuss (1910) and their estimates are typically considered as the extremes of the upper and lower bounds for the effective properties of composite materials. Voigt assumed that the strain field within the composite medium is uniform, thus the average of the elastic tensor on the whole field is computed with the volume fraction f_r and elastic tensor $\mathbb{C}_r$ in rth phase:

$$\mathbb{C}^{Voigt} = \sum_{r=1}^{N} f_r \mathbb{C}_r. \tag{1.26}$$

Similarly, Reuss considered the stress field within the heterogeneous material is uniform, and the average is obtained:

$$\mathbb{C}^{Reuss} = (\sum_{r=1}^{N} f_r \mathbb{C}_r^{-1})^{-1}. \tag{1.27}$$

It is obvious that the Voigt bounds is a special case of the Eq.(1.25) as $\mathbb{A} = \mathbb{I}$:

$$\mathbb{C}^{hom} = \langle \mathbb{C} : \mathbb{A} \rangle = \langle \mathbb{C} \rangle = \sum_{r=1}^{N} f_r \mathbb{C}_r = \mathbb{C}^{Voigt}. \tag{1.28}$$

It is proved based on the variational formulations that the estimates of Voigt and Reuss are rigorous upper and lower bounds, respectively (Hill, 1952):

$$\mathbb{C}^{Reuss} \leqslant \mathbb{C}^{hom} \leqslant \mathbb{C}^{Voigt}. \tag{1.29}$$

The inequality provides the extremes of analytical solution regardless of the geometry, however, the bounds are either too stiff or too soft and are impractical

in engineering practice. Some narrower and more useful bounds are developed based on Voigt and Reuss bounds, for example, Hill's average bounds (Hill, 1952), Hashin-Shtrikman bounds (Hashin and Shtrikman, 1963) and others mentioned in (Aboudi et al., 2012). Nevertheless, the approaches proposed according to geometries *i.e.* interacting of phases, periodic and random microstructures, are more useful and further investigations have been largely contributed for finding the analytical methods of homogenization for composite materials.

1.2.2 Eshelby equivalent inclusion method

Eshelby (Eshelby, 1957) studied a homogeneous linear elastic solid occupied a domain Ω embedded an subdomain Ω^0. The elastic constants of the insider subdomain (inclusion) and outside subdomain (matrix) are the same C_{ijkl}. An eigenstrain (stress-free transformation strain) ε^*_{ij} is imposed on the subdomain Ω^0 and is assumed to be uniform. Therefore, the stress and strain relationship inside the inclusion is

$$\sigma_{ij} = C_{ijkl} : (\varepsilon^I_{kl} - \varepsilon^*_{kl}), \tag{1.30}$$

where $\boldsymbol{\varepsilon}^I_{kl}$ denotes the constrained strain inside the inclusion. A forth order tensor is introduced to associate the constrained strain with its eigenstrain:

$$\varepsilon^I_{ij} = S_{ijkl} : \varepsilon^*_{ij}, \tag{1.31}$$

S_{ijkl} is called Eshelby's tensor and is minor symmetric:

$$S_{ijkl} = S_{jikl} = S_{ijlk}, \qquad S_{ijkl} \neq S_{klij}. \tag{1.32}$$

The Eshelby tensor S_{ijkl} ($\mathbb{S}^E$ in tensor form) is a spatial function and depends on material properties and the shape of inclusions. The explicit form exists only for specific shapes (sphere, ellipsoid, cylinder *etc*.). In general, the Eshelby tensor can be expressed in the form:

$$S_{ijmn} = -\frac{1}{2} C_{lkmn}(P_{iklj} + P_{jkli}), \tag{1.33}$$

where P_{ijkl} ($\mathbb{P}$ in tensor form) is an auxiliary tensor related to Eshelby's tensor, so-called Hill's tensor, and takes the form in Green's function $G_{ij}(\boldsymbol{x}-\boldsymbol{x}')$:

$$P_{ijkl} = -\int_{\Omega^0} G_{ij,kl}(\boldsymbol{x}-\boldsymbol{x}')d\Omega(\boldsymbol{x}'). \tag{1.34}$$

Eshelby firstly studied the case of an ellipsoidal inclusion embedded in an infinite matrix and provided an explicit form of S_{ijkl} as a fundamental solution of homogenization problems. For the case of a spherical inclusion in an isotropic medium, the Eshelby's tensor takes the compact form with the Poisson ratio ν:

$$S_{ijkl} = \frac{5\nu-1}{15(1-\nu)}\delta_{ij}\delta_{kl} + \frac{4-5\nu}{15(1-\nu)}(\delta_{ik}\delta_{jl}+\delta_{il}\delta_{jk}). \tag{1.35}$$

1.2.3 Dilute scheme

As the volume fraction of inclusions is low, the inclusions are considered to be dilute suspension in an infinite matrix phase and the interactions among the particles are negligible. The solution for this situation is called dilute scheme. The R.V.E. undergoes an external load $\boldsymbol{E}^\infty$ and the average strain in each phase is computed as

$$\boldsymbol{\varepsilon}_r = (\mathbb{I}+\mathbb{S}^E:(\mathbb{C}_0)^{-1}:(\mathbb{C}_r-\mathbb{C}_0))^{-1}:\boldsymbol{E}^\infty. \tag{1.36}$$

where $\mathbb{I}$ denotes the forth order unit tensor, $\mathbb{S}^E$ is the Eshelby's tensor. $\mathbb{C}_0$ and $\mathbb{C}_r$ represents the elastic tensor of matrix and individual phase, respectively.

For the dilute distributed inclusions, the external strain $\boldsymbol{E}^\infty$ tends to be the average strain $\boldsymbol{E}$ and $\boldsymbol{\varepsilon}_r = \mathbb{A}_r:\boldsymbol{E}$. Therefore, the localization tensor of the rth phase is given by:

$$\mathbb{A}_r^{dil} = [\mathbb{I}+\mathbb{S}^E:(\mathbb{C}_0)^{-1}:(\mathbb{C}_r-\mathbb{C}_0)]^{-1}. \tag{1.37}$$

Substitute it into Eq. 1.25 for a composite with N dilute distributed inclusions, the macroscopic elastic tensor is defined as:

$$\mathbb{C}^{hom} = \mathbb{C}_0 + \sum_{r=1}^{N} f_r[(\mathbb{C}_r-\mathbb{C}_0)^{-1}+\mathbb{S}:\mathbb{C}_0^{-1}]. \tag{1.38}$$

1.2.4 Mori-Tanaka scheme

As the volume fraction of particles increases, the interactions between the phases are significant. The composite material is modeled as N families of ellipsoidal inclusions interacting each other. The idea of Mori and Tanaka (1973) is to simplify the the problem of localization in representing the inclusions with same shape, orientation and elastic behavior by an equivalent ellipsoidal inclusion in an infinite medium with elastic tensor $\mathbb{C}_0$ of the matrix undergoes a constant strain $\boldsymbol{E}^0$. The strain in individual phase is written based on the solution of Eshelby's problem:

$$\boldsymbol{\varepsilon}_r = (\mathbb{I} + \mathbb{S}^E : (\mathbb{C}_0)^{-1} : (\mathbb{C}_r - \mathbb{C}_0))^{-1} : \boldsymbol{E}^0. \tag{1.39}$$

With the help of the average relation: $\langle \boldsymbol{\varepsilon} \rangle = \boldsymbol{E}$, the strain $\boldsymbol{E}^0$ is given by:

$$\boldsymbol{E}^0 = (\sum_{r=0}^{N} f_r (\mathbb{I} + \mathbb{S}^E : (\mathbb{C}_0)^{-1} : (\mathbb{C}_r - \mathbb{C}_0))^{-1})^{-1} : \boldsymbol{E}. \tag{1.40}$$

It is noted that the term $(\mathbb{I} + \mathbb{S}^E : (\mathbb{C}_0)^{-1} : (\mathbb{C}_r - \mathbb{C}_0))^{-1}$ is exactly the localization tensor of the dilute scheme. In the following expression it will be noted as $\mathbb{A}_r^{dil}$. Therefore, the localization tensor of Mori-Tanaka scheme for the rth phase is written by:

$$\mathbb{A}_r^{MT} = \mathbb{A}_r^{dil} : (\sum_{r=0}^{N} f_r \mathbb{A}_r^{dil})^{-1}. \tag{1.41}$$

And the macroscopic elastic tensor takes the form:

$$\mathbb{C}^{hom} = \sum_{r=0}^{N} f_r \mathbb{C}_r : \mathbb{A}_r^{dil} (\sum_{r=0}^{N} f_r \mathbb{A}_r^0)^{-1}, \tag{1.42}$$

which is equivalent to:

$$\mathbb{C}^{hom} = \mathbb{C}_0 + \sum_{r=1}^{N} f_r [(\mathbb{C}_r - \mathbb{C}_0)^{-1} + \mathbb{S}^E : (\mathbb{C}_0)^{-1}]^{-1} (\sum_{r=0}^{N} f_r \mathbb{A}_r^0)^{-1}. \tag{1.43}$$

1.2.5 Self-consistent scheme

The self-consistent scheme is particularly used for polycrystalline type materials, in which there is non dominant constituent. No matrix phase is clearly identified but

an arrangement of grains bonded to each other. The idea is to reduce the problem to the solution of an inclusion in an infinite effective medium. The localization tensor for self-consistent approach is expressed as:

$$\mathbb{A}_r^{sc} = [\mathbb{I} + \mathbb{S}^E : (\mathbb{C}^{hom})^{-1} : (\mathbb{C}_r - \mathbb{C}^{hom})]^{-1}, \tag{1.44}$$

The macroscopic elastic tensor is then written by:

$$\mathbb{C}^{hom} = \sum_{r=0}^{N} f_r \mathbb{C}_r : \mathbb{A}_r^{SC} (\sum_{r=0}^{N} f_r \mathbb{A}_r^{hom})^{-1}. \tag{1.45}$$

Due to the fact that the prescribed strain $\boldsymbol{E}^0$ is equal to the macroscopic strain $\boldsymbol{E}$, it is noted that:

$$(\sum_{r=0}^{N} f_r \mathbb{A}_r^{hom})^{-1} = \mathbb{I}, \tag{1.46}$$

and the macroscopic elastic tensor is simplified as:

$$\mathbb{C}^{hom} = \sum_{r=0}^{N} f_r \mathbb{C}_r : \mathbb{A}_r^{SC}. \tag{1.47}$$

1.3 Computational homogenization methods

Apart from analytical approaches, numerical homogenization approaches have been developed as reference solutions to predict the effective properties of the heterogeneous materials. In contrast to analytical solutions, the numerical methods have no limits on the microstructures, *i.e.* arrangements, constituents' properties and shapes, and the prediction is more accurate. The local fields are explicitly represented and the macroscopic fields are computed by averaging those local fields on the R.V.E. Some of the numerical homogenization methods performed by the Finite Element (FE) techniques are reviewed and some other approaches, for example, fast Fourier transforms (FFT) based method, are discussed in details as well.

1.3.1 Hill's incremental method

The incremental homogenization method was initially proposed for determining the overall properties of nonlinear heterogeneous materials (Hill, 1965).The main

steps for non linear homogenization with the incremental approach are illustrated in Fig. 1.3.

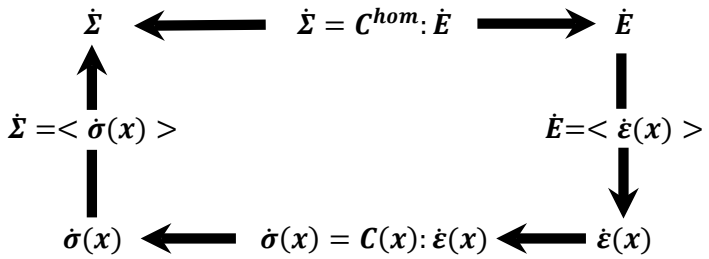

Fig. 1.3 Diagram of non linear homogenization method with incremental approach

Consider a R.V.E occupied a domain V with N phases, at the microscopic level the mechanical behavior of the individual phase V_r at its local position $\boldsymbol{x}$ in the R.V.E is written in the incremental form:

$$\dot{\sigma}(\boldsymbol{x}) = \mathbb{C}_r : \dot{\varepsilon}(\boldsymbol{x}), \qquad \forall x \in \boldsymbol{V_r}. \tag{1.48}$$

The relation of strain and stress between microscopic and macroscopic levels is expressed by introducing a forth order tensor $\mathbb{A}$:

$$\dot{\varepsilon}_r = \mathbb{A}_r(\boldsymbol{x}) : \dot{\boldsymbol{E}}, \tag{1.49}$$

where $\dot{\boldsymbol{E}}$ is the incremental macroscopic strain.

Combine Eq.(1.49) with Eq.(1.48) and take the average one can find:

$$\dot{\boldsymbol{\Sigma}} =< \mathbb{C}(\boldsymbol{x}) : \mathbb{A}(\boldsymbol{x}) >: \dot{\boldsymbol{E}}. \tag{1.50}$$

In fact, Eq. (1.50) shows the constitutive relations at the macroscopic level and the macroscopic tangent tensor can be easily derived as:

$$\mathbb{C}^{hom} =< \mathbb{C}(\boldsymbol{x}) : \mathbb{A}(\boldsymbol{x}) > . \tag{1.51}$$

In order to determine the homogenized tangent tensor $\mathbb{C}^{hom}$, the properties of each individual phase has to be taken into account. Consider the volume fraction f_r and local tangent tensor $\mathbb{C}_r$ of the rth phase, the homogenized tangent tensor at the

macroscopic is computed by:

$$\mathbb{C}^{hom} = \sum_{r=1}^{N} f_r \mathbb{C}_r : \mathbb{A}_r, \qquad r = 1, 2, ... \tag{1.52}$$

where the localization tensor $\mathbb{A}_r$ can be determined by the homogenization schemes stated previously. By using a Mori-Tanaka scheme, $\mathbb{A}_r$ can be expressed in the following:

$$\mathbb{A}_r = [\mathbb{I} + \mathbb{P}_r^0 : (\mathbb{C}_r - \mathbb{C}_0)]^{-1} : [\sum_{r=1}^{N} f_r [\mathbb{I} + \mathbb{P}_r^0 : (\mathbb{C}_r - \mathbb{C}_0)]^{-1}]^{-1}, \tag{1.53}$$

where $\mathbb{P}_r^0$ is the Hill's tensor characterized by the geometry of the rth phase of inclusions and the tangent tensor $\mathbb{C}_0$ of the matrix.

In order to solve the problem, it requires to compute the Hill's tensor $\mathbb{P}_r^0$ and stiffness tensor $\mathbb{C}_r$ for each individual phase. The Hill's tensor is identical for the same geometry of inclusion and can be defined by

$$\mathbb{P}^0 = \mathbb{S}(\mathbb{C}_0) : \mathbb{C}_0^{-1}, \tag{1.54}$$

and the local tangent modulus $\mathbb{C}_r$ is required to be determined by the local constitutive models used in each phase. For example, a three-phase composite consisted spherical elastic quartz and spherical elastic damaged calcite inclusions scattered inside the elastoplastic matrix are considered in (Abou-Chakra Guéry et al., 2008).

As the local behavior is characterized the local tangent modulus $\mathbb{C}_r$ is computed and the incremental method can be then applied in numerical algorithm. The integration is performed for each integration point of elements and the Hill's tensor $\mathbb{P}^0$ is calculated by the numerical integration. And the effective elastic modulus of the composite $\mathbb{C}^{hom}$ is determined with the Mori-Tanaka scheme.

The Hill incremental method is an efficient method for predicting the effective properties of composite materials, however, the approach provides a very stiff response. It has been improved with isotropization technique (Abou-Chakra Guéry et al., 2009) by evaluated the Eshelby tensor using an isotropic approximation of the tangent operator associated to the matrix. Moreover, even though with modified method it is validate for some specific cases, for example, time-dependent inelastic response. It considers only the properties and the volume fractions of constituents

but lacks the physical description of the microstructures, *e.g.* their shapes and distributions.

1.3.2 Secant method

The secant method has been proposed by many researchers to liniearize the local nonlinear constitutive laws by a secant operator to associate the total strain and total stress at each phase. (Suquet, 1996a,b)

$$\sigma_r = \mathbb{C}_r^s : \varepsilon_r, \qquad \mathbb{C}_r^s = 3k_r\mathbb{J} + 2\mu_r^s\mathbb{K}, \tag{1.55}$$

where the local secant shear modulus μ_r^s is a function of strain at each phase, which is approximated by the average strain $\bar{\varepsilon}$ by considering these secant moduli are constant at individual phase, and the forth order tensor $\mathbb{J}$ and $\mathbb{K}$ are defined in terms of components form:

$$J_{ijkl} = \frac{\delta_{ij}\delta_{kl}}{3}, \qquad K_{ijkl} = I_{ijkl} - K_{ijkl}, \qquad \text{with} \qquad I_{ijkl} = \frac{\delta_{ik}\delta_{jl} + \delta_{il}\delta_{jk}}{2}. \tag{1.56}$$

The macroscopic constitutive equation can be then written in the form of secant tensor $\mathbb{C}^s$:

$$\boldsymbol{\Sigma} = \mathbb{C}^s(\bar{\varepsilon}) : \boldsymbol{E}. \tag{1.57}$$

The effective strain $\bar{\varepsilon}$ can be defined by two approaches. The first one is called classical method (first moment approach) with the equivalent Von Mises strain:

$$\bar{\varepsilon}_r = \sqrt{\frac{2}{3}\boldsymbol{S}^r : \boldsymbol{S}^r}, \qquad S_{ij}^r = \varepsilon_{ij}^r - \frac{\varepsilon_{kk}^r}{3}\delta_{ij}. \tag{1.58}$$

And a modified method (the second moment approach) was proposed in (Suquet, 1995) that the reference equivalent strain is computed by:

$$\bar{\varepsilon}_r = \sqrt{\langle \varepsilon_{eq}^2 \rangle_r}, \tag{1.59}$$

The analytical expression of effective strain for the second method can be found in (Suquet, 1996a) and it can be also extended into ellipsoidal shape of multiphase composite.

1.3.3 Nonuniform transformation field analysis

The Transformation Field Analysis (TFA) is initially proposed in (Dvorak, 1992; Dvorak and Benveniste, 1992) by assuming the microscopic fields of internal variables as piecewise uniform and the method is proved to be an efficient method of reducing the number of macroscopic internal variables for computing the effective response of composite materials. Improvement and extensions have been made on the approach to reduce the number of internal variables by considering the plastic modes as non-uniform in plastic field and the homogenized properties of the composite is thus more accurate by the Nonuniform Transformation Field Analysis (NTFA) (Michel and Suquet, 2003, 2004) approach due to the accurate capture of the heterogeneity of the plastic strain field. The NTFA has been implemented in metal matrix composites with nonlinear (Chaboche et al., 2005) as well as geomaterials and porous materials (Jiang and Shao, 2013; Jiang et al., 2011).

The aim of the non-uniform transformation field analysis (NTFA) is to find the approximate resolution of the local problem, in other words, to determine the plastic field by considering the plastic strain $\boldsymbol{\varepsilon}^p$ as non-uniform within each individual phase V_r:

$$\boldsymbol{\varepsilon}^p(\boldsymbol{x}) = \sum_{k=1}^{M} \boldsymbol{\varepsilon}_k^p \mu^{(k)}(\boldsymbol{x}), \qquad \forall \boldsymbol{x} \in V_r, \tag{1.60}$$

where M is the total number of plastic modes, $\boldsymbol{\mu}^{(k)}$ is the kth plastic mode and V_r is the rth phase of the composite.

Certain assumptions are made to determine these plastic modes: each individual phase has its own group of modes and each of the mode has to satisfy the incompressible, orthogonal and normalized rules, *i.e.* $tr(\mu^{(k)}) = 0$, $< \mu^{(k)}, \mu^{(l)} >= 0$ and $< \mu_{eq}^{(k)} >= 1$.

The theoretical solution of a non linear homogenization of elastoplastic heterogeneous materials is expressed by the means of Green's operator as:

$$\boldsymbol{\varepsilon}(\boldsymbol{x}) = \mathbb{A} : \boldsymbol{E} + \frac{1}{V} \int_V \Gamma(\boldsymbol{x}, \boldsymbol{x}') : (\mathbb{C}(\boldsymbol{x}') : \boldsymbol{\varepsilon}^p(\boldsymbol{x}'))dV'. \tag{1.61}$$

With the approximation of Eq.(1.60), Eq.(1.61) becomes:

$$\boldsymbol{\varepsilon}(\boldsymbol{x}) = \mathbb{A} : \boldsymbol{E} + \sum_{l=1}^{M} (\mathbb{D} * \mu^{(l)})(\boldsymbol{x}) \boldsymbol{\varepsilon}_l^p, \tag{1.62}$$

where the nonlocal operator $\mathbb{D}(\boldsymbol{x},\boldsymbol{x}') = \Gamma(\boldsymbol{x},\boldsymbol{x}') : \mathbb{C}(\boldsymbol{x}')$ denotes the strain at point $\boldsymbol{x}$ generated by a transformed strain at point $\boldsymbol{x}'$.

The total reduced strain can be obtained by multiplying $\mu^{(k)}$ on Eq.(1.62) and averaging over V:

$$e_k = \boldsymbol{a}^{(k)} : \boldsymbol{E} + \sum_{l=1}^{M} D_{kl}^N \varepsilon_l^p, \tag{1.63}$$

where the reduced total strain e_k and plastic strain e_k^p, the reduced localization tensors $a^{(k)}$ and the interaction tensor D_{kl} are defined as:

$$e_k =< \boldsymbol{\varepsilon} : \boldsymbol{\mu}^{(k)} >, \quad e_k^p =< \boldsymbol{\varepsilon}^p : \boldsymbol{\mu}^{(k)} >, \quad \boldsymbol{a}^{(k)} =< \mathbb{A}^T : \boldsymbol{\mu}^{(k)} >, \quad D_{kl}^N =< \boldsymbol{\mu}^{(k)} : (\mathbb{D} * \boldsymbol{\mu}^{(l)}) > . \tag{1.64}$$

As these reduced variables are known, the local constitutive relations are expressed accordingly:

$$\tau_k =< \mu^{(k)} : \mathbb{C} : (\boldsymbol{\varepsilon}(\boldsymbol{x}) - \boldsymbol{\varepsilon}^p(\boldsymbol{x})) > . \tag{1.65}$$

The elastic tensor $\mathbb{C}(\boldsymbol{x})$ remains a constant in each phase, and assumes as isotropic characterized by two parameters, a bulk modulus $k^{(r)}$ and a shear modulus $G^{(r)}$. Taking into account the assumption of the NTFA for each plastic mode, incompressible and exists only in a single phase,

$$\mathbb{C} : \mu^{(k)} = 2G^{(k)}\mu^{(k)}. \tag{1.66}$$

thus, the stresses and strains are obtained as follows:

$$\tau_k = 2G^{(k)}(e_k - e_k^p). \tag{1.67}$$

In order to solve the problem, the reduced Von Mises yield criterion has been considered in two different models: uncoupled and coupled model in (Michel and Suquet, 2003). For the purpose of simplicity, a Drucker-Prager criterion coupled model is reviewed to fully explain the NTFA approach. The local yield function and flow rules are:

$$f_p = \alpha\sigma_m + \sigma_{eq} - R(\gamma^p), \tag{1.68}$$

$$\dot{\boldsymbol{\varepsilon}}^p = \dot{\gamma}^p(\frac{1}{3}\alpha\boldsymbol{\delta} + \frac{3}{2}\frac{\boldsymbol{S}}{\sigma_{eq}}). \tag{1.69}$$

where the equivalent stress and mean stress are expressed in terms of the reduced

variables:

$$\sigma_{eq} = (\frac{3}{2}\sum_{k=1}^{M}\tau_k^2)^{1/2}, \qquad \sigma_m = \frac{1}{3}\sum_{k=1}^{M}\tau_k. \tag{1.70}$$

and the reduced plastic flow rule is as follows:

$$\dot{e}_k^p = \frac{3}{2}\dot{\gamma}\frac{\tau_k}{\sigma_{eq}}. \tag{1.71}$$

Accordingly, the reduced plastic strains takes the form as:

$$\varepsilon_k^p = \frac{e_k}{<\boldsymbol{\mu}^{(k)} : \boldsymbol{\mu}^{(k)}>}. \tag{1.72}$$

Therefore, the constitutive relations are fully complete in terms of the reduced variables by the NTFA approach.

In the work mentioned above, the NTFA is implemented in metallic materials, porous materials and geomaterials and provides a very efficient way of simulate the effective properties of the composite materials. Nevertheless, the plastic modes required high computational costs and strongly influences the accuracy of the method. Furthermore, the NTFA has its limitations on the details of description of the microstructures.

1.3.4 Time-dependent behavior

Time-dependent behavior exists obviously in geomaterials as the study of experimental data and several approaches has been proposed to describe the important behavior. Abou-Chakra Guéry et al. (2009) proposed an elastoviscoplastic behavior for the clay matrix by extending the incremental method and Huang et al. (2014) extended the approach for the porous materials. In general, time-dependent deformation results in the evolution of microstructures, for example, dislocations, grain boundary slidings *etc.* and the strain exhibits as a function of applied loading. For instance, the viscoplastic strain in composite materials can be characterized in the local field as the flow rule:

$$\dot{\boldsymbol{\varepsilon}}^{vp} = \dot{\gamma}\frac{\partial f_{vp}}{\partial \boldsymbol{\sigma}}. \tag{1.73}$$

f_{vp} is the viscoplastic yield function and the viscoplastic multiplier $\dot{\gamma}$ is defined by:

$$\dot{\gamma} = 0 \qquad \text{if } f_{vp} \leq 0, \tag{1.74}$$

$$\dot{\gamma} = \frac{c_{vp}}{\eta}(\frac{f_{vp}}{c_{vp}})^m \qquad \text{if } f_{vp} > 0. \tag{1.75}$$

The parameter η and m controls the evolution rate of viscoplastic strain of the clay matrix. Thus, the rate of viscoplastic stress is determined

$$\dot{\boldsymbol{\sigma}} = \mathbb{C}(\dot{\boldsymbol{\varepsilon}} - \frac{c_{vp}}{\eta}(\frac{f_{vp}}{c_{vp}})^m \frac{\partial f_{vp}}{\partial \boldsymbol{\sigma}}). \tag{1.76}$$

As the local strain and stress are known, the macroscopic properties are determined by the modified Hill's incremental method as mentioned above.

1.3.5 Fast Fourier transforms method

The numerical method based on fast Fourier transforms (FFT) was originally proposed by (Moulinec and Suquet, 1994, 1998) to compute the effective response of the heterogeneous materials with complex microstructures. The primary idea is to make use of the image pixels of the actual microstructure directly as the material points in the numerical simulation which is enlightened by the principle of superposition in elastic linear theory. The solution is given in the Fourier series or integral form, and the corresponding displacement, strain and stress are then obtained as superpositions of the solutions and it can be also solved by the method of Green's functions (Milton, 2002; Mura, 1987; Nemat-Nasser and Hori, 1999). Nevertheless, the solutions are expressed in an integral equation formulation and difficult to find explicitly. Ponte Castañeda and Willis (1995) introduced a uniform reference medium to make use of the concept of polarization and expressed in terms of the strain as the Lippmann-Schwinger equation (refer to Kröner (1977)). The integral equation is able to resolve by an iterative algorithm with the means of Green's operator using fast Fourier transforms. Periodic microstructure is considered in the FFT method based on those theoretical fundamentals (Bornert et al., 2001) and the method for computing the effective properties of the periodic composite media is recalled in the following as a brief review.

For finding the effective properties of a heterogeneous material a homogeneous reference medium with constant stiffness tensor $\mathbb{C}^0$ is introduced and the problem

can be solved by making use of relevant Green's operator Γ^0:

$$\varepsilon(u(x)) = -\Gamma^0 * (\mathbb{C}(x) - \mathbb{C}^0) : \varepsilon(u(x)) + E. \tag{1.77}$$

In order to solve the integral equation, an iterative scheme is proposed:

$$\varepsilon(u^{i+1}) = -\Gamma^0 * (\mathbb{C} - \mathbb{C}^0) : \varepsilon(u^i) + E. \tag{1.78}$$

The integral equation is difficult to solve due to the convolution product, however, the convolution product can be transformed into a dot product by using the Fourier transforms analysis and the problem becomes solvable. The idea is firstly to transform the integral equation into Fourier space:

$$\hat{\varepsilon}^{i+1}(\xi) = \hat{\varepsilon}^i(\xi) - \hat{\Gamma}^0(\xi) : \hat{\sigma}^i(\xi), \qquad \forall \xi \neq 0, \quad \hat{\varepsilon}^{i+1}(0) = E, \tag{1.79}$$

and the initial integral equation can be resolved by transforming back into real space:

$$\varepsilon^{i+1}(x) = \mathcal{F}^{-1}(\hat{\varepsilon}^i(\xi)), \quad \sigma^{i+1}(x) = \mathbb{C}(x) : \varepsilon^{i+1}(x), \tag{1.80}$$

where the operator $*$ denotes the convolution product, $\mathcal{F}^{-1}$ indicates the inverse Fourier transforms and the symbol ξ is the frequencies in Fourier space.

The initial integral equation (Eq.(1.77)) is solved by using Fourier transforms analysis, but the problem for computing the overall response of periodic composite media still needs further discussion.

Unlike the finite element method (FEM) meshing structure the FFT based method simulates the actual structure as combination of discrete materials points. The structure is discreted into a regular grid consisting of $N_1 \times N_2$ pixels for two-dimensional problem ($N_1 \times N_2 \times N_3$ for three-dimensional problems). And the coordinates of the pixels in real space and frequencies are associated by the procedure of image processing. The coordinates of these pixels (2D problems) denoted by (i_1, i_2) in real space is defined by

$$x(i,j) = ((i_1 - 1) \cdot \frac{T_1}{N_1}, (i_2 - 1) \cdot \frac{T_2}{N_2}), \qquad i_1 = 1,2,...,N_1, \quad i_2 = 1,2,...,N_2, \tag{1.81}$$

where T_i is the period of the unit cell in ith direction ($i = 1,2$). And the corresponding

frequencies in Fourier space is defined by

$$\xi_i = \begin{cases} 0, \frac{1}{T_i}, ..., (\frac{N_i}{2} - 1)\frac{1}{T_i}, \frac{N_i}{2}\frac{1}{T_i}, & N_i \text{ is odd.} \\ 0, \frac{1}{T_i}, ..., \frac{N_i - 1}{2}\frac{1}{T_i}, & N_i \text{ is even.} \end{cases} . \tag{1.82}$$

At each pixel the variables used in the numerical calculations are sampled on these discrete points. In other words, the algorithm for solving the integral equations is calculated repeatedly at each pixel on the whole field until satisfying the tolerance and then the effective values are determined by the average theorem stated in previous section of fundamentals of homogenization methods. Note that the approach can be extended to the cases of the composite with nonlinear constituents by an implicit scheme for the incremental form of the field obey a nonlinear constitutive law.

The FFT based method will be elaborated in the next chapter and the efficiency and limitations will also be discussed. Application of computing homogenized properties of nonlinear heterogeneous materials will be performed on several case, for example, matrix-inclusion problem for two and three phases, complex microstructures, porous media *etc*. And the approach is extended into three dimensional problems with massive computational costs but optimized by parallel methods. improvements will be proposed as well.

1.4 Closing remarks

The significance of the inhomogeneous materials in engineering practice leads to the development of homogenization methods based on R.V.E. for determining their overall behaviors and as is known that each approach has its advantages and shortcomings. The classical bounds based on *rules of mixture* is basically proposed for the linear elastic fields and mean field approaches for matrix-inclusions composite such as Eshelby's inclusion problem, Mori-Tanaka and self-consistent schemes requires low computational costs but highly depends on the constituents arrangements. Meanwhile, semi-analytical solutions are also active research subjects, such as using Hill's incremental method in the FE code. The direct numerical methods, such as finite element (FE) computation, fast Fourier transforms (FFT) based approach on *unit cell* problems, so-called periodic microfield approaches or unit cell methods, are efficient and accurate, and is able to study the details on the local stress

and strain fields within the unit cell.

Some of those methods have been implemented for investigating the mechanical behaviors of Callova-Oxfordian argillite. The effective behavior based the Hill's incremental method is obvious stiffer than the experimental data and the *isotropization technique* is introduced to modify the algorithm but lack of physical explanations and descriptions of the mircrostructure. NTFA approach is proved to be very efficient and accurate, but the plastic modes requires high computational costs and intractable to implement. The FFT as a direct numerical method shows its potentials for studying the heterogeneous materials in nonlinear range and straightforwardly for the details in local fields as well. The application on the field of metallic medium has proved its efficiency and accuracy.

Chapter 2

Numerical method of periodic composite materials based on fast Fourier transforms

In this chapter, a detailed description of the numerical method based on fast Fourier transforms (FFT) is provided in the aspects of mathematical fundamentals and the numerical algorithm. The basic scheme is reviewed based on a local problem and the procedure of implementation of the numerical calculation is fully explained with the discretization of microstructure. The comparison of the accelerated schemes are discussed and the convergence rate are compared. Some examples of application are performed as the demonstration of the FFT based method. In Section 2.2 an elastoplastic model is established as a benchmark for a two phases material consisting of elastoplastic clay matrix with perfectly elastic inclusions. The results are compared with the work of (Moulinec and Suquet, 1998) as a validation. The application is extended to the porous materials and compared with the FEM solution obtained from Abaqus.

2.1 Numerical method based on fast Fourier transforms

The aim of the numerical method based on fast Fourier transform (known as FFT) is to determine effective properties of composites directly from images of its actual micro-structure in the numerical simulation (Moulinec and Suquet, 1994, 1998). The commonly used numerical method based upon the Finite Element Method (FEM)

encounters the difficulty of massive degrees of freedom and consequently consumes high computational costs due to the difficulty to mesh the complex micro-structures. On the other hand, FFT Method allows to make use of the grid points sampling the complex structures to certain numbers of mesh points which are assigned the specific material properties to represent the entire medium with their micro-structures. Mathematically, FFT is a fast algorithm to compute discrete Fourier transforms (DFT) and their inverses. DFT is the discrete form of Fourier transforms (FT) which is used efficiently solve partial differential equations, and to perform some complex operations much more easily such as convolutions by transforming the present function to another. In simple terms, fast Fourier transforms in the present approach is used to solve the equilibrium equations due to the merit of its simplicity and efficiency in numerical analysis and advantages of avoiding mesh for complex micro-structures. In the next, fast Fourier transforms will be elaborated from the aspects of mathematics and then extended into the problems of the resolution of effective properties of composite media.

2.1.1 Mathematical basis of fast Fourier transforms

As stated above Fourier transforms are the fundamentals of fast Fourier transforms and discrete Fourier transforms, thus, the definition of FT and its properties are firstly presented and the content related to this study is only referred.

Fourier transforms

Theoretically, Fourier transform (FT) transforms a mathematical function of time, $f(t)$, into a new function noted as $\hat{f}(\xi)$, whose argument ξ represents the frequency. The definition of the *Fourier transform* of the function $f(x)$ is

$$\hat{f}(\xi) = \int_{-\infty}^{+\infty} f(x) e^{-2\pi i \xi x} dx, \tag{2.1}$$

and it can be abbreviated in the form

$$\hat{f}(\xi) = \mathcal{F}[f(x)], \tag{2.2}$$

where $\mathcal{F}$ is the *Fourier transform operator*.

Under suitable condition, f can be determined by $\hat{f}$ through *inverse Fourier*

transform:

$$f(x) = \int_{-\infty}^{+\infty} \hat{f}(\xi) e^{2\pi i \xi x} d\xi, \tag{2.3}$$

in abbreviation form Eq. (2.3) can be rewritten as

$$f(x) = \mathcal{F}^{-1}[\hat{f}(\xi)], \tag{2.4}$$

where $\mathcal{F}^{-1}$ is so-called *inverse Fourier transform operator*.

Properties of Fourier transform

The properties of Fourier transform related to the present study are mentioned as a review in the following.

- **Linearity**
  For any complex number a and b, if $h(x) = af(x) + bg(x)$, then

  $$\hat{h}(\xi) = a \cdot \hat{f}(\xi) + b \cdot \hat{g}(\xi).$$

- **Derivation**
  If $g(x) = f'(x)$, then

  $$\hat{g}(\xi) = i\xi \hat{f}(\xi).$$

- **Convolution theorem**
  If $f(x)$ and $g(x)$ are integrable functions with Fourier transforms $\hat{f}(\xi)$ and $\hat{g}(\xi)$ respectively, then the Fourier transform of the convolution is given by the product of the Fourier transforms $\hat{f}(\xi)$ and $\hat{g}(\xi)$. It means that if:

  $$h(x) = f(x) * g(x) = \int_{-\infty}^{+\infty} f(y) g(x-y) dy,$$

  where $*$ denotes the convolution operation, then

  $$\hat{h}(\xi) = \hat{f}(\xi) \cdot \hat{g}(\xi).$$

Discrete Fourier transform

The definition of *discrete Fourier transform* (DFT) is quite similar with the basic Fourier transform. The sequence of N complex numbers $x_0, x_1, ..., x_{N-1}$ is transformed into another sequence of N complex numbers according to the DFT formula:

$$X_\xi = \sum_{n=0}^{N-1} x_n \cdot e^{-2\pi i \xi n/N}, \tag{2.5}$$

where the *N-points inverse DFT (IDFT)* is defined as follows:

$$x_n = \frac{1}{N} \sum_{\xi=0}^{N-1} X_\xi \cdot e^{i2\pi \xi n/N}. \tag{2.6}$$

The three dimensional problems will be discussed in this study, so the 3-D formula of DFT and IDFT are presented as well. The forward 3-D DFT are:

$$X_{k_x k_y k_z} = \sum_{j_x=0}^{N_x-1} \sum_{j_y=0}^{N_y-1} \sum_{j_z=0}^{N_z-1} x_{j_x j_y j_z} \cdot e^{-i2\pi k_x j_x/N_x} e^{-i2\pi k_y j_y/N_y} e^{-i2\pi k_z j_z/N_z}, \tag{2.7}$$

and the inverse form:

$$x_{j_x j_y j_z} = \sum_{k_x=0}^{N_x-1} \sum_{k_y=0}^{N_y-1} \sum_{k_z=0}^{N_z-1} X_{k_x k_y k_z} \cdot e^{-i2\pi j_x k_x/N_x} e^{-i2\pi j_y k_y/N_y} e^{-i2\pi j_z k_z/N_z}. \tag{2.8}$$

Fast Fourier transform

As mentioned above, *Fast Fourier transform* (FFT) computes the DFT and produces exactly the same result as implementing the DFT definition directly. The only difference is that FFT is much faster than the DFT. It can be seen from the definition of DFT (2.5) that it requires $O(N^2)$ operations by N outputs of X_k and a N terms summation. FFT only takes $O(N \cdot logN)$ operations as computing the same results. The time costs of FFT and DFT for solving the same transform problem with N points can be denoted as

$$\lambda = \frac{Time\,of\,FFT}{Time\,of\,DFT} \approx \frac{N \cot logN}{N^2} = \frac{logN}{N}. \tag{2.9}$$

2.1.2 Green's function for heterogeneous materials

The initial idea of the direct numerical approach based upon fast Fourier transforms is to use directly the image of a real composite material by assigning the mechanical properties individually to those pixels in 2-D or voxels in 3-D. Afterward, the numerical algorithm for certain mechanical problems is implemented to those individual points separately through the whole field. Specifically, a set of partial differential equations governing the mechanical problems at each material point are solved individually so that the local field can be known in details. From this point of view, the definition of the overall behavior of a composite medium is obtained by taking into account all response of each point in the whole domain which is so-called 'local problem' on a representative volume element (R.V.E).

An integral equation formulation

To begin with, a classical resolution of the heterogeneous material is introduced according to the contributions in (Castañeda, 2005). For simplicity, a linear elastic heterogeneous medium which occupies a domain Ω with boundary $\partial\Omega$ was studied in the example. The elasticity tensor is noted as $\mathbb{C}(\boldsymbol{x})$ strictly depending on the local position, and the governing equations can be rewritten here in tensor form and in terms of components with respect to a Cartesian coordinate system, respectively:

$$\boldsymbol{\varepsilon}(x) = \frac{1}{2}(\nabla \boldsymbol{u}(x) + (\nabla \boldsymbol{u}(x))^T), \quad \text{or} \quad \varepsilon_{ij}(x) = \frac{1}{2}(u_{i,j}(x) + u_{j,i}(x)), \tag{2.10}$$

$$\boldsymbol{\sigma}(x) = \mathbb{C}(x) : \boldsymbol{\varepsilon}(x), \quad \text{or} \quad \sigma_{ij}(x) = C_{ijkl}(x)\varepsilon_{kl}(x), \tag{2.11}$$

and

$$div\boldsymbol{\sigma}(x) + \boldsymbol{b} = \boldsymbol{0}, \quad \text{or} \quad \sigma_{ij,j}(x) + b_i = 0. \tag{2.12}$$

The prescribed displacement boundary condition is first considered:

$$\boldsymbol{u}(x) = \boldsymbol{u_0} \quad \forall \boldsymbol{x} \in \partial\Omega, \tag{2.13}$$

where $\boldsymbol{u}_0$ is known on the boundary $\partial\Omega$.

The key technique is to introduce a homogeneous "reference medium" with constant stiffness tensor $\mathbb{C}^0$ prescribed under a polarization field which is used to represent the heterogeneties of the material. As is illustrated in Fig. 2.1 that

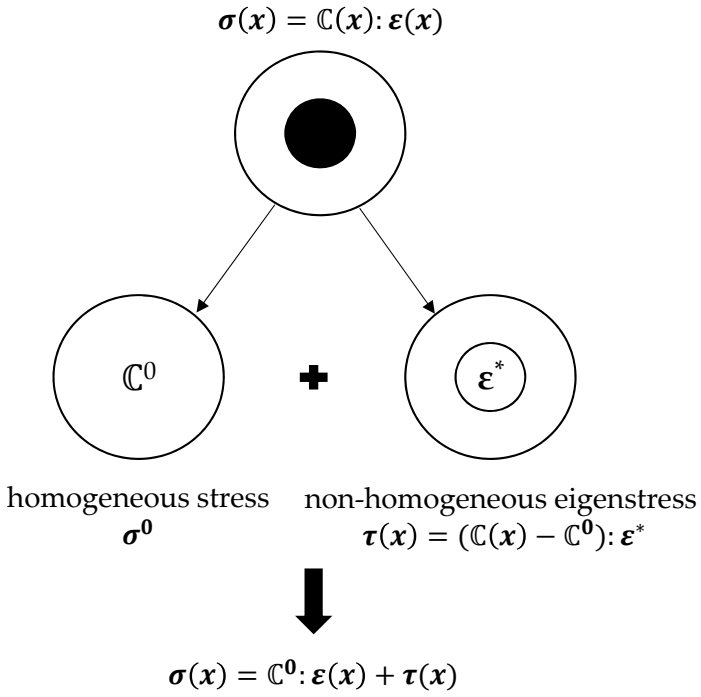

Fig. 2.1 Schematics of homogeneous reference medium to solve boundary value problems for heterogeneous materials.

the initial heterogeneous materials are splited into two individual materials: a homogeneous one with elastic constant $\mathbb{C}^0$ and another one with an eigenstrain $\boldsymbol{\varepsilon}^*$ within an inclusion. It is worthy mentioning that the second problem is exactly the Eshelby's inclusion problem. The eigenstrain $\boldsymbol{\varepsilon}^*$ induces a polarization field $\boldsymbol{\tau}$ as the difference between the stress in the actual heterogeneous material and the stress in the homogeneous material:

$$\boldsymbol{\tau}(x) = (\mathbb{C}(x) - \mathbb{C}^0) : \boldsymbol{\varepsilon}(x), \quad \text{or} \quad \tau_{ij}(x) = (C_{ijkl}(x) - C^0_{ijkl}) : \varepsilon_{kl}(x) \tag{2.14}$$

and the constitutive equation is then rewritten as

$$\boldsymbol{\sigma}(x) = \mathbb{C}^0 : \boldsymbol{\varepsilon}(x) + \boldsymbol{\tau}(x), \quad \text{or} \quad \sigma_{ij}(x) = C^0_{ijkl} : \varepsilon_{kl}(x) + \tau_{ij}(x) \tag{2.15}$$

Thus, the equilibrium equation can be then expressed as the relation between the stress and the displacement directly by combining those governing equations stated above:

$$div(\mathbb{C}^0 \nabla \boldsymbol{u}(x)) + div \cdot \boldsymbol{\tau}(x) + \boldsymbol{b} = \boldsymbol{0}, \quad \text{or} \quad (C^0_{ijkl} u_{k,l}(x))_{,j} + \tau_{ij,j}(x) + b_i = 0. \tag{2.16}$$

Now the problem of a heterogeneous material can be considered as a homogeneous material with a constant elasticity tensor $\mathbb{C}^0$ in the domain Ω subjected to a body force $\nabla\cdot\boldsymbol{\tau}+\boldsymbol{b}$ with the same boundary condition as before in (2.13). Therefore, the problem can be split into two problems according to two different body force: (1) a homogeneous elastic material with body force $\boldsymbol{b}$; (2) a homogeneous elastic material with body force $\boldsymbol{\tau}$. The first problem can be easily solved as a general boundary value problem, however, the second problem is exact the Eshelby's problem and is difficult to find an explicit solution due to the fact that $\boldsymbol{\tau}$ is a function of displacement $\boldsymbol{u}$ as well. An alternative method by making use of the relevant Green's function of the problem is introduced and equation (2.16) can be solved as

$$\frac{\partial}{\partial x_j}\left[C^0_{ijkl}\frac{\partial G^0_{kp}}{\partial x_l}(\boldsymbol{x},\boldsymbol{x}')\right]+\delta_{ip}\delta(\boldsymbol{x}-\boldsymbol{x}')=0,\qquad \forall\boldsymbol{x}\in\Omega \tag{2.17}$$

and

$$G_{ip}(\boldsymbol{x},\boldsymbol{x}')=0,\qquad \forall\boldsymbol{x}\in\partial\Omega. \tag{2.18}$$

where $\boldsymbol{G}$ is so-called *Green's function* associated with the homogenized material with stiffness tensor $\mathbb{C}^0$ in the domain Ω. After some mathematical manipulations (see Appendix 1) the solution of the problem (2.16) can be expressed by the *Green operator* Γ^0 associated with $\mathbb{C}^0$ and the polarization field τ:

$$\varepsilon_{ij}(\boldsymbol{x})=\varepsilon^0_{ij}(\boldsymbol{x})-\int_\Omega \Gamma^0_{ijpq}(\boldsymbol{x},\boldsymbol{x}')\tau_{pq}(\boldsymbol{x}')d\boldsymbol{x}', \tag{2.19}$$

where

$$\Gamma^0_{ijpq}(\boldsymbol{x},\boldsymbol{x}')=\left.\frac{\partial G^0_{ip}}{\partial x_j\partial x'_q}\right|_{ijpq}. \tag{2.20}$$

The last term of equation (2.19) is exactly the definition of convolution on the Green's function Γ^0 and the polarization field $\boldsymbol{\tau}$:

$$\Gamma^0*\boldsymbol{\tau}=\int_\Omega \Gamma^0_{ijpq}(\boldsymbol{x},\boldsymbol{x}')\tau_{pq}(\boldsymbol{x}')d\boldsymbol{x}', \tag{2.21}$$

finally, the solution of equation (2.16) becomes

$$(\mathbb{C}-\mathbb{C}^0)^{-1}\boldsymbol{\tau}+\Gamma^0*\boldsymbol{\tau}=\varepsilon_0, \tag{2.22}$$

and this integral equation is well known as the *Lippman-Schwinger* equation, as discussed by (Kröner, 1977) and the details about the explicit form of the Green's function $\boldsymbol{G}^0$ and associated operator Γ^0 can be find in a number of contributions, only cite a few here (Castañeda, 2005; Milton, 2002; Mura, 1987; Nguyen et al., 2008). It is worth noting that the Green's operator is explicitly known in the Fourier space (Moulinec and Suquet, 1998) and the details on the expression for different cases, *e.g.* isotropic and anisotropic materials, will be presented in the next subsection. The merit of explicit form makes the problems on the heterogeneous materials to be capable of being resolved by making use of the Green's operator coupling with the Fourier transforms. The eligible approach is fully reviewed based on a local problem in the following.

Local problem

An auxiliary problem introduced in (Moulinec and Suquet, 1998) is recalled here as an example of application of FFT method. A homogeneous material with elasticity tensor $\mathbb{C}^0$ subjected to a polarization field $\boldsymbol{\tau}$ submitted to a prescribed macroscopic strain $\boldsymbol{E}$ and periodic boundary conditions applied. Interfaces among all different phases are assumed to be perfectly bonded. With all those assumptions it now becomes a well-posed local problem on a representative volume element (r.v.e.) with the volume of V. The notation used hereinafter follows the convention in (Moulinec and Suquet, 1998). The local strain field $\boldsymbol{\varepsilon}(\boldsymbol{u}(\boldsymbol{x}))$ is considered as two terms:

$$\boldsymbol{\varepsilon}(\boldsymbol{u}(\boldsymbol{x})) = \boldsymbol{\varepsilon}(\boldsymbol{u}^*(\boldsymbol{x})) + \boldsymbol{E}, \tag{2.23}$$

where $\boldsymbol{E}$ denotes the average of the strain field for the homogeneous part by the volumetric averaging operator $\langle\cdot\rangle$ on the whole unit cell:

$$< \boldsymbol{\varepsilon} >= \boldsymbol{E}, \tag{2.24}$$

and $\boldsymbol{\varepsilon}(\boldsymbol{u}^*(\boldsymbol{x}))$ implies the presence of heterogeneities and its average vanishes due to the fact that the displacement filed u^* is periodic.

$$< \boldsymbol{\varepsilon}(\boldsymbol{u}^*(\boldsymbol{x})) >= 0. \tag{2.25}$$

The governing equations of the closed problem is then expressed as:

$$\begin{cases} \boldsymbol{\sigma}(\boldsymbol{x}) = \frac{\partial w}{\partial \boldsymbol{\varepsilon}}(\boldsymbol{x}) & \forall \boldsymbol{x} \in V \\ \boldsymbol{div}\boldsymbol{\sigma}(\boldsymbol{x}) = 0 & \forall \boldsymbol{x} \in V, \quad u^*\#, \quad \boldsymbol{\sigma}\cdot n - \# \\ \boldsymbol{\varepsilon}(\boldsymbol{x}) = \frac{1}{2}(\nabla \boldsymbol{u}^*(\boldsymbol{x}) + \nabla^T \boldsymbol{u}^*(\boldsymbol{x})) + \boldsymbol{E} & \forall \boldsymbol{x} \in V \end{cases} \tag{2.26}$$

where w is a free energy in function of stain $\boldsymbol{\varepsilon}$ and V denotes the volume element, $\boldsymbol{u}^*\#$ represents periodicity, and the traction $\boldsymbol{\sigma}\cdot\boldsymbol{n}$ is anti-periodic noted as $\boldsymbol{\sigma}\cdot\boldsymbol{n} - \#$.

Apply the "reference medium" method a homogeneous material with stiffness tensor $\mathbb{C}^0$ is introduced and a polarization field $\boldsymbol{\tau}(\boldsymbol{x})$ is defined as the difference between the actual stress and the reference stress field:

$$\boldsymbol{\tau}(\boldsymbol{x}) = \frac{\partial w}{\partial \boldsymbol{\varepsilon}}(\boldsymbol{x}) - \mathbb{C} : \boldsymbol{\varepsilon}(\boldsymbol{x}). \tag{2.27}$$

The solution of the problem can be simply expressed according to the method proposed in equation (2.22):

$$\boldsymbol{\varepsilon}(\boldsymbol{u}^*(\boldsymbol{x})) = -\Gamma^0 * \boldsymbol{\tau}(\boldsymbol{x}) + \boldsymbol{E}, \qquad \forall \boldsymbol{x} \in V. \tag{2.28}$$

Despite the fact that the polarization field $\boldsymbol{\tau}$ is known and the operator Γ^0 can be deduced explicitly, the convolution operator is extremely difficult to solve directly. Nevertheless, the most common fast method for convolution operator is to make use of the Fast Fourier transform (FFT) algorithm via the *Convolution Theorem* mentioned in previous subsection. By applying the FFT algorithm the convolution operator is transformed as a simple production in Fourier spaces:

$$\hat{\boldsymbol{\varepsilon}}(\boldsymbol{\xi}) = -\hat{\Gamma}^0(\boldsymbol{\xi}) : \hat{\boldsymbol{\tau}}(\boldsymbol{\xi}) \qquad \boldsymbol{\xi} \neq \boldsymbol{0}, \quad \hat{\boldsymbol{\varepsilon}}(\boldsymbol{0}) = \boldsymbol{E}, \tag{2.29}$$

where the Green's operator $\hat{\Gamma}^0$ can be derived explicitly in Fourier space for medium with knowing mechanical properties. For example, an isotropic material with Lamé coefficients λ^0 and μ^0, the Green's operator can be expressed explicitly in the form:

$$\hat{\Gamma}_{khij}(\boldsymbol{\xi}) = \frac{1}{4\mu^0|\boldsymbol{\xi}|^2}(\delta_{ki}\xi_h\xi_j + \delta_{hi}\xi_k\xi_j + \delta_{kj}\xi_h\xi_i + \delta_{hj}\xi_k\xi_i) - \frac{\lambda^0 + \mu^0}{\mu^0(\lambda^0 + 2\mu^0)}\frac{\xi_i\xi_j\xi_k\xi_h}{|\boldsymbol{\xi}|^4}. \tag{2.30}$$

Therefore, after such mathematical transforms the problem is significantly simplified and can be straightforwardly performed into numerical algorithm in Fourier

space. The means of Green's operator or Green's function coupled with fast Fourier transforms (FFT) provides a very efficient theoretical approach to solve the mechanical problems of composite heterogeneous material. Meanwhile, significant numerical progress has been made in this field as well by many researchers, such as the accelerated scheme for the composite with high contrast (Michel et al., 2001) and the polarization based iterative scheme (Monchiet and Bonnet, 2012).

2.1.3 Numerical algorithms based on FFT approach

As is discussed before, the intent of the numerical method based on FFT is to directly use the digital pixels of an image of a real composite material to simulate the complex micro-structures. The image is discretized into pixels which are assigned mechanical properties according to their positions which represent the properties of the actual medium. The process of discretization can be implemented by the algorithm of image process and the coordinates $\boldsymbol{x}$ in real space are corresponding to the frequency $\boldsymbol{\xi}$ in Fourier space. Therefore, all the governing formula in real space can be then transformed into Fourier space according to the discrete Fourier transforms by applying on positions of each pixel. As is known before, the whole procedure can be efficiently implemented by FFT. The "basic scheme" is briefly repeated here as an example to implement the method.

The solution (Eq. 2.28) of the problem presented before is recalled here:

$$\boldsymbol{\varepsilon}(\boldsymbol{u}(\boldsymbol{x})) = -\Gamma^0(\boldsymbol{x}) * \boldsymbol{\tau}(\boldsymbol{u}(\boldsymbol{x})) + \boldsymbol{E}, \tag{2.31}$$

and an iterative scheme based on fixed-point algorithm was proposed in (Moulinec and Suquet, 1998):

$$\boldsymbol{\varepsilon}(\boldsymbol{u}^{i+1}) = -\Gamma^0 * \boldsymbol{\tau}(\boldsymbol{u}^i) + \boldsymbol{E}. \tag{2.32}$$

After applying the FFT, the equation is transformed into Fourier space and leads to:

$$\hat{\boldsymbol{\varepsilon}}^{i+1}(\boldsymbol{\xi}) = -\hat{\Gamma}^0(\boldsymbol{\xi}) : \hat{\boldsymbol{\varepsilon}}^i(\boldsymbol{\xi}) \qquad \forall \boldsymbol{\xi} \neq 0 \quad \text{and} \quad \hat{\boldsymbol{\varepsilon}}^{i+1}(\boldsymbol{0}) = \boldsymbol{E}, \tag{2.33}$$

where $\hat{\boldsymbol{\tau}}$ and $\hat{\Gamma}^0$ are both known explicitly in Fourier space.

As the iterative scheme of the local problem is proposed, the algorithm for the whole field can be then implemented at each loading step according to the discretization procedure of the unit cell to regular grid of points with the discrete algorithm. The basic scheme is recalled here in the discrete form and the superscript

denotes the iteration in each loading step:

$$\begin{cases} \text{Initialization:} & \boldsymbol{\varepsilon}^0(\boldsymbol{x_p}) = \boldsymbol{E} \qquad \forall \boldsymbol{x}_p \in \Omega, \\ & \boldsymbol{\sigma}^0(\boldsymbol{x}_p) = \mathbb{C}(\boldsymbol{x}_p) : \boldsymbol{\varepsilon}^0(\boldsymbol{x}_p) \qquad \forall \boldsymbol{x}_p \in \Omega, \\ \text{Iterate } i+1 & \text{the previous } \boldsymbol{\varepsilon}^i \text{and } \boldsymbol{\sigma}^i \text{ are known at each position } \boldsymbol{x}_p \\ \quad 1) & \hat{\boldsymbol{\sigma}}^i = \mathcal{F}(\boldsymbol{\sigma}^i) \\ \quad 2) & \text{Verify the convergence and update the stress/strain} \\ \quad 3) & \hat{\boldsymbol{\varepsilon}}^{i+1}(\boldsymbol{\xi}_p) = \hat{\boldsymbol{\varepsilon}}^i(\boldsymbol{\xi}_p) - \hat{\Gamma}^0(\boldsymbol{\xi}_p) : \hat{\boldsymbol{\sigma}}^i(\boldsymbol{\xi}_p) \qquad \forall \boldsymbol{\xi}_p \neq \boldsymbol{0}, \quad \hat{\boldsymbol{\varepsilon}}^{i+1}(\boldsymbol{0}) = \boldsymbol{E} \\ \quad 4) & \boldsymbol{\varepsilon}^{i+1} = \mathcal{F}^{-1}(\hat{\boldsymbol{\varepsilon}}^{i+1}) \\ \quad 5) & \boldsymbol{\sigma}^{i+1}(\boldsymbol{x}_p) = \mathbb{C}(\boldsymbol{x}_p) : \boldsymbol{\varepsilon}^{i+1}(\boldsymbol{x}_p) \quad \forall \boldsymbol{x}_p \in \Omega \end{cases} \tag{2.34}$$

In these relations, $\boldsymbol{x}_p$ and $\boldsymbol{\xi}_p$ denote the coordinates in real space and Fourier space, respectively. $\mathbb{C}(\boldsymbol{x}_d)$ implies that the constitutive relation strongly depends on the local position of the point which is applying to update the strain and stress. The symbol $\mathcal{F}$ and $\mathcal{F}^{-1}$ represent correspondingly the FFT and inverse FFT operators. And the step 3) of the algorithm is simplified by the properties of Green's operator:

$$\Gamma^0 * (\mathbb{C}^0 : \boldsymbol{\varepsilon}) = \boldsymbol{\varepsilon}. \tag{2.35}$$

which gives the form of (3) in the scheme by transforming into Fourier space.

The convergence condition is controlled by the equilibrium equation and performed in Fourier space to avoid the difficulty of the computation for the differential operator:

$$err^i = \frac{< \|div\boldsymbol{\sigma}^i(\boldsymbol{x}_d)\|^2 >^{1/2}}{\| < \boldsymbol{\sigma}^i(\boldsymbol{x}_d) > \|} = \frac{< \|\boldsymbol{\xi} \cdot \hat{\boldsymbol{\sigma}}^i(\boldsymbol{x}_d)\|^2 >^{1/2}}{\|\hat{\boldsymbol{\sigma}}^i(\boldsymbol{0})\|} \leqslant w, \tag{2.36}$$

and the matrix 2-norm is utilized here as the norm of the second order tensor. w is a chosen value of convergence tolerance.

The choice of the reference stiffness tensor $\mathbb{C}^0$ (with Lamé coefficients λ^0 and μ^0) is arbitrary, however, it affects significantly the rate of the convergence. In practice, the best rate of convergence is provided with the value (Moulinec and Suquet, 1998)

$$\begin{aligned}\lambda^0 &= \frac{1}{2}(\inf_{x\in V}\lambda(x)+\sup_{x\in V}\lambda(x))\\ \mu^0 &= \frac{1}{2}(\inf_{x\in V}\mu(x)+\sup_{x\in V}\mu(x))\end{aligned} \tag{2.37}$$

Discrete of FFT model

In the above FFT based numerical model, a continuous polarization tensor field should be determined. In practice, in view of its numerical implementation, a discrete FFT based model is defined. We shall determine a discrete distribution of polarization tensor at a limited number of points. Therefore, the unit cell is meshed by a regular grid composed of a limit number of point in each direction in real space. The unit cell is discretized into a regular grid composed of $N1\times N2\times N3$ voxels in three dimensional case. The coordinates of pixels are denoted by $x_p(i_1,i_2,i_3)$ which are linked to the coordinates, $\xi(i_1,i_2,i_3)$, in Fourier space correspondingly by the grid of the model. The number of points in each direction depends on the choice of resolution. The relationships between the two coordinates and the grid information are given by:

$$x_p(i_i,i_2,i_3) = i_k\cdot\frac{T_k}{N_k}, \qquad i_k = 0,1,...,N_{k-1}, \quad k=1,2,3. \tag{2.38}$$

and the coordinates of $\xi(i_1,i_2,i_3)$ for the case of N_k is even

$$\xi(i_1,i_2,i_3) = (i_k-\frac{N_k-1}{2})\frac{1}{T_k} \tag{2.39}$$

and the case of N_k is odd

$$\xi(i_1,i_2,i_3) = (i_k-\frac{N_k}{2}+1)\frac{1}{T_k} \tag{2.40}$$

where T_k is the period of the model in the kth direction ($k=1,2,3$).

Therefore, the iterative numerical algorithm presented above will be applied to each discrete point $\boldsymbol{x}_p$ in real space or $\boldsymbol{\xi}_p$ in Fourier space.

Extension to nonlinear materials

The above numerical method for a linear inhomogeneous material is now extended to nonlinear heterogeneous materials. It is generally convenient to express nonlinear constitutive relations in an incremental form. For this purpose, the total loading path is divided into a limit number of steps N. Starting from the initial conditions, at the end of the step n, the local fields of stress, strain and internal variables $(\boldsymbol{\sigma}^n, \boldsymbol{\varepsilon}^n, \boldsymbol{V}^n)$ are all known. Considering now the loading step $n+1$, an incremental of macroscopic strain $\Delta \boldsymbol{E}^{n+1}$ is applied to the unit cell. The problem to be solved is to find the corresponding macroscopic stress increment $\Delta \boldsymbol{\Sigma}^{n+1}$ by using nonlinear local constitutive relations.

To this end, the iterative algorithm presented above is now applied to each loading step. Consider here the time-independent behavior only. Without loosing the generality, the local nonlinear constitutive relations can be expressed in the following incremental form:

$$\Delta \boldsymbol{\sigma}(\boldsymbol{x}) = \mathbb{C}^{tan}(\boldsymbol{x}) : \Delta \varepsilon(\boldsymbol{x}), \tag{2.41}$$

where the forth order tensor $\mathbb{C}^{tan}(\boldsymbol{x})$ denotes the tangent operator which depends on the loading history and loading direction.

Accordingly, the FFT-based iterative numerical algorithm for nonlinear heterogeneous materials at the loading step $n+1$ is defined by (for the sake of simplicity, the step index $(n+1)$ in omitted in the iteration loop):

$$\begin{cases}
\text{Initialization:} & \boldsymbol{\varepsilon}^{(n+1)0}(\boldsymbol{x_p}) = \boldsymbol{\varepsilon}^n(\boldsymbol{x_p}) + \Delta \boldsymbol{E}^{n+1} \qquad \forall \boldsymbol{x}_p \in \Omega, \\
& \boldsymbol{\sigma}^{(n+1)0}(\boldsymbol{x}_p) = \boldsymbol{\sigma}^n(\boldsymbol{x}_p) + \mathbb{C}^{tan(n+1)0}(\boldsymbol{x_p}) : \Delta \boldsymbol{\varepsilon}^{(n+1)0}(\boldsymbol{x_p}) \\
\text{Iterate } i+1 & \text{the previous } \boldsymbol{\varepsilon}^i \text{and } \boldsymbol{\sigma}^i \text{ are known at each position } \boldsymbol{x}_p \\
\quad a) & \hat{\boldsymbol{\sigma}}^i = \mathcal{F}(\boldsymbol{\sigma}^i) \\
\quad b) & \text{Verify the convergence and update the stress/strain} \\
\quad c) & \hat{\boldsymbol{\varepsilon}}^{i+1}(\boldsymbol{\xi}_p) = \hat{\boldsymbol{\varepsilon}}^i(\boldsymbol{\xi}_p) - \hat{\Gamma}^0(\boldsymbol{\xi}_p) : \hat{\boldsymbol{\sigma}}^i(\boldsymbol{\xi}_p) \qquad \forall \boldsymbol{\xi}_p \neq \boldsymbol{0}, \quad \hat{\boldsymbol{\varepsilon}}^{i+1}(\boldsymbol{0}) = \boldsymbol{E}^{(n+1)} \\
\quad d) & \boldsymbol{\varepsilon}^{i+1} = \mathcal{F}^{-1}(\hat{\boldsymbol{\varepsilon}}^{i+1}) \\
\quad e) & \boldsymbol{\sigma}^{i+1}(\boldsymbol{x}_p) = \boldsymbol{\sigma}^n(\boldsymbol{x}_p) + \mathbb{C}^{tan(i+1)}(\boldsymbol{x_p}) : \Delta \boldsymbol{\varepsilon}^{i+1}(\boldsymbol{x_p}) \quad \forall \boldsymbol{x}_p \in \Omega \\
\quad f) & \text{update } \boldsymbol{V}^{i+1} \text{ from } \boldsymbol{\varepsilon}^{i+1} \text{ and } \boldsymbol{V}^i
\end{cases} \tag{2.42}$$

Accelerated schemes

It is noted that the FFT based method requires high computational memory and cost due to the convergence rate, especial for some extreme case, for instance, composite with high contrast or infinite contrast (containing voids or rigid inclusions). Thus, the approach has been improved to accelerate the convergence rate by many researches. Eyre and Milton (1999) firstly introduced an accelerated scheme by reformulating the key iterative procedure of basic scheme to avoid negative stiffness for the reference medium. Michel et al. (2001) proposed a new scheme based on augmented Lagrangian method to deal with the high contrast composite coupled with the nonlinear materials. A polarization based FFT iterative scheme was proposed by (Monchiet and Bonnet, 2012) to compute the effective properties of composite with arbitrary contrast and overcame the highly contrast of the mechanical properties between individual phases by considering both strain and stress. The investigation of (Moulinec and Silva, 2014) found that those accelerated schemes are strongly related and can be summarized to be the particular cases for the polarization-based scheme. The unified scheme is recalled in the following based on the previous work of (Moulinec and Silva, 2014):

$$
\begin{cases}
\text{Iterate } i+1 & \text{the previous } \boldsymbol{\varepsilon}^i \text{and } \boldsymbol{\sigma}^i \text{ known} \\
1) & \boldsymbol{s}_a^i(\boldsymbol{x}) = \boldsymbol{\sigma}^i(\boldsymbol{x}) + (1-\beta)\cdot\mathbb{C}^0 : \boldsymbol{\varepsilon}^i(\boldsymbol{x}) \\
 & \boldsymbol{s}_b^i(\boldsymbol{x}) = \alpha\boldsymbol{\sigma}^i(\boldsymbol{x}) - \beta\cdot\mathbb{C}^0 : \boldsymbol{\varepsilon}^i(\boldsymbol{x}) \\
2) & \hat{\boldsymbol{s}}_b^i = \mathcal{F}(\boldsymbol{s}_b^i) \\
3) & \hat{\boldsymbol{\varepsilon}}_b^i(\boldsymbol{\xi}) = -\hat{\Gamma}^0(\boldsymbol{\xi}) : \hat{\boldsymbol{s}}_b^i(\boldsymbol{\xi}_p) \qquad \forall \boldsymbol{\xi} \neq \boldsymbol{0}, \quad \hat{\boldsymbol{\varepsilon}}_b^{i+1}(\boldsymbol{0}) = \beta \boldsymbol{E} \\
4) & \boldsymbol{\varepsilon}_b^{i+1}(\boldsymbol{x}) = \mathcal{F}^{-1}(\hat{\boldsymbol{\varepsilon}}_b^i) \\
5) & \boldsymbol{e}^{i+1}(\boldsymbol{x}) = (\mathbb{C}(\boldsymbol{x}) + \mathbb{C}_0)^{-1} : (\boldsymbol{s}_a^i(\boldsymbol{x}) + \mathbb{C}^0 : \boldsymbol{\varepsilon}_b^i(\boldsymbol{x})) \\
6) & \boldsymbol{\sigma}^{i+1}(\boldsymbol{x}) = \mathbb{C}(\boldsymbol{x}) : \boldsymbol{\varepsilon}^{i+1}(\boldsymbol{x}) \\
7) & \text{Verify the convergence}
\end{cases}
\tag{2.43}
$$

It is found that the polarization scheme is the more adaptable for both strain based and stress based iterative scheme. As $\alpha = \beta = 1$ the scheme tends to be the augmented Lagrangian scheme and $\alpha = \beta = 2$ appears to be the Eyre-Milton scheme. The convergence rate is influenced dramatically by the contrast of the material properties between different phases. It is proved in the work of (Monchiet

and Bonnet, 2012) that the strain based iterative scheme diverges in the cases of rigid inclusions but converges in the cases of voided materials. On the contrary, the stress based iterative scheme converges rapidly in the case of composites with rigid inclusions but diverges for the voided composites. The polarization scheme is proved also that the composite containing both rigid inclusions and voids (for instance, $\alpha = \beta = 1.5$) can be studied without the problem of convergence. A test based on the present strain-based scheme is performed in Fig.2.2. The curve shows that the strain based formulations has a better convergence for composite with soft inclusions. It is indicated that the strain based method has a satisfactory convergence for the material containing voids as a specific case.

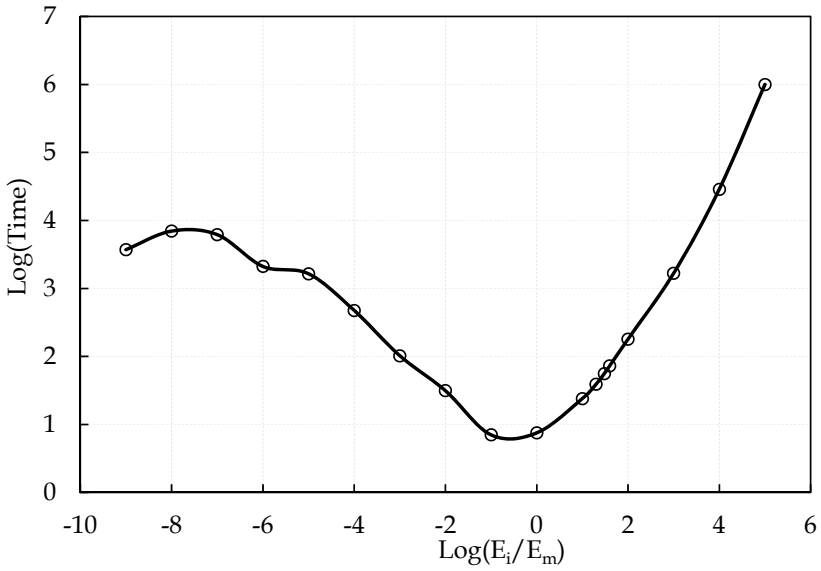

Fig. 2.2 Computational time consuming at convergence as a function of the contrasts between the phases for strain based formulations.

Remarks

So far the principles of the FFT method have been discussed in detail and the main ideas are stated here as a summary of the method. A composite material is discretized into a regular grid of nodes and each node have a unique coordinate in real space and in Fourier space as well as specific mechanical properties. For example, every node have a particular stiffness tensor to represent the local constitutive relation of the local mechanical properties of the composite. The differences of the local properties distinguish the different phases of the composite. The FFT method is then implemented by a discrete algorithm to solve the partial differential equations on

each node in the whole domain according to their local material properties. Hereafter, the overall response of the completed field are homogenized by the means of the volumetric average on all the nodes in the whole field:

$$\bar{f} =< f >= \frac{1}{|\Omega|}\int_{\Omega} f(\boldsymbol{x})d\boldsymbol{x}, \tag{2.44}$$

or equivalently in the discrete form:

$$\bar{f} =< f >= \frac{1}{|\Omega|}\sum_{x=0}^{N-1} f_x. \tag{2.45}$$

Meanwhile, different constitutive laws can be simply performed on every individual phase and the linear or non linear cases can be effectively extended as well. The convergence rate and the accuracy of the FFT method will be investigated in the next section by several tests.

2.2 Numerical applications

The primary principles and basic algorithms of the Fast Fourier Transforms method have been thoroughly stated in the former section. In this section, some examples of numerical applications are performed as a validation of the implementation of the present method.

2.2.1 Composites reinforced by unidirectional long fibers

The first example is to compare with the numerical applications in (Moulinec and Suquet, 1998) to validate the present approach. The computational structural is a two dimensional problem which consists of matrix reinforced by unidirectional long fibers aligned along the x_3 direction (see Fig. 2.3). The representative volume element (R.V.E.), unit cell for periodic microstructure, is chosen as a square matrix with a centered circle fiber. The matrix is considered as an elastoplastic model with Young's modulus and Poison ratio:

$$E_m = 68.9GPa,\ \mu_m = 0.35, \tag{2.46}$$

and the plastic behaviors characterized by Von Mises criterion with linear hardening

$$f = \sigma_{eq} - R(\gamma), R(\gamma) = \sigma_0 + H\gamma, \tag{2.47}$$

where $R(\gamma)$ is the isotropic hardening function with the hardening variable γ which is calculated by the accumulated equivalent plastic strain:

$$\dot{\gamma} = \sqrt{\frac{2}{3}\dot{\boldsymbol{\varepsilon}}^p : \dot{\boldsymbol{\varepsilon}}^p}, \tag{2.48}$$

in which $\dot{\boldsymbol{\varepsilon}}^p$ is the deviator plastic strain rate.

The fibers are assumed to be perfectly elastic, isotropic, and governed by the elastic parameters, Young's modulus and Poisson ratio:

$$E_f = 400GPa, \mu_f = 0.23. \tag{2.49}$$

The fiber volume fraction is 47.5%. The hardening modulus can be $H = 0$ for perfectly plasticity and $H = 1171MPa$ for plastic with isotropic linear hardening.

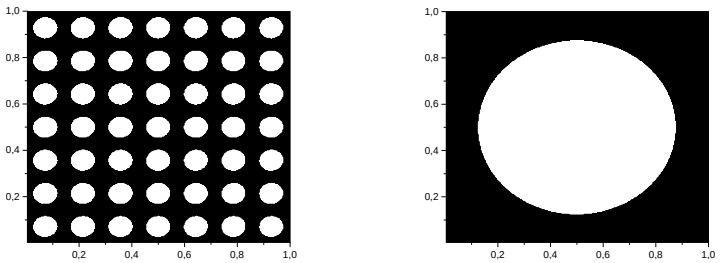

Fig. 2.3 Microstructures of fibers reinforced composites with fiber volume fraction f = 47.5% simulated with FFT method. Spatial resolutions: 256×256 pixels. (a) Periodic microstructure containing 49 circular fibers; (b) Unit cell containing one fiber.

The overall properties of the composite are performed in various spatial resolution, $N_1 * N_2$, which are the number of pixels contained in each direction, respectively. For instance, N can be 64, 128, 256, 512 and even up to 1024 due to the high performance of the server computational tools.

The comparison of the present FFT approach with the proposed method in Moulinec and Suquet (1998) is shown in Fig. 2.4 and the influence of the spatial resolutions on the overall response is analyzed as well. It can be seen that the present method has a very good agreement at high spatial resolutions with the reference

solution for both perfectly elastic fiber case and that of matrix with isotropic hardening. It is noted that the influence of the spatial resolution for the case of matrix with perfect plastic behavior is much more remarkable. The study on the effects of the spatial resolution also coincides with the discussion in their paper that the higher spatial resolutions provide better results. Nevertheless, the high spatial resolutions requires large computer memories and time consuming for the calculations. It is noted in the Fig. 2.4 that 128×128 has well met the requirements of the accuracy while 256×256 provides slightly better results. However, it costs much more computer memories and computational time, therefore, the spatial resolutions 128×128 is set to be the standard one in the following computations.

The second example is performed on the model with the same geometry (fiber reinforced composite) under uniaxial tension loading but with different material properties. The plastic behavior of the matrix is also governed by Von Mises criterion and the fibers remain perfectly linear elastic with a different volume fraction $f = 25\%$. The material parameters (seen in table 2.1 and 2.2) are assigned the same as the plain strain problem used in Michel and Suquet (2004) as following:

Table 2.1 Material parameters of the fibers

E_f	μ_f
$400GPa$	0.25

Table 2.2 Material parameters of the solid matrix

E_m	μ_m	σ_0	H	m
$75GPa$	0.30	$75MPa$	$416.5MPa$	0.3895

The results of the present FFT approach are compared with the reference solution in Michel and Suquet (2004) and the one provided by FEM software ABAQUS in Figure 2.5. It is noted that the present results are consistent well with the reference solutions.

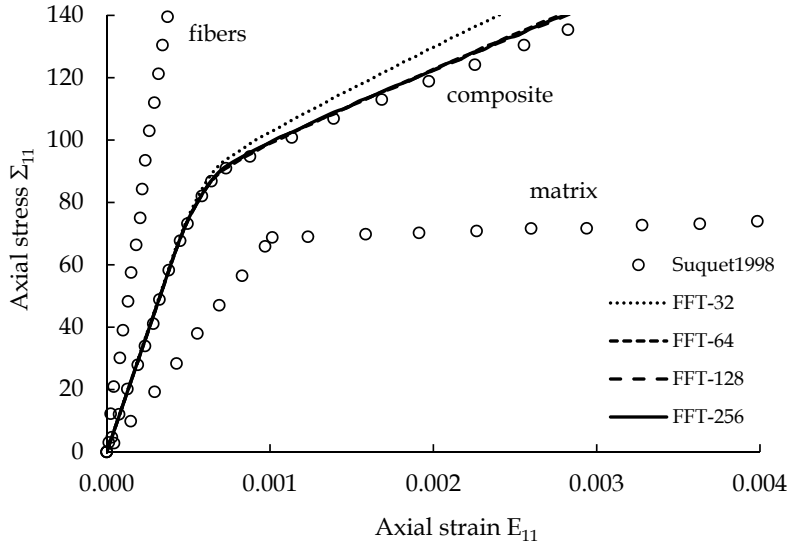

(a)

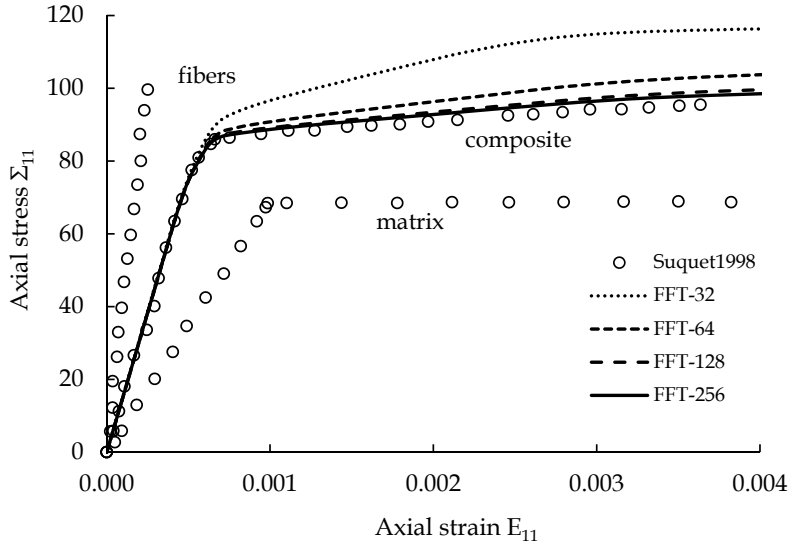

(b)

Fig. 2.4 Comparison of overall behaviors between the results of Suquet (1998) with local response (circled line) and the present method (illustrated in the legend). Axial tension problem with fiber volume fraction $f = 47.5\%$. Different spatial resolution are performed: (a) Matrix with isotropic linear hardening; (b) Perfectly plastic matrix

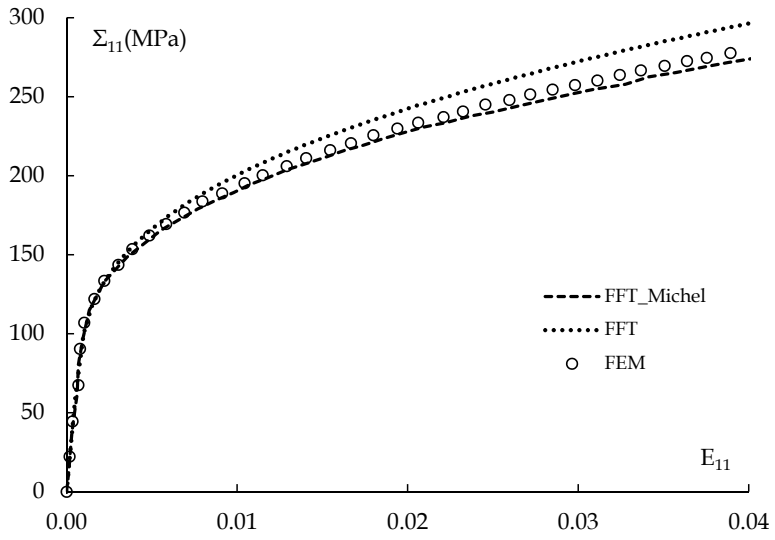

Fig. 2.5 Von Mises matrix with isotropic hardening under uniaxial tension, FFT (dot line), FFT Michel(2004) (dashed line) and FEM (circled line).

2.2.2 Comparison with isotropization method

Hill's incremental method has been widely used to predict the overall response of the matrix-inclusion type composite materials. Abou-Chakra Guéry et al. (2008) and Jiang and Shao (2009) found that the incremental method predicted the effective properties too stiff and an isotropization technique was introduced by using an isotropic approximation of the tangent operator associated to the clay matrix for J_2 plasticity theory (Doghri and Ouaar, 2003; Pierard and Doghri, 2006). The results with the isotropization procedure provided a good agreement with the FE reference solution, however, the technique is lack of physical interpretation. As a full field micromechanical analyzed method, the FFT based method computes the macroscopic response of composite materials strictly from microscopic scale by considering the shapes and proportions of inclusions as well as their distributions. The predictions from the incremental method coupled with the isotropization procedure are recalled here from the work of (Jiang and Shao, 2009). The FE reference solution is calculated with the FEM software Abaqus with UMAT procedure and the FFT based approach provided the results with the same geometry and materials parameters.

The micromechanical model is simply proposed as a two-phase composite with linearly elastic inclusions characterized by Young's modulus and Poisson ratio:

$$E_I = 98GPa, \qquad \nu = 0.15. \tag{2.50}$$

An modified non-associated Drucker-Prager type elastoplastic behavior is assumed for the matrix phase, and the elastic paramters are:

$$E_m = 3GPa, \qquad \nu = 0.3, \tag{2.51}$$

and the plastic yield criterion is defined by:

$$f = \alpha\sigma_m + \sigma_{eq} - (\sigma_0 + H\gamma^m) = 0, \tag{2.52}$$

with the plastic flow rule:

$$g = \psi\sigma_m + \sigma_{eq} - (\sigma_0 + H\gamma^m), \tag{2.53}$$

where $\sigma_m = tr(\boldsymbol{\sigma})$ and $\sigma_{eq} = \sqrt{\frac{3}{2}\boldsymbol{S} : \boldsymbol{S}}$ are the mean stress and equivalent stress, respectively, $\boldsymbol{S}$ being the deviator stress. The plastic parameter α and ψ are the material constant with the initial threshold of yield stress σ_0. H and m are the hardening parameters with the plastic variable γ computed by the accumulation of the equivalent plastic strain rate $\dot{\gamma} = \sqrt{\frac{2}{3}\dot{\boldsymbol{\varepsilon}}^p : \dot{\boldsymbol{\varepsilon}}^p}$. And the values of the plastic parameters used in the simulations are listed in Tab. 2.3:

Table 2.3 Plastic parameters of the clay matrix

α	$\sigma_0(MPa)$	$H(MPa)$	m
0.167	8.0	190.0	0.30

Two different volume fractions are considered: $f = 5\%$ and $f = 15\%$, with different plastic parameter ψ so-called the volumetric dilatance coefficient: $\psi = 0.167$ is for the associated case, and $\psi = 0.10$, $\psi = 0.15$ and $\psi = 0.20$ for the non associated cases. The results obtained from the FFT method are compared with the original incremental method, the isotropization method and the FE reference method in Fig.2.6 and Fig.2.7 for $f = 5\%$ and 15%. It is noted that the isotropization method has a obviously better prediction with the anisotropic technique. However, it is observed that the isotropization approach is influenced by the volumetric dilatancy coefficient ψ. The direct simulation of the FFT method provides more accurate predictions for different conditions. It is worthy mentioning that the FFT approach is strictly obtained from the microscopic level and the microstructures are more

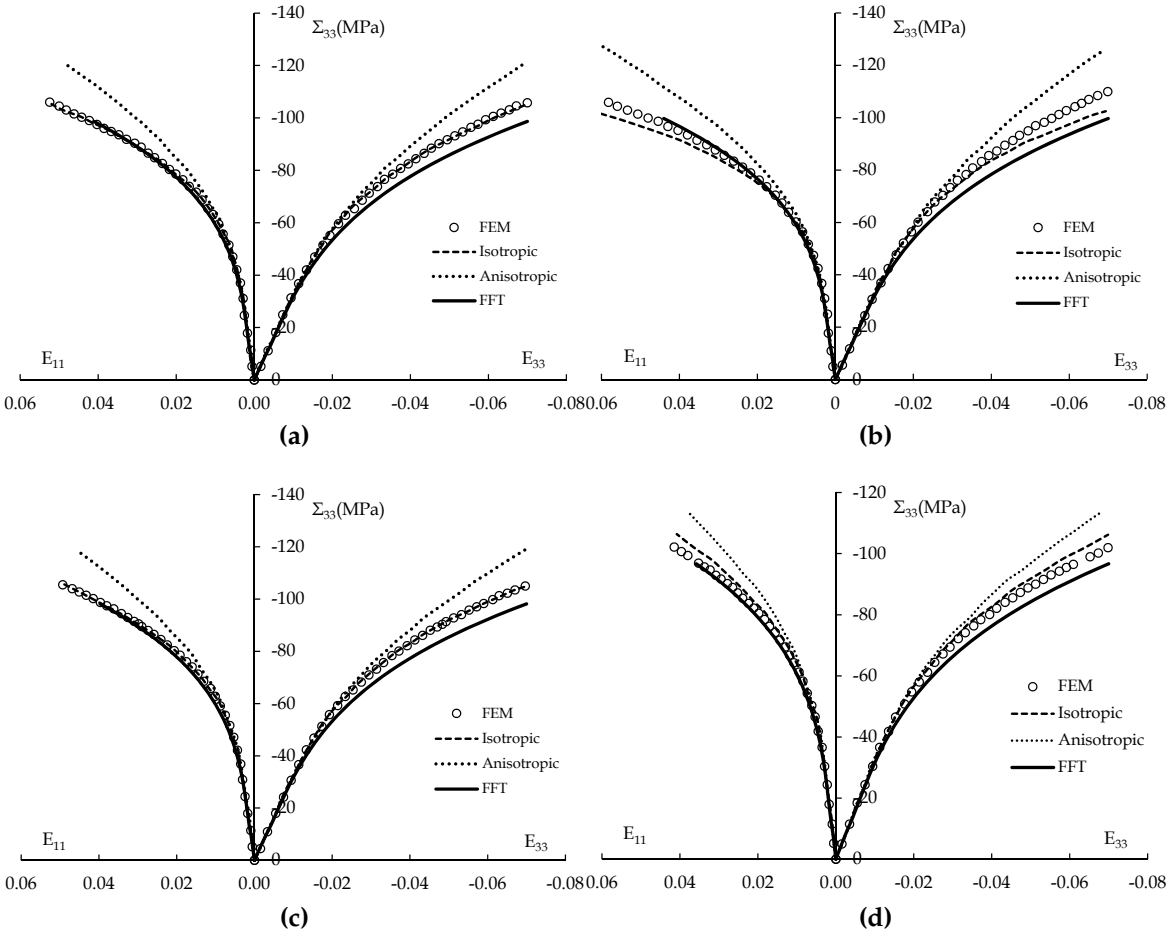

Fig. 2.6 Comparison of the overall response for inclusion reinforced composite under uniaxial compression test between FFT method, Hill's incremental approach, isotropization method and FE solution. Volume fraction: $f = 5\%$, plastic dilatancy coefficient: (a) $\psi = 0.167$ (associated); (b) $\psi = 0.20$; (c) $\psi = 0.15$; (d) $\psi = 0.10$.

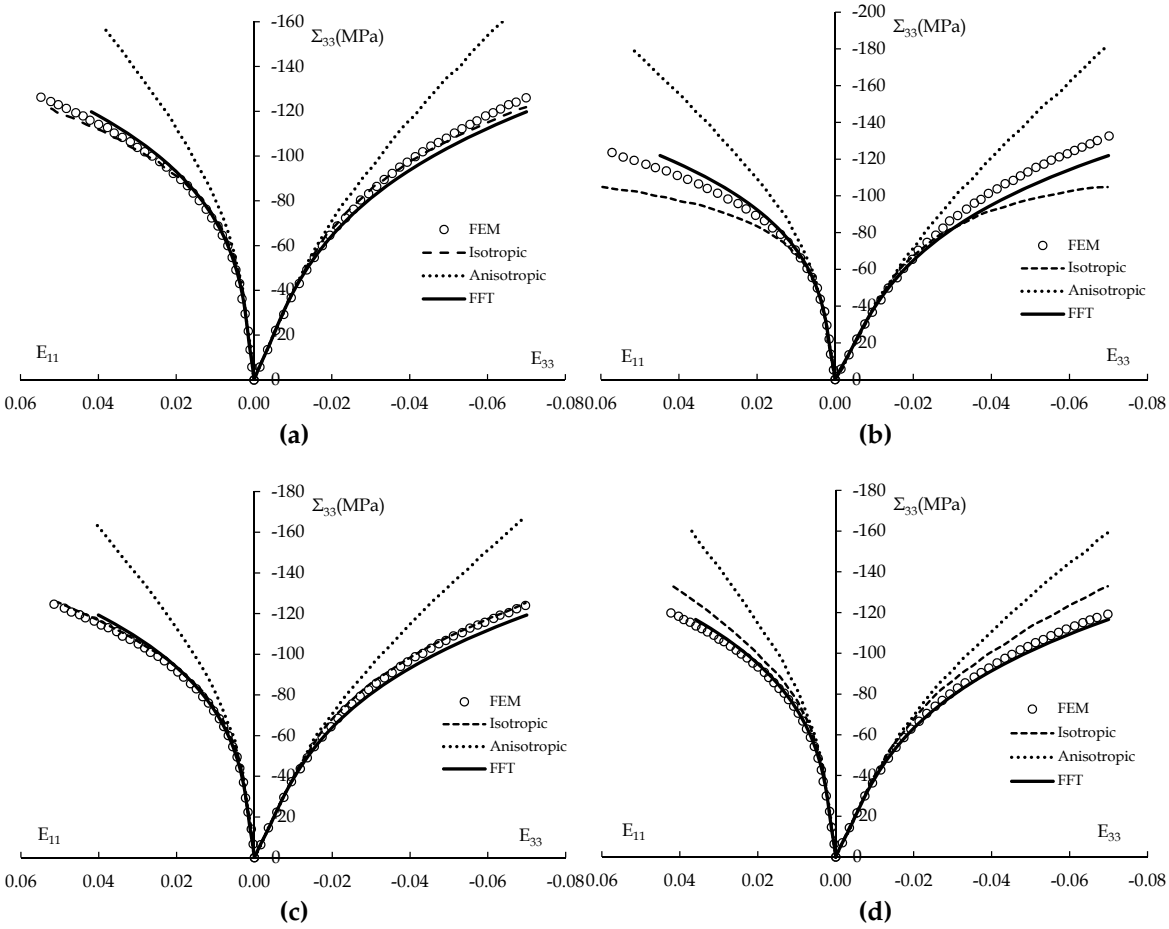

Fig. 2.7 Comparison of the overall response for inclusion reinforced composite under uniaxial compression test between FFT method, Hill's incremental approach, isotropization method and FE solution. Volume fraction: $f = 15\%$, plastic dilatancy coefficient: (a) $\psi = 0.167$ (associated); (b) $\psi = 0.20$; (c) $\psi = 0.15$; (d) $\psi = 0.10$.

eligible for physical characterization.

2.2.3 Application to porous materials

As stated previous the present scheme is strain based algorithm which was verified in Monchiet and Bonnet (2012) that such iterative scheme has a nice convergence for the case of voided materials. Indeed, the tests with the present strain based formulations show a satisfactory convergence for porous material (see Fig.2.2). Therefore, an elastoplastic porous material is studied by the present method and the results are compared with the classical computational method, for instance, the Finite Element Method (FEM), the nonuniform transformation field analysis (NTFA) and Gurson's model. The reference solutions are obtained from Jiang et al. (2011) for the case of uniaxial tension test with porosity of $f = 10\%$ and $f = 25\%$, respectively. The results of the FFT method is calculated with the present numerical simulations and the comparison are illustrated in Fig. 2.8. It is noted that comparing with NTFA and Gurson's model the present FFT method has a much better agreement with the reference solution of FEM for both porosities.

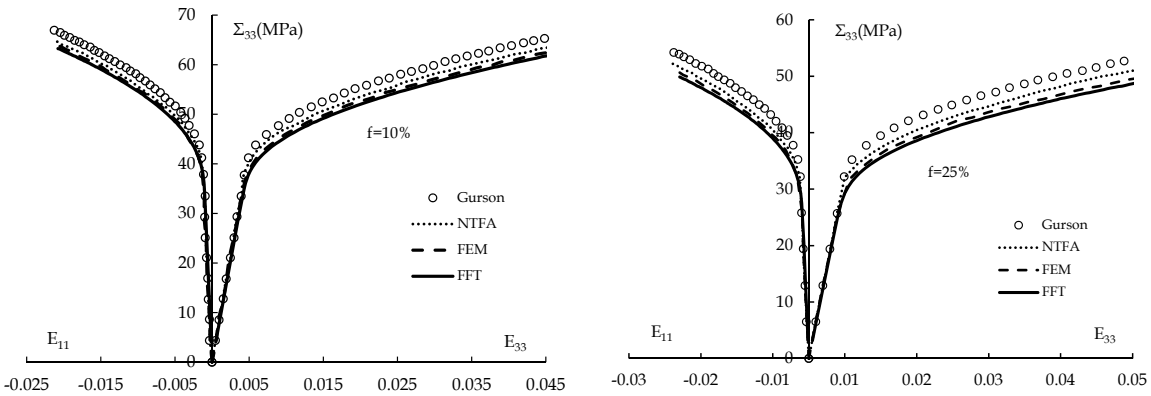

Fig. 2.8 Comparison of numerical methods for porous materials under uniaxial tension test: (a) $f = 10\%$, (b) $f = 25\%$: Gurson's model (circled line), NTFA (dot line), FEM (dash line) and FFT (solid line).

2.3 Closing remarks

This chapter is aimed to review the FFT based method from the respects of mathematical fundamentals and numerical implementations. It is also intend to verify the FFT based method for the composite materials, for instance, two-phase composite consists of elastoplastic matrix and perfectly linear elastic inclusions under uniaxial tension and compression tests. The results are firstly compared with the reference resolution obtained by the FEM software ABAQUS. Afterwards, some typical tests in the contributions of the researchers such as Moulinec and Suquet (1998), Michel and Suquet (2004) are analyzed and compared and the results are satisfactory. The comparison with isotropization approach confirms that the FFT method to be an eligible full field simulation tool for the predictions of the nonlinear heterogeneous composite materials. Moreover, the present approach shows its advantages for the highly contrast case, especially materials with voids. The results for the porous materials are modeled and compared with the classical schemes, for example, FEM, the Gurson's model and the NTFA. The results obtained by the present method are well agreed with the reference methods, and in some cases the present method even provides a better resolution. Furthermore, some influence factors are studied as well, for instance, the spatial resolutions which strongly affect the accuracy of the method. Nevertheless, the present method also indicates some shortcomings, *e.g.*, the convergence rate is very slow for some cases such as hard inclusions, even not possible for rigid inclusions.

After all these analysis the present method can be noted as a valid computational method to proceed further research. On one hand, the present method can be improved from the algorithm for the iterative rate and some critical situations such as rigid inclusions. On the other hand, the present method has been validated for several cases which can lead to the research for the study of interfaces, three phases consist of matrix, inclusions and porous at the same time, and damage process caused by cracks and so forth.

Chapter 3

Effects of microstructure on macroscopic behaviors of nonlinear matrix-inclusion type composites

The macroscopic properties of matrix-inclusion type materials strongly depend on the microstructures, for example, the shape, size, arrangement and proportion of the individual phases. The FFT method provides a powerful tool to determine the effective properties taking into account the effects of the complex microstructures. The treatment of microstructures of composite materials by the FFT method has huge advantages for numerical simulations since the aim of the development of the approach is to make directly use of the image of real structures (Moulinec and Suquet, 1994, 1998). FFT method discretizes the structure into points (pixels) and assigns the mechanical properties according to the local position of points individually. In this case, the local information of the microstructures (phase compositions and proportions, *etc.*) is completely known at microscopic scale. The macroscopic responses can be fully computed by the average theorem. More importantly, the scheme can be pragmatically extended into three dimensional problem without any fundamental difficulties.

This chapter aims to present the numerical treatment of microstructures by the FFT method and to study the effects of microstructure on the macroscopic response of the nonlinear matrix-incluson type composites. Different microstructures will be studied, for example, matrix reinforced by one centered spherical/ellipsoidal inclusion, or randomly distributed inclusions, to show the inclusion shape, size and orentations effects.

3.1 Numerical generation of microstructure

The microstructure of a real structure is usually too complicated to treat in simulation, especially for the method requiring to mesh the structure. As stated in previous chapter, the FFT method is developed to overcome such intractable problems by making use of the image of the real structure by discretizing the structure into points (pixels for 2D images and voxels for 3D ones). Each point carries the local information such as mechanical properties, thermodynamic parameters and so forth. The images of a real structure can be simply obtained from a micro-CT scanner. The digital information of the real structure can be acquired straightforwardly by image processing and the data can be then directly utilized into the numerical simulations and to predict the effective properties of heterogeneous materials. The procedure of such application and the numerical formulations are referred to the work of (Lebensohn et al., 2011). However, an alternative way is used in this research to produce the microstructure artificially.

3.1.1 Procedures of generation

The numerical treatement is presented with a microstructure of a matrix reinforced by one centered spherical inclusion. For the sake of simplicity, a two dimensional example is firstly considered to explain the procedure. Suppose that the structure is a unit square consisting a circular inclusion in the center (see Fig.3.1a). The numerical treatment of producing the microstructure artificially is presented in the following:

1. Disretize the corresponding unit cell into, for instance, 8×8 points with regular grid as shown in Fig.3.1b.

2. Digitalize the structure on the discretized points with numerical values. As is shown that the pixels located totally inside of the circle are assigned to be 1 and the rest to be 0 (including the ones crossed by the circle).

3. Represent the microstructure numerically according to the material properties given in Fig.3.1a. Assign the digital value (see in Fig.3.1b) to characterize material phases, for example, 1 for material 1 (black) and 0 for material 2 (white). Putting the digital data into the numerical program to generate the microstructure illustrated in Fig.3.1c. All the data needed *i.e.* mechanical

properties, distribution and proportion of phases, are known and ready to use in the computational program as the discreted algorithm stated in chapter 2.

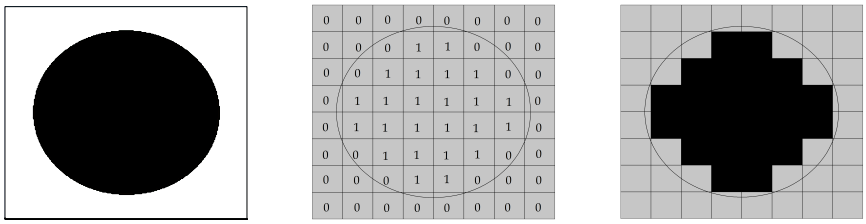

(a) Original image **(b)** Regular grid 8×8 **(c)** Numerical representation with 8×8

Fig. 3.1 Numerical treatment of image. (a) Original image from Micro-CT scanner; (b) Discretization with 1 for the pixels totally inside of the circle and 0 for the rest; (c) Treatment in numerical calculations: the pixels with value 1 assigned to be black phase and 0 for white phase with certain mechanical properties.

It is noted that comparing the inclusion generated by numerical simulation in Fig.3.1c with the original one in Fig.3.1am a great difference can be found, particularly the interface between the matrix and inclusion. Nevertheless, it can be improved by increasing the number of the discrete points as shown in Fig. 3.2. It is noted that 64×64 is sufficient enough to represent the original structure. With the increase of spatial resolution ($N_1\times N_2$) the loss of details on the material interfaces is reduced dramatically, and the microstructure generated is sufficiently precise. The effects of the spatial resolution on the numerical results of macroscopic level will be discussed in detail in the following section.

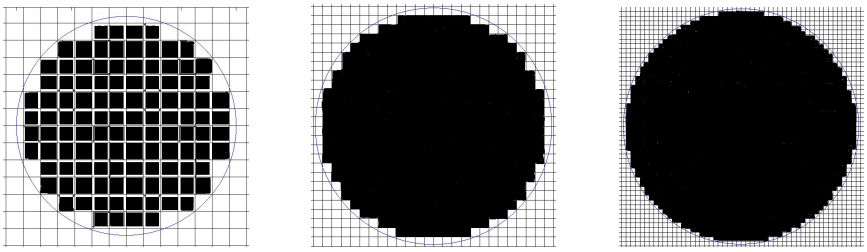

(a) 16×16 **(b)** 32×32 **(c)** 64×64

Fig. 3.2 Numerical representation for 2D problem: reduction of information loss by increasing discrete points.

Based on the 2D example, the microstructure generation of the FFT method can be then extended into three dimensional and some more complex cases. Basically,

the numbers, the shapes, the proportions and the distributions of the inclusion determine the microstructures. On the one hand, the shape of the inclusion is able to be various. For example, sphere, ellipsoid, cube or layer, even for some very complex shapes. On the other hand, the distributions of the inclusions with different shapes can be considered for a complex microstructure. For instance, multiple inclusions with regular or random distributions, isotropic or anisotropic structures with the shape of ellipsoidal inclusions. Basically, the numbers, the shapes, the proportions and the distributions of the inclusion determine the microstructures and the microstructures coupled with their mechanical properties effect the macroscopic behaviors of the composite materials. Therefore, the microstructure generation of the FFT full field simulation provide a powerful tool to study the effective properties of the composite from the analysis of the microscopic scale.

The basic procedures of the microstructure generation for the FFT full field simulation are summarized in the following:

1. Discretize the unit cell into regular grid with $N_1 \times N_2$ pixels for two dimensional simulation and $N_1 \times N_2 \times N_3$ voxels for three dimensional simulation and assign each of the node a specific coordinate (N_1, N_2, N_3). The entire unit cell consist of $N_1 \times N_2 \times N_3$ nodes and the coordinates of all the nodes have to fall between $(0,0,0)$ to $(1,1,1)$. All the node information is uniform as matrix at this moment and to be ready to use in the algorithm stated in the chapter 2 of the discretization procedure.

2. Find the location and shape parameters of the inclusion. For example, the structure of a sphere in the center of a cube. The center of sphere shall be $(0.5, 0.5, 0.5)$. As the volume fraction f is known, the radius of the sphere can be calculated by $R = \sqrt[3]{f/(\frac{4}{3}\pi)}$. The procedure is exactly the same for other shapes, for instance, the volume fraction of an ellipsoidal inclusion is calculated with $V = \frac{4}{3}\pi abc$. The only difference is the determination of the axis radius with different aspect ratio Ar and consequently produces prolate or oblate inclusions.

3. Generate the microstructure with specific mathematical equations according to the initial structure. Take a sphere as an example, the equation of a sphere in real coordinate space ($\mathbb{R}^3$) is $(x-x_0)^2 + (y-y_0)^2 + (z-z_0)^2 = R^2$. (x, y, z) is the coordinate of the nodes and (x_0, y_0, z_0) is the center of the sphere with radius R. With this equation the domain of the inclusion can be determined. All

the nodes inside of the equation will be assigned the inclusion information. With their specific coordinates and material properties all nodes information are stored in an array, and now are ready to use in the discrete algorithm proposed in the previous chapter.

The steps above provide the way of generating artificial microstructures of single inclusion without any fundamental difficulties. Some very complex microstructures are frequently appeared in the field of composite media. For example, numbers of spherical inclusions randomly distributed inside the cubic matrix. To reproduce such microstructure, it requires an iterative algorithm to generating the location of the spheres. As the first sphere is found simply without any constrain, the rest of the spheres has to satisfy some requirements, for instance, the interaction between spheres, the radius and the orientation for the case of ellipsoid. No interaction is allowed and the sphere is uniform. The distance between the center of the first and the second sphere must greater than two times of their radius. Similarly, the third one must has no interaction with the former two and the same for the rest ones.

For the case of ellipsoidal inclusion the algorithm is much more complicated due to their orientation. The approach is to generate the spheres first and then change the aspect ratio Ar and the orientation is rotated by a random angle θ with respect to the axis. The definition of the original position and its rotation angle θ of a prolate and oblate ellipsoid are illustrated in Fig. 3.3, respectively. According to the general rotation equation with respect to any axis. For example, the original coordinate (x,y,z) is rotated with respect to y axis in space as a new coordinate (X,Y,Z) by a rotation matrix:

$$\begin{bmatrix} X \\ Y \\ Z \end{bmatrix} = \begin{bmatrix} cos\,\theta & 0 & sin\,\theta \\ 0 & 1 & 0 \\ -sin\,\theta & 0 & cos\,\theta \end{bmatrix} \cdot \begin{bmatrix} x \\ y \\ z \end{bmatrix}. \tag{3.1}$$

Therefore, the new equation of an ellipsoid can be expressed as the new coordinates (X,Y,Z) and their original ones $(x-x_0, y-y_0, z-z_0)$ by the former rotation matrix with respect to y axis:

$$\begin{cases} \frac{X^2}{R_A^2} + \frac{Y^2}{R_B^2} + \frac{Z^2}{R_C^2} \leqslant 1 \\ X = (x-x_0)\cdot cos\,\theta + (z-z_0)\cdot sin\,\theta \\ Y = (y-y_0) \\ X = (z-z_0)\cdot cos\,\theta - (x-x_0)\cdot sin\,\theta \end{cases}, \tag{3.2}$$

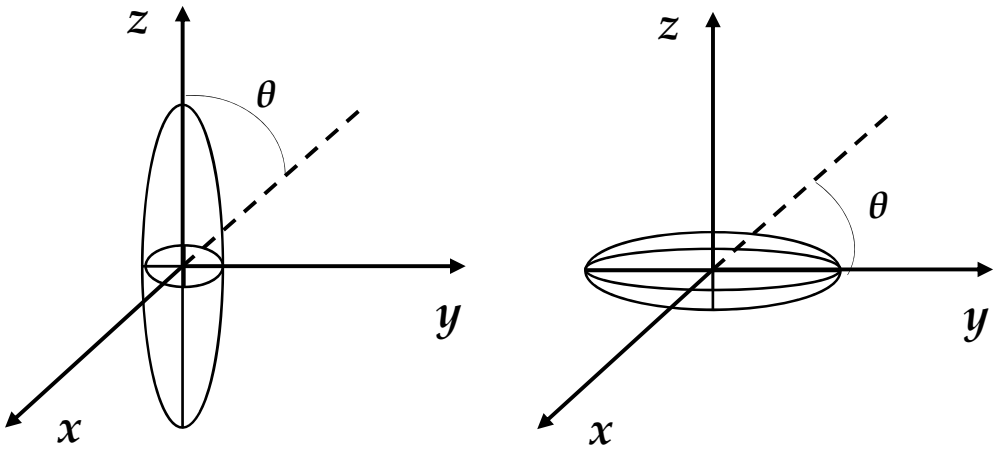

(a) prolate **(b)** oblate

Fig. 3.3 Definition of the geometry of prolate and oblate spheroid, the original position and the transformation angle θ.

where (x, y, z) and (x_0, y_0, z_0) are the coordinates of all nodes and the center of the ellipsoid generated. R_A, R_B, R_C are the semi-principle axes and (X, Y, Z) are the rotated coordinates. It is noted that the rotation angle θ is generated with a random angle for each of the ellipsoid to make the orientations randomly distributed. On the other hand, θ can be also set to be a specific value for uniform distribution to consider the anisotropic microstructures.

The aspect ratio is chosen to be $Ar = 3$ for the prolate inclusion and $Ar = \frac{1}{3}$ for the oblate one if without any specific indication, and $Ar = 1$ for the sphere (no orientation considered). The volume fraction f and the total number N decide the size of inclusions. With the steps above the complex microstructures can be simulated and the effects of microstructures on the overall behavior of matrix-inclusion composite can be studied further.

3.1.2 An example of microstructure and effects of spatial resolution

In order to illustrate the generation of microstructure based on the previous procedure, an example of three dimensional microstructure is firstly shown: a spherical inclusion embedded at the center of a unit cube. The numerical treatment follows the former procedure to discretize the cube into voxels and the spherical inclusion is characterized by the specific voxels with different material properties from the matrix phase as illustrated in Fig. 3.4. The figure shows the basic microstructure which is not distinct since the spatial resolution is not high enough ($32 \times 32 \times 32$ in

this case). In order to realize the influence of the spatial resolution, a comparison is performed in Fig. 3.5. It shows clearly that the higher spatial resolution provides a more accurate microstructure. The spatial resolution affects not only the realization of microstructures but also the accuracy of the numerical calculations. These effects will be discussed in the following section in details.

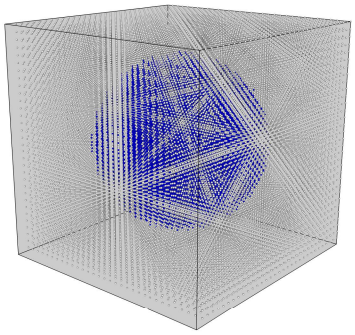

Fig. 3.4 Microstructures of 3D representation of a cube centered with a spherical inclusion ($32\times32\times32$ spatial resolution).

It is noted from the Fig.3.5 that the realization of the figure is based on displaying all voxels point by point with grey points for matrix phase and blue points for the inclusion phase. In other words, the composite material is composed with full local information carrying their own material properties. It is the way of microstructure generation and numerical calculation. It is much more convenient to set the matrix phase to be transparent in order to exhibit clearly the insider microstructures. Nevertheless, the analysis of strain and stress field under mechanical loadings at microscopic scale requires the full field exhibition.

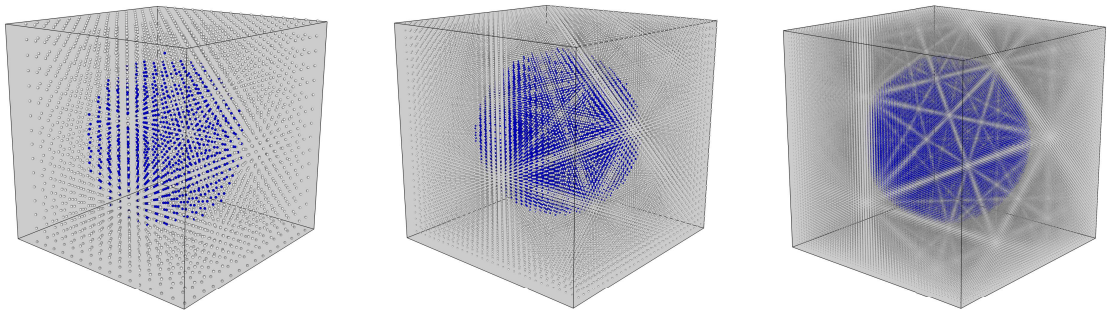

(a) $16\times16\times16$ **(b)** $32\times32\times32$ **(c)** $64\times64\times64$

Fig. 3.5 Numerical representation for 3D problem: reduction of information loss by increasing discrete points (spatial resolution).

It is worthy mentioning that the FFT simulation features the possibility of mod-

eling solid inclusions but also void media. The only difference is the step of assignment of the material properties on the discretized points. Therefore, these microstructures are used in the following of this chapters for solid inclusions and are extended to porous materials in the later chapters. Additionally, the procedure of the microstructure generation also allows to extend the simulation into multiphases without fundamental difficulties.

3.2 Effects of microstructure with different types of inclusions

As stated in the summary of the microstructure generation, the original intention for modeling microstructures without meshing potentializes this method to be more efficient to build various types of microstructures for matrix-inclusion type composites. The divese shape coupled with different arrangements can produce extensive numbers of microstructure. For example, one inclusion case with spherical or ellipsoidal shape, multiple inclusions with regular or random distributions, the isotropic and anisotropic structure due to the orientation of ellipsoidal inclusions *etc.*. In this section, the objective is to study further the effects of the microstructures generated on the macroscopic behavior of composite materials by the FFT simulation. The effects of inclusion shapes, distributions, sizes, orientations with the loading path will be considered. The examination of these effects is an important issue in the field of micromechanics, which can provide a effective approach to study the macroscopic behaviors of composite materials at the microscopic level.

3.2.1 One spherical inclusion

A two dimensional example has been compared in chapter 2 with the results of (Moulinec and Suquet, 1998) and as stated previously that the FFT based method can be simply extended into three-dimensional problems. A 3D numerical study is performed in this section to exhibit the efficiency and accuracy of the FFT method with some typical homogenization approaches and the reference FE solution (referred to Kanouté et al. (2009); Michel and Suquet (2004)).

The studied material is assumed to be a periodic matrix-inclusion composite (see Fig. 3.6) with the inclusion volume fraction $f = 30\%$. The interface between the two phases is assumed to be perfect bonded. The material parameters are recalled

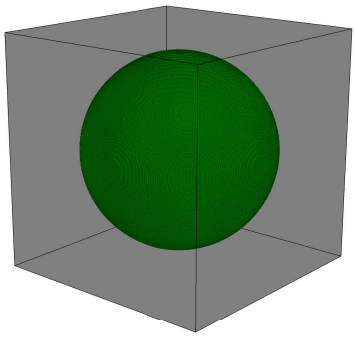

Fig. 3.6 Microstructures of 3D representation of a cube centered with a spherical inclusion ($256 \times 256 \times 256$ spatial resolution).

from (Michel and Suquet, 2004). The inclusion is assumed to be perfect elastic with the elastic parameters:

$$E_f = 400GPa, \quad \nu_f = 0.2.$$

The local behavior of matrix is characterized by a Von Mises criterion with an isotropic power law hardening:

$$\sigma_{eq} \leqslant \sigma_0 + H\gamma^m,$$

with the following material parameters:

$$E_m = 75GPa, \nu_m = 0.3, \sigma_0 = 75MPa, H = 416MPa, m = 0.3895,$$

and the accumulated plastic strain γ defined by the rate of equivalent plastic strain:

$$\dot{\gamma} = \sqrt{\frac{2}{3}\dot{\varepsilon}_p : \dot{\varepsilon}_p},$$

in which $\dot{\varepsilon}^p$ is the plastic rate.

As the material parameters are defined for each material components, the composite material is studied with a prescribed tension. The Fig. 3.7 shows the comparison between FFT method and the typical homogenization methods for the prediction of the overall strength of the composite. It is noted that the Transformation Field Analysis(TFA) and Hill's incremental approach predict very stiff responses. With some improvements on both methods the Nonuniform Transformation Field Analysis (NTFA) and isotropic incremental approach provide a very comparable prediction compared with the FEM reference solution. It can be seen that the FFT

method has a very good agreement with those modified approaches and the FE reference solution without any numerical difficulty and modification. It is worthy noting that the NTFA and Hill's incremental with isotropization are both mathematical modifications and are intractable to explain the physical meaning. Meanwhile, it is difficult for the mean field approaches to provide the analysis of the local field description due to the means of the simulation of microstructures. However, as the full field approach the FFT method has the merit of full analysis of the whole field and of the physical explanations at the microscopic level as shown in Fig. 3.8.

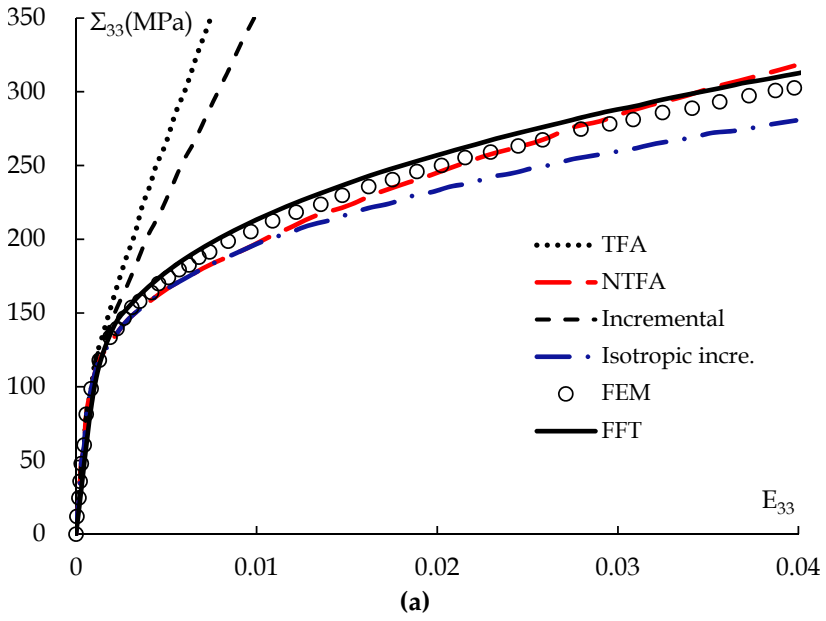

Fig. 3.7 Overall response of unit cell for isotropic power law hardening matrix composite in 3D: (a) geometry generated by FFT method; (b) comparison between the FFT method (solid line) and the reference FE solution (circled line) with different homogenization methods.

The FFT method is able to provide the distributions of the local stress and strain at every loading step and the local fields can be known at each material point. The Fig. 3.8a illustrates the field analysis of local stress (σ_{33} in loading path) distributions in three dimensional with half of the unit cell. A sectional face is chosen to display the stress distributions in 2D in order to observe more clearly the details (see Fig. 3.8b). The Fig. 3.8c and 3.8d show the distributions of local stress at the chosen sectional face at the primary stage and the last stage, respectively. The value at each point is displayed in details on the whole field. It can be seen that the stress concentration is explicit at the interface region. The positive stress is clearly observed on the loading path and negative one is found on the perpendicular direction of the vertex of the

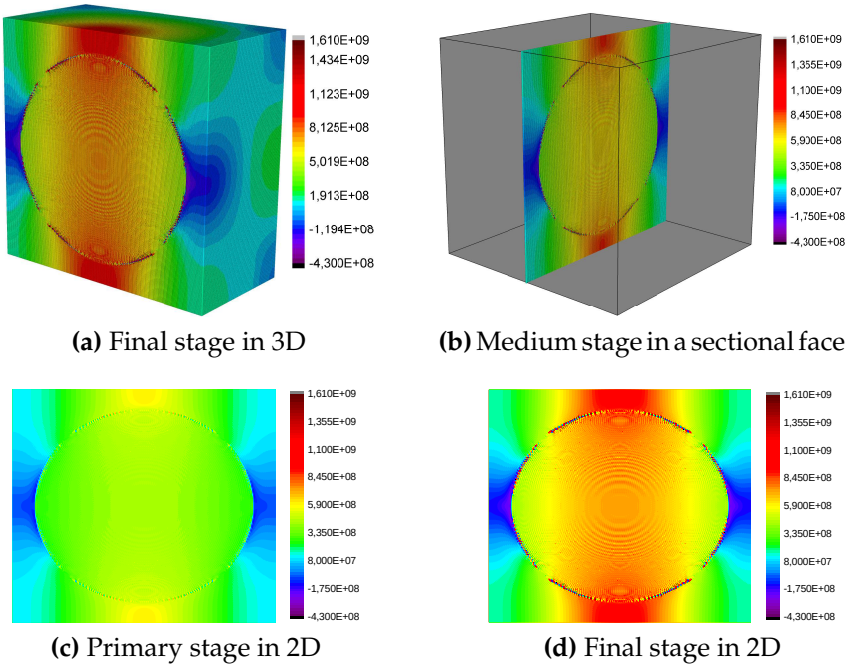

(a) Final stage in 3D **(b)** Medium stage in a sectional face

(c) Primary stage in 2D **(d)** Final stage in 2D

Fig. 3.8 Distribution of local stress predicted by the present method: (a) primary stage; (b) final stage; (c) distribution in 3D.

inclusion.

3.2.2 One ellipsoidal inclusion

As is known that the shape of inclusion strongly effects the effective properties of composite materials. Apart from the spherical inclusion, the FFT method is able to investigate the case of matrix with ellipsoidal inclusions. With respect to the aspect ratio A_r, the ellipsoid is classified into four distinct cases. Excepting the special case ($Ar = 1$) for the sphere and scalene spheroid, two typical shapes are studied: prolate and oblate spheroid. Different from the sphere, the orientation of ellipsoid effects the microstructures and the overall behaviors of the composite materials. Fig. 3.9 illustrates the typical samples concerning the angle θ between the orientation of major axis of ellipsoid.

The microstructure generation of ellipsoid is different from that of sphere due to its orientations. The volume fraction of the ellipsoid is $V = \frac{4}{3}abc$ with the semi-principle axes of length a, b, c. For prolate and oblate inclusion simulated in this study, the axes are chosen as $c = Ar \cdot a = Ar \cdot b$ and $a = b = c/Ar$, respectively. Two values of volume fraction are considered: $f = 5\%$ with $Ar = 3$ and $f = 30\%$ with

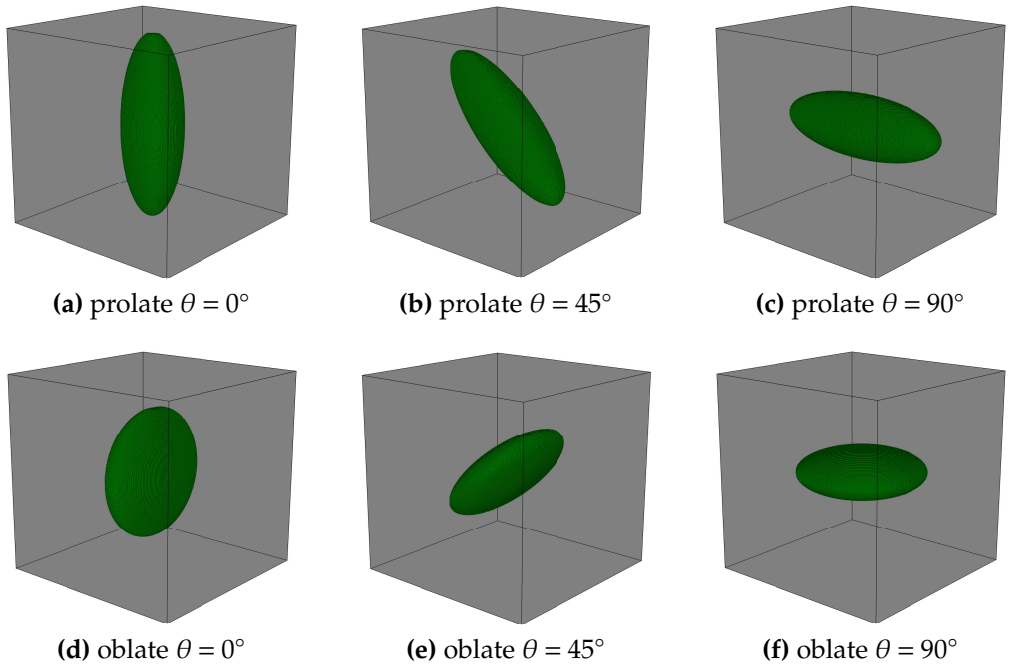

(a) prolate $\theta = 0°$ **(b)** prolate $\theta = 45°$ **(c)** prolate $\theta = 90°$

(d) oblate $\theta = 0°$ **(e)** oblate $\theta = 45°$ **(f)** oblate $\theta = 90°$

Fig. 3.9 Microstructures of different shapes and orientations for single ellipsoid (spatial resolution$256\times256\times256$). θ: angle between the major axes of ellipsoid.

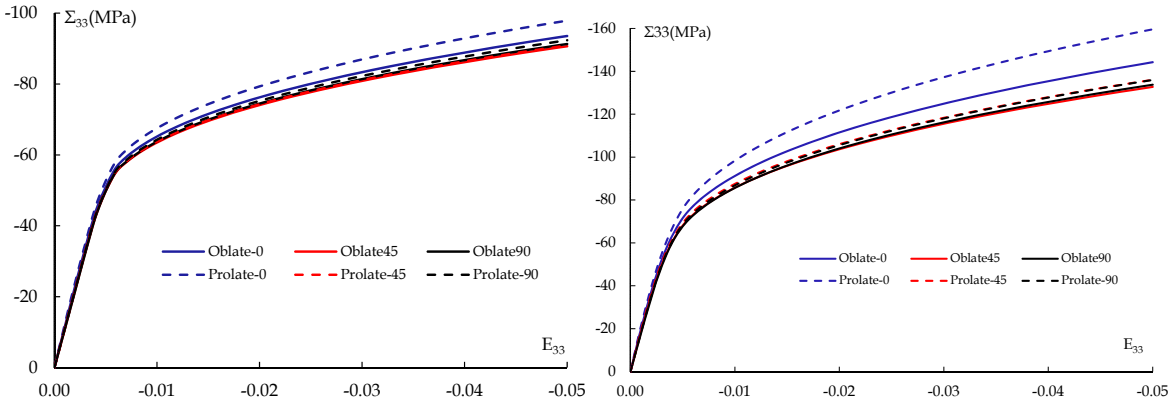

(a) f=5% **(b)** f=30%

Fig. 3.10 Comparison of effective properties for prolate and oblate inclusion with different orientations for two volume fractions.

$Ar = 1.2$. Three values of the angle θ are studied: $\theta = 0°$, $\theta = 45°$ and $\theta = 90°$.

Higher contrast of material properties between matrix and inclusion is considered in this simulation $E_i/E_m = 10$ in order to obtain higher heterogeneous microscopic distributions of strain and stress field. The behavior of matrix is governed with a J_2-type plastic criterion with isotropic hardening $\sigma_{eq} \leqslant \sigma_0 + H\gamma^m$ (defined in previous section), and the inclusion is characterized with perfectly elastic behavior. The values of material parameters are chosen as follows for matrix:

$$E_m = 10GPa, \nu_m = 0.3, \sigma_0 = 45MPa, H = 150MPa, m = 0.4, \tag{3.3}$$

and for inclusion:

$$E_i = 100GPa, \nu_i = 0.2. \tag{3.4}$$

Periodic boundary condition is applied on the unit cell and a macroscopic strain $\boldsymbol{E}$ is gradually prescribed in 3 direction (vertical in the figure) at each time step $\Delta\boldsymbol{E}/\Delta t$:

$$E_{33} = \boldsymbol{E}, \qquad E_{11} = E_{22} = E_{12} = E_{13} = E_{23} = 0. \tag{3.5}$$

The effective properties of composite with different shapes and directions of ellipsoidal inclusion are compared in Fig.3.10 for two volume fractions $f = 5\%$ and $f = 30\%$. It is noted that for low volume fraction ($f = 5\%$) the effects of inclusion shape are not significant and only the prolate inclusion with $\theta = 0°$ is obviously stiffer than others. However, the effects are remarkable for high volume fraction ($f = 30\%$). It is clear that the prolate inclusion is generally stiffer than the oblate one and the angle concerning the loading path $\theta = 0°$ is higher than other angles of orientation. It confirms the influence of the orientation of inclusions.

In order to explicate the macroscopic behavior, the FFT method provides a way for microscopic analysis. The distributions of local stress field σ_{33} are illustrated in Fig. 3.11 and 3.12. Stress concentrations are clearly observed particularly at the region of the material interfaces. For different orientations concerning the loading path, the one with $\theta = 0°$ induces more stress concentration specifically at the vertex of the ellipsoid. For the ones with $\theta = 45°$ and $\theta = 90°$ less stress concentration are observed at the vertex region, but instead of dispersed stress along the loading path. The phenomenon is more distinct for the higher volume fraction for both prolate and oblate shape. From the microscopic view, the stress concentration extensively occurs at the convex part of the geometric shape. It develops maximal concentration as the convex part is exactly along the loading path. Meanwhile, as

the convex part has an angle with the loading path, the concentration is reduced and lower concentration appears at nearby region of the geometry. Moreover, plastic deformation and hardening are highly developed at the region with higher stress concentration. Therefore, the prolate with $\theta = 0°$ generating higher macroscopic stress can be fully explained from the microscopic analysis. Indeed, the inclusion shape and orientation have a significant influence on the macroscopic behavior of composite materials.

3.2.3 Randomly distributed spherical inclusions

The microstructures of most matrix-inclusion type composites are very complex. Inclusion with different shapes, sizes, numbers and directions, the microstructure can be found in the matrix. The microstructure can be treated as a matrix reinforced by randomly distributed inclusions. As stated in section of microstructure generaton, the FFT method is able to simulate these complex structures without fundamental difficulties. In this subsection, the case of randomly distributed spherical inclusions will be firstly considered. The microstructure generation is presented in the following. The more complex microstructure with randomly distributed ellipsoidal inclusions will be studied later.

Certain regulations are required to produce the scattered inclusions: 1) Non overlap is allowed; 2) Part of inclusion is permitted to be outside of the unit cell; 3) Size of spheres is uniform. In order to satisfy these rules, an algorithm is proposed to generate the coordinates of inclusion center. Each of coordinates is composed with three random number falling between the range of $(0,0,0)$ and $(1,1,1)$. Iterative scheme is proposed to ensure that the distance between every new generated coordinates and all the former ones is great than $2R$ (R is the radius of the spherical inclusion). The volume fraction f, radius R and number N are related by $f = N\frac{4}{3}\pi R^3$ for sphere and the microstructure is generated with knowing two of these three values.

Two typical microstructures with randomly distributed spherical inclusions are illustrated in Fig. 3.13. The volume fraction is $f = 5\%$ and the radius of the sphere is $R = 0.05$ (dimension of the unit cell $l = 1$). It is shown in Fig.3.13a that a composite reinforced by randomly distributed inclusions with only one property and Fig.3.13b illustrates a composite with two different constituents. The composite with three phases will be discussed in the next chapter. Hereafter, two-phase composite is

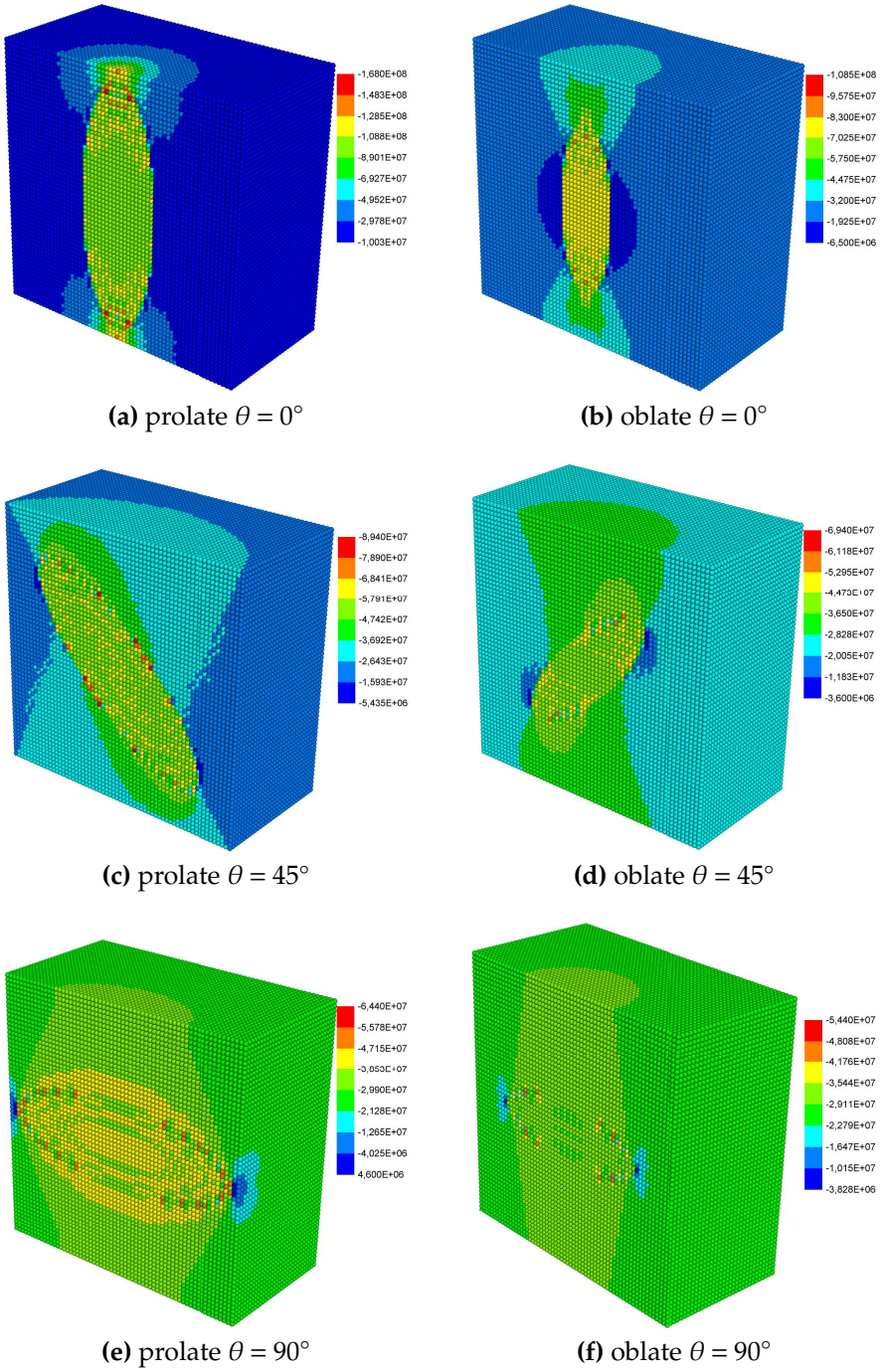

(a) prolate $\theta = 0°$ **(b)** oblate $\theta = 0°$

(c) prolate $\theta = 45°$ **(d)** oblate $\theta = 45°$

(e) prolate $\theta = 90°$ **(f)** oblate $\theta = 90°$

Fig. 3.11 Distribution of local stress σ_{33} (loading path) for prolate and oblate with different orientations θ (angle with loading path), volume fraction $f = 5\%$ with aspect ratio $Ar = 3$.

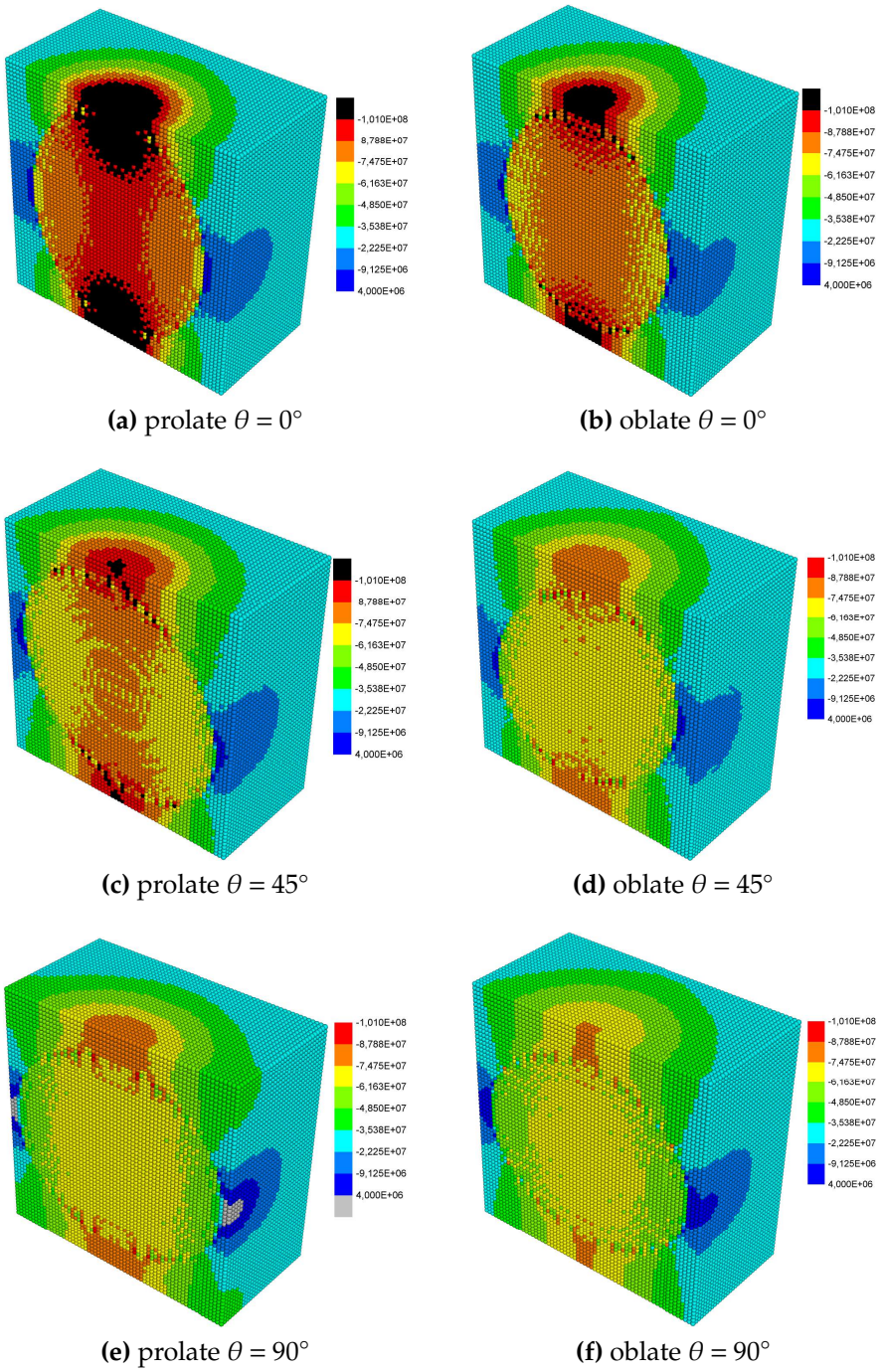

(a) prolate $\theta = 0°$ **(b)** oblate $\theta = 0°$

(c) prolate $\theta = 45°$ **(d)** oblate $\theta = 45°$

(e) prolate $\theta = 90°$ **(f)** oblate $\theta = 90°$

Fig. 3.12 Distribution of local stress σ_{33} for prolate and oblate with different orientations θ (angle with load path), volume fraction $f = 30\%$ with aspect ratio $Ar = 1.2$.

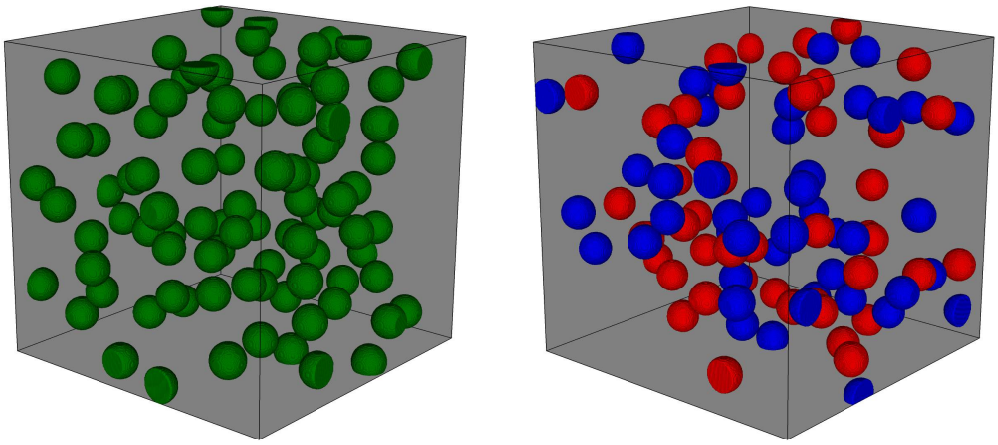

(a) (b)

Fig. 3.13 Microstructures with randomly distributed spherical inclusions for volume fraction $f = 5\%$ and radius of sphere $R = 0.05$ (spatial resolution $256 \times 256 \times 256$). (a) two-phase composite; (b) three-phase composite.

examined.

As the properties of inclusions are uniform, the size effects of the inclusions are practical problems concerning in the filed of composite materials from the view of microscopic level. It is an elemental feature for the FFT method and microstructures with different sizes are illustrated in Fig. 3.14. The volume fraction is the same for microstructures with different size of inclusions as $f = 20\%$. The size of the inclusions is simulated for $R = 0.01$, 0.02, 0.05, 0.01 and 0.2, here only three typical sizes are illustrated. The figures show the distributions of microstructures from microscopic level.It can be observed that the composite with smaller size of inclusions (see Fig.3.14c) scatters inside of the whole unit cell. The structure tends to be uniform and isotropic compared with those with larger size of inclusions (see Fig.3.14a).

In order to validate the analysis and prediction of overall responses, uniaxial tension tests (following the direction 33) are studied on the microstructures with different size of inclusions and the results are shown in Fig. 3.15. The figure shows that the inclusion size has a great influence on the macroscopic behavior. The effective strength is stiffer for the composites with smaller size of inclusions. The FFT method provides a better way to analyze the microscopic variables with the full field simulation. Fig. 3.16 shows the distributions of the local stress σ_{33} for the composites having different size of inclusions with the same volume fraction $f = 20\%$ under uniaxial tension tests. The figures demonstrate the distributions of stress fields at the final stage of the loading process. It can be seen that the stress in

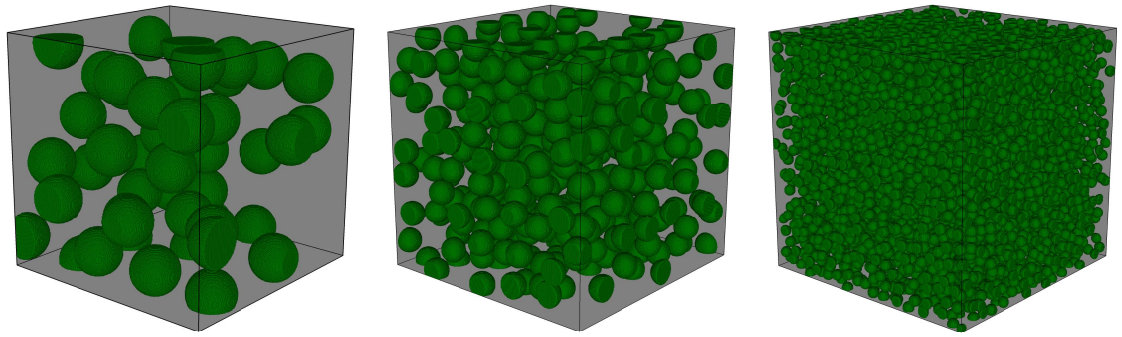

(a) R=0.1 **(b)** R=0.05 **(c)** R=0.02

Fig. 3.14 Microstructures for different size of inclusions for the same volume fraction $f = 20\%$. (a) R=0.1; (b) R=0.05; (c) R=0.02.

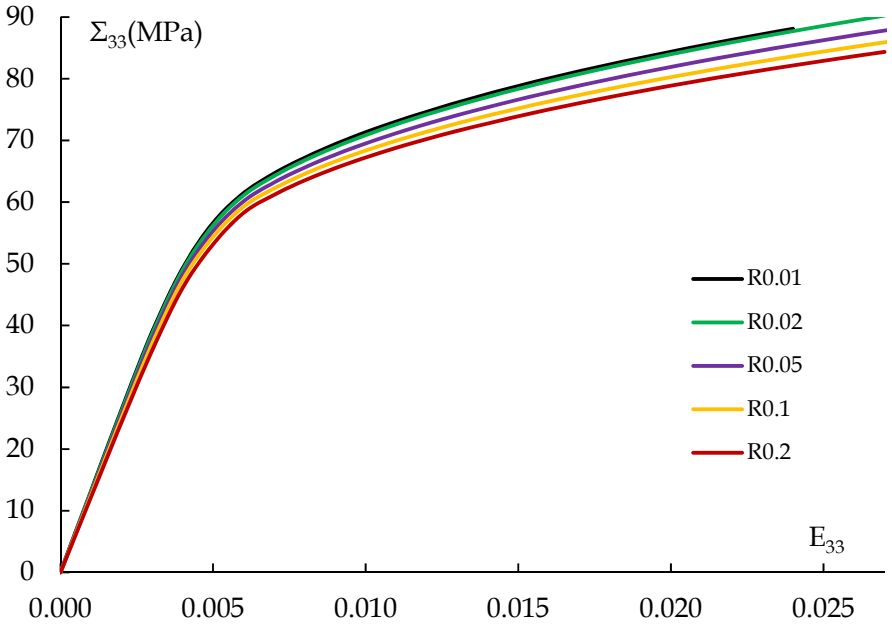

Fig. 3.15 Effective strength predicted by the FFT simulation for different size of inclusions with the same volume fraction.

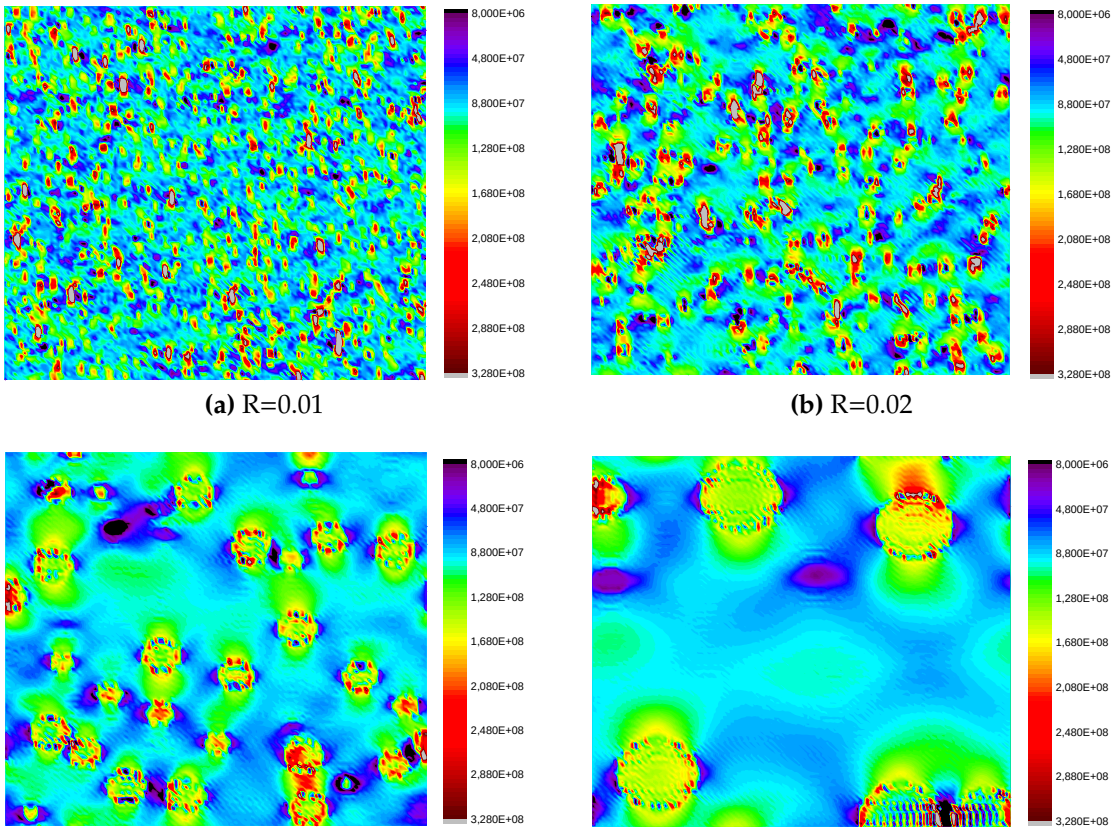

(a) R=0.01 **(b)** R=0.02

(c) R=0.05 **(d)** R=0.1

Fig. 3.16 Distribution of microscopic stress σ_{33} predicted by the FFT simulation for different size of inclusions: (a) R=0.01; (b) R=0.02; (c) R=0.05; (d) R=0.01.

the matrix paste is nearly the same for all sizes and stress concentration takes place largely at the material interfaces and interacted region of the nearby inclusions. It is noted that the stress field nearby the phase boundaries along the loading path are generally higher than other region. Specifically, the figure with small size of inclusions shows large amount of stress concentration and almost dispersed in the whole field. It is shown that the stress is very high at some region with the red color where the value of the stress is up to $200MPa$. In general, the distributions of the local stress field for small size are almost uniform with much more stress concentration. On the contrary, the stress concentration for the microstructures with large size occurs at the region nearby the inclusion, and most of the region remains the lower stress level. Stress concentration between inclusions are also clearly observed along the loading path. For example, the two closed inclusions at the right-down corner in Fig. 3.16c. Contrarily, at the horizontal level the stress is very low comparing with the one in matrix paste (the purple color in the figures). It takes place at the inclusions interaction region as well as the light blue field induced by the inclusions away from this face. In general, from microscopic level it is indicated that the structure with small size inclusion induces more stress concentration compared with the one with large size, and the macroscopic strength is thus higher for the one with smaller size.

3.2.4 Randomly oriented ellipsoidal inclusions

Different from the spherical inclusion, the orientation of ellipsoidal inclusion has to be taken into account to study the effects of microstructure on the macroscopic response. The idea is to generate the sphere first, and it follows the former procedures for generating randomly distributed spherical inclusions. The ellipsoid is then generated inside the sphere with a random orientation. However, the volume fraction is required to be recalculated according to its aspect ratio Ar. The radius of the sphere is R, the maximum length of major axis of prolate is R and the minor axes are R/Ar. The volume fraction of prolate is recalled here: $f = \frac{4}{3}\pi abc = \frac{4}{3}\pi\frac{R}{Ar}\frac{R}{Ar}R = \frac{4}{3}\pi R^3/Ar^2$ for prolate and $f = \frac{4}{3}\pi abc = \frac{4}{3}\pi RR\frac{R}{Ar} = \frac{4}{3}\pi R^3/Ar$ for oblate. It means that the volume fraction f for sphere is able to generate $\frac{f}{Ar^2}$ prolate, similarly, $\frac{f_s}{Ar}$ for oblate. With these procedures the microstructure with randomly oriented ellipsoidal inclusions can be generated and the effects of microstructures on the macroscopic behavior is discussed in the following by using the FFT method.

-Random orientation

Two typical microstructures with randomly distributed inclusions are considered as illustrated in Fig.3.17: random prolate and random oblate inclusions. As is shown in the figure that the scattered inclusions are randomly distributed and this makes the composite homogeneous from the view of macroscopic scale. However, the composite is quite heterogeneous at the microscopic level with different orientation of inclusions. For the purpose of simplicity, the former material properties (see Equations 3.3 and 3.4) are adopted hereafter to simulate the overall behavior of the composites under uniaxial tension test (see Equation 3.5) for two values of volume fraction $f = 10\%$ and 20%. The results will be compared with the one for matrix with randomly distributed spherical inclusions (see Fig.3.13) studied in section 3.2.3.

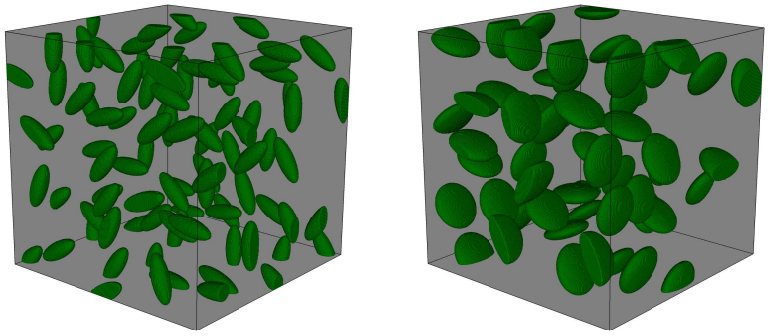

(a) prolate inclusions **(b)** oblate inclusions

Fig. 3.17 Microstructures with 40 randomly distributed inclusions. Volume fraction $f = 5\%$. (a) Prolate inclusion with aspect ratio $Ar = 3$; (b) Oblate inclusion with aspect ratio $Ar = 1/3$. Spatial resolution $400 \times 400 \times 400$.

The effective properties of the composites with three different microstructures are shown in Fig.3.18. It is noted that the microstructures for different shapes have nearly no effects on the overall properties with respect to its volume fraction. For searching the explanation of this phenomenon, microscopic analysis is provided in Fig.3.19. The number of inclusons is large and the inclusions are randomly distributed in the matrix. At the macroscopic scale, the composite is nearly homogeneous despite that the shape of inclusions are different. With the same inclusion volume fraction ($f = 10\%$ and 20%), the macroscopic behaviors are almost the same, but the volume fraction of inclusions significantly effects the material strength. The figures show clearly that the stress concentration near the inclusions. However, for the same volume fraction the amount of the stress concentration is nearly at the same

level. Meanwhile, the stress concentration values compared with the stress field in the dominant matrix phase are almost similar. Consider both the amount and the value for different shapes at the same volume fraction, the effects of the shape are not obviously on the macroscopic level. Therefore, the effects different shapes of randomly distributed inclusions are very limited comparing with the dominant matrix region. It is the reason that the stress-strain relation exhibits the almost same response for different shapes at the macroscopic level.

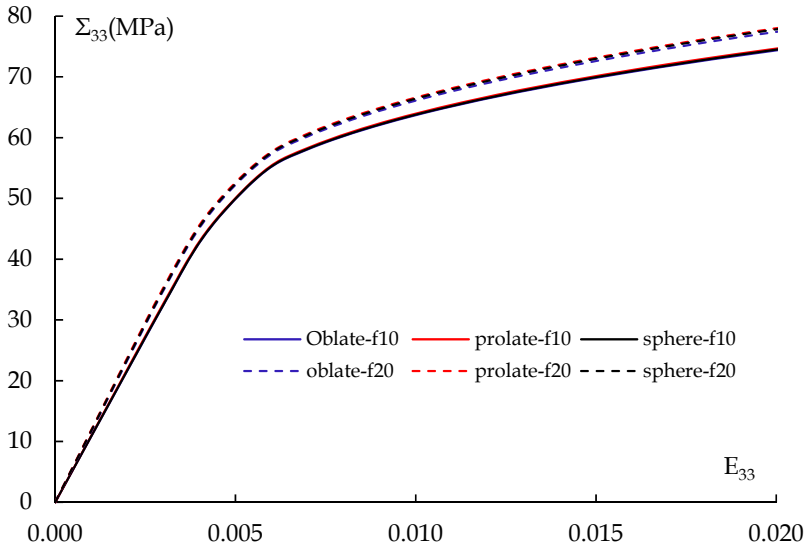

Fig. 3.18 Effects of randomly distributed inclusions with the shape of sphere, prolate and oblate for volume fraction: $f = 10\%$ and $f = 20\%$.

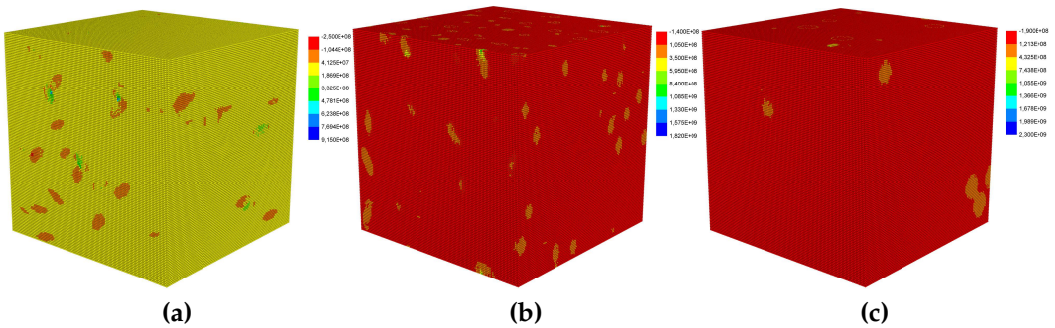

Fig. 3.19 Distribution of local stress σ_{33} for randomly distributed inclusions with different shapes, volume fraction $f = 10\%$ with aspect ratio $Ar = 1.5$ for ellipsoids. (a) oblate inclusions; (b) prolate inclusions; (c) spherical inclusions.

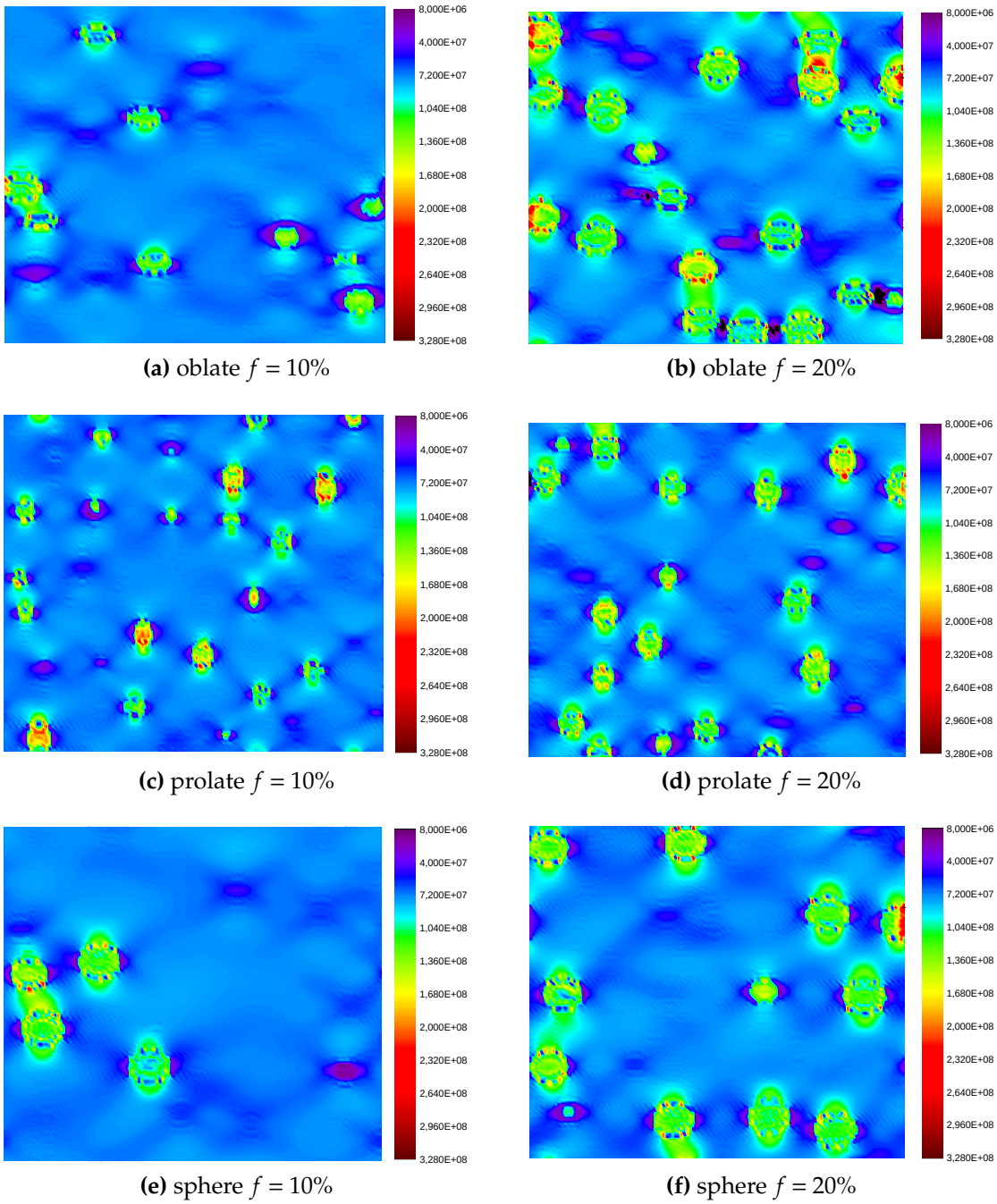

(a) oblate $f = 10\%$ **(b)** oblate $f = 20\%$

(c) prolate $f = 10\%$ **(d)** prolate $f = 20\%$

(e) sphere $f = 10\%$ **(f)** sphere $f = 20\%$

Fig. 3.20 Distribution of local stress σ_{33} for randomly distributed with different shapes and volume fraction in 2D. (a) oblate $f = 10\%$; (b) oblate $f = 20\%$ (c) prolate $f = 10\%$; (d) prolate $f = 20\%$ (e) sphere $f = 10\%$; (d) sphere $f = 20\%$.

-Uniform orientation

The material with uniform direction of fibers is a practical composite in many engineering fields. The effects on the macroscopic response have been studied experimentally and numerically by many researchers (Niandou et al., 1997; Pietruszczak et al., 2002; Salager et al., 2013). The fibers with uniform direction make the composite being anisotropic and macroscopic properties being directionally dependent. Fig.3.21a illustrates the definition of load direction with the fiber orientation by the angle θ. The load is applied on the 33 direction (vertical) and three typical angles are considered: $\theta = 0°, 45°, 90°$. Fig.3.21c, 3.21d, 3.21e show the microstructures with uniform direction of oblate inclusions with the three typical angles. The microsturcture with randomly oriented oblate inclusions is also shown in Fig. 3.21b. It can be seen that the randomly oriented oblate inclusions make the composite isotropic and those structures with uniform directions are directionally dependent. In order to study the effects of orientations, uniaxial tension tests are implemented on those microstructures with the materials properties stated in the previous section (see equation 3.3 and 3.4) and the strain controlled process is performed in the 33 direction (see equation 3.5).

The computational results are shown in Fig.3.22 and 3.23 for two volume fractions: $f = 10\%$ and $f = 20\%$. For both volume fractions the figure clearly shows that the microstructures with randomly oriented inclusions obtain the same material properties for the load direction 11 and 33. The volumetric deformation are also identical for different loading directions. On the contrary, the microstructures with uniform directions exhibit a very different overall response for different inclusion directions. It is indicated that the microstructure with $\theta = 0°$ provides much stiffer effective properties, and the one with $\theta = 45°$ obtains much softer overall response comparing with the other two cases. The volumetric deformation for three angles gives the same trends as the effective response. In short, the numerical results shows clearly that the effective strength of the isotropic composite is path independent while the one of the anisotropic composite is highly path dependent. The comparison of tensile strength with variation of sample orientations is compared for the perfect plastic matrix ($\sigma_0 \leqslant \sigma_{eq}$) and other material parameters remain the same as eqation 3.3 and 3.4. Several different angles are studied from $\theta = 0°$ to $90°$. The final strengths in Fig.3.24a are chosen as the ultimate strength since the lines are stay level. For the strength of the one with $\theta = 0°$ the ultimate strength should be higher than the final stage from the trend of the curve, however, the last strength

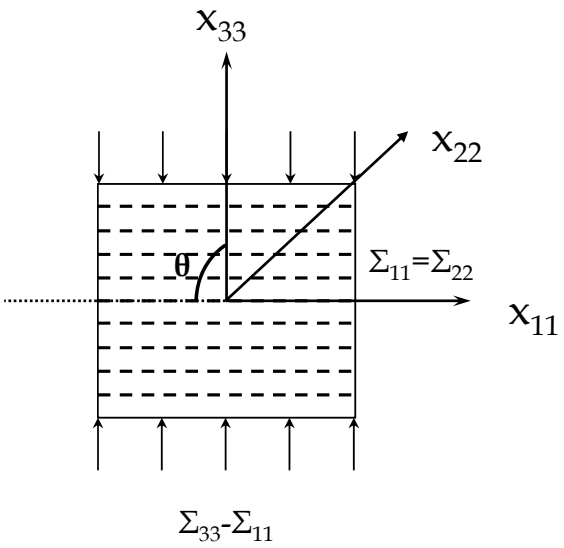

(a) Load direction

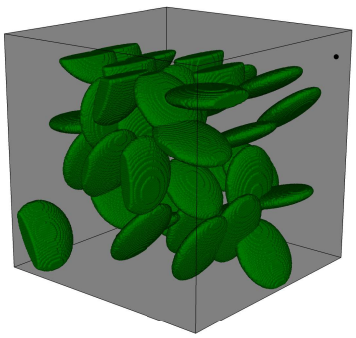

(b) Microstructure 1

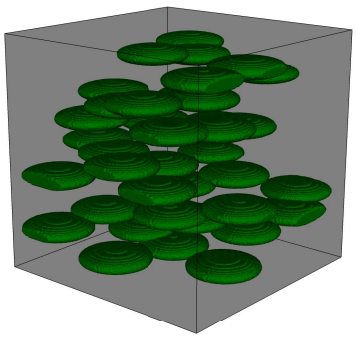

(c) Microstructure 2

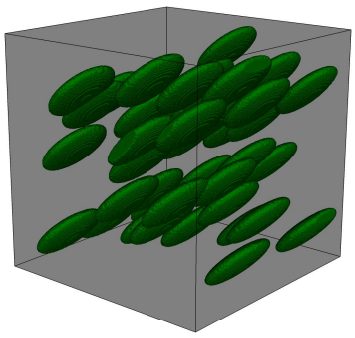

(d) Microstructure 3

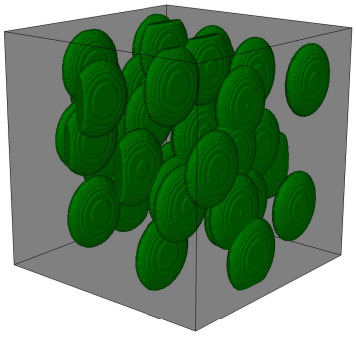

(e) Microstructure 4

Fig. 3.21 Definition of load orientation (a) and microstructure with oblate inclusions: (b) Randomly oriented inclusions; (c) Uniform oriented inclusions with 90^o; (d) Uniform oriented inclusions with 45^o; (e) Uniform oriented inclusions with 0^o.

is chosen. The curve in Fig.3.24b shows clearly the relations between the tensile strength with the inclusion directions and the results agree with the experimental research in (Pietruszczak et al., 2002).

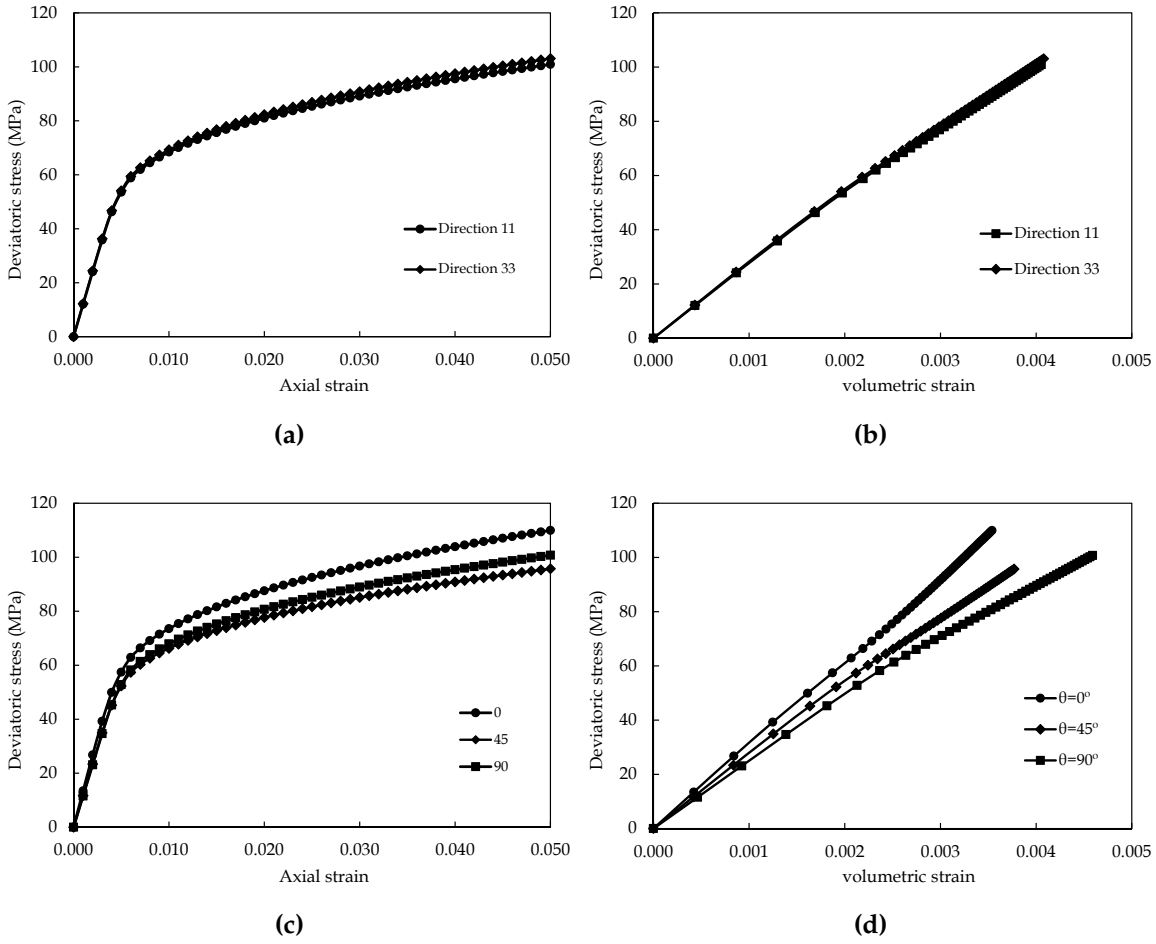

Fig. 3.22 Numerical simulation of uniaxial tests with isotropic and anisotropic microstructures for volume fraction $f = 10\%$: (a) strain and stress curve for microstructure 1: oblate with random orientations; (b) volumetric strain and overall stress curve of microstructures 1; (c) strain and stress curve for anisotropic microstructures: $\theta = 0^o, 45^o, 90^o$; (d) volumetric strain and overall stress curve for anisotropic microstructures.

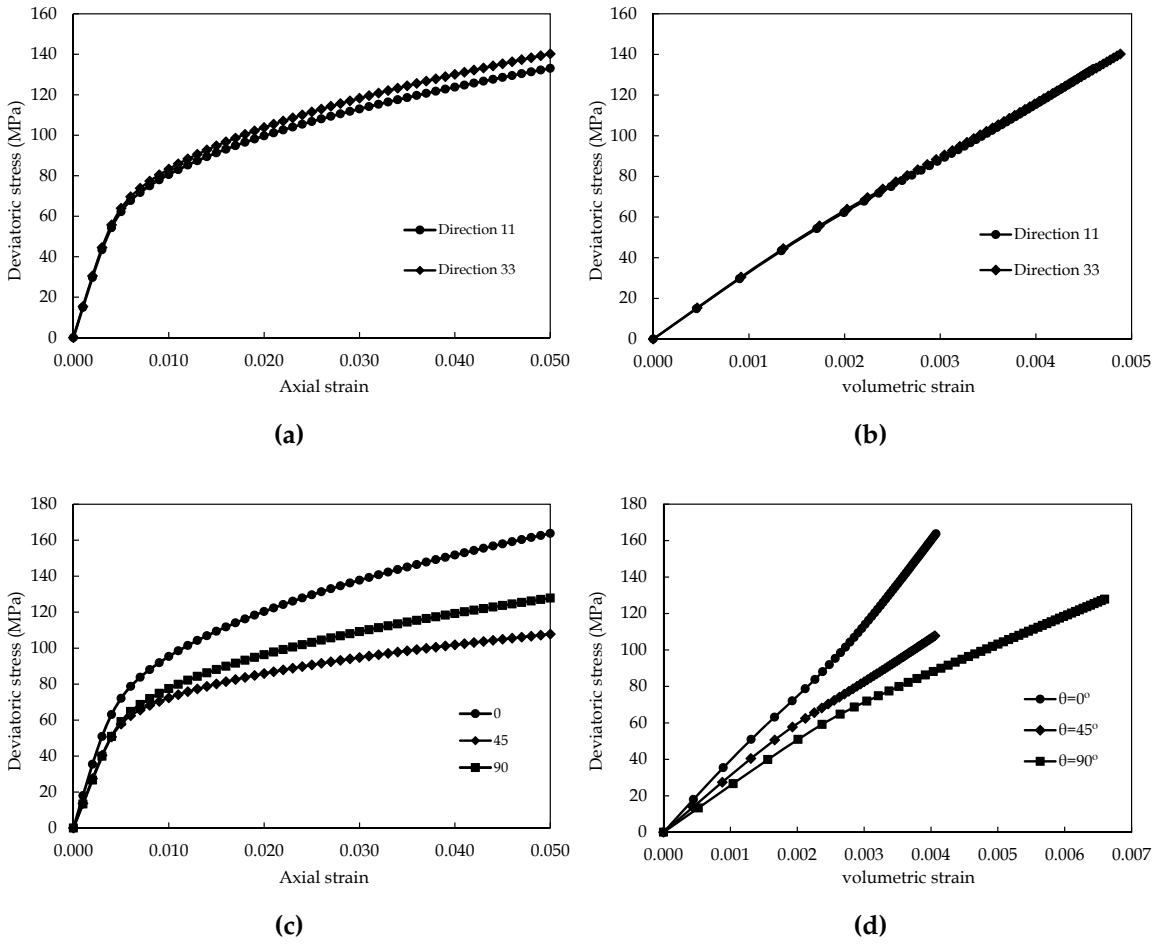

Fig. 3.23 Numerical simulation of uniaxial tests with isotropic and anisotropic microstructures for volume fraction $f = 20\%$: (a) strain and stress curve for microstructure 1: oblate with random orientations; (b) volumetric strain and overall stress curve of microstructures 1; (c) strain and stress curve for anisotropic microstructures: $\theta = 0^o, 45^o, 90^o$; (d) volumetric strain and overall stress curve for anisotropic microstructures.

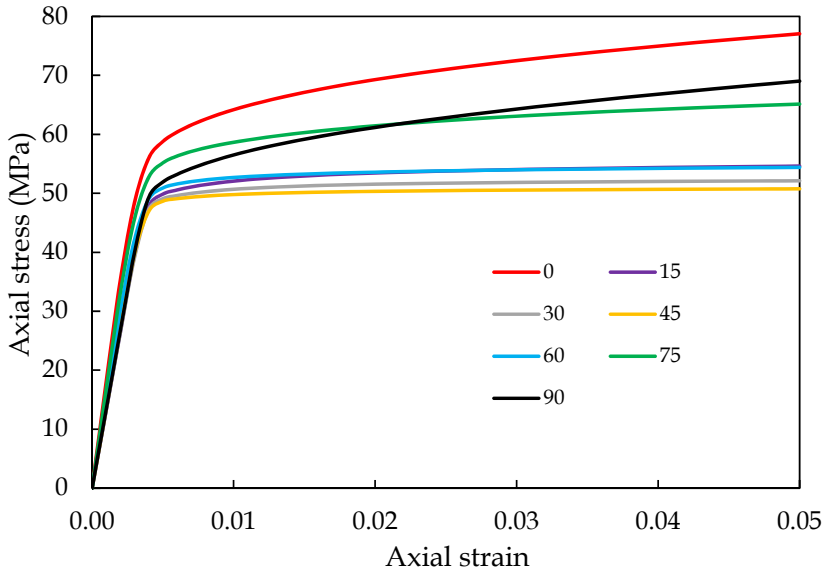

(a)

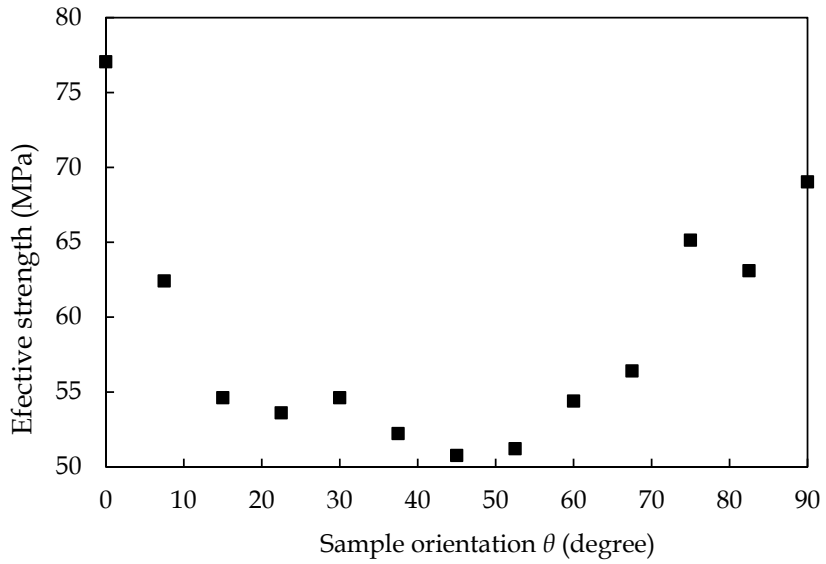

(b)

Fig. 3.24 Effects of orientations on the effective strength under uniaxial tension tests. (a) Overall response with different orientations; (b) Variation of uniaxial tensile strength with sample orientation θ.

3.3 Closing remarks

The effects of microstructure on the overall behaviors of matrix-inclusion type composite are studied in this chapter by using the FFT method. In order to generate the

complex microstructures, a numerical procedure is used and it is dependent of the spatial resolution. Different typical microstructures are generated and simulated by the FFT method to study the effective properties of these composite materials. The effects of microstructure are fully considered: matrix reinforced by one spherical or ellipsoidal inclusion, or by randomly oriented ellipsoidal ones. The shapes, distributions, orientations and sizes of inclusions are accounted for the macroscopic behaviors of the studied composite. Using the FFT method, the micromechanical analysis is fully described with the display of microscopic stress and strain. The investigations indicate that the FFT method is an efficient approach to predict the overall behaviors of composite materials. In the following chapters, the investigation will be extended into the applications of three-phase nonlinear behavior of geomaterials with complex microstructures as well as the porous materials.

Chapter 4

A numerical study of effective mechanical behavior of geomaterials based on Fast Fourier Transform

Abstract

This paper is devoted to the numerical modeling of effective mechanical behaviors of rock like materials by taking into account effects of micro-structure. The numerical model will be based on the Fast Fourier Transform (FFT) technique. We consider a class of rock materials with a micro-structure which can be represented by a continuous matrix phase in which are embedded mineral inclusions. One or several constituent phases exhibit a nonlinear inelastic behavior. The proposed numerical model is firstly assessed by comparing numerical results with reference solutions obtained by direct finite element simulations. It will be then applied to a typical clayey rock which is constituted by an elastic-plastic clay matrix which is reinforced by linear elastic quartz and calcite grains. The proposed numerical model is further extended by including the progressive damage process due to the growth of micro-cracks. Comparisons between numerical results and experimental data will be presented to assess the efficiency of the numerical model.

Keywords: Homogenization, Fast Fourier Transform, Plasticity, Damage, Clayey rocks, Heterogeneous materials

Preprint submitted to Elsivier *May 14, 2015*

4.1 Introduction

During the last decades, clayey rocks have been largely investigated in many countries as a potential geological barrier for underground radioactive waste disposal and sequestration of residual gas. Clayey rocks also constitute the cap rock of many oil and gas reservoirs. On the other hand, shales are investigated as reservoir rocks for the optimal exploration of shale gas. In all these applications, it is crucial to characterize and describe both short and long term hydromechanical behaviors of clayey rocks, in particular plastic deformation and damage process, as well as permeability evolution. As a representative clayey rock, we consider here the Callovo-Oxfordian (COX) claystone from the underground research laboratory of Andra, the French National Agency for radioactive waste management. Extensive laboratory studies have been conducted this material and we do not intend to give here an exhaustive review of all obtained results (Andra, 2005, 2012). Basically, the inelastic mechanical behaviors of the COX claystone can be characterized by the plastic deformation and microcrack induced damage in the clay matrix and at interfaces. The macroscopic responses are strongly influenced by its mineral compositions and the water saturation degree due to the presence of swelling clay minerals such as smectite. Time-dependent behaviours have also been investigated thorough creep tests and as a first approximation can be attributed to viscoplastic deformation and subcritical propagation of microcracks of the clay matrix. Based on experimental results, different kinds of macroscopic constitutive models have first been proposed to describe the elastic, plastic, viscoplastic and damage behaviors of the COX claystone, for instance (Chiarelli et al., 2003; Hoxha et al., 2007; Shao et al., 2006). These macroscopic models can generally capture the overall responses of the material but fail to properly taking into account effects of micro-structure. For example, the macroscopic models are not able to explicitly describe the effects of mineral compositions and spatial distribution of mineral inclusions. In order to improve and complete the macroscopic models, an important effort has been made during the last years on the development of micro-mechanical models based on various homogenization techniques. Concerning clayey rocks, several micro-macro models have also been proposed, for instance (Abou-Chakra Guéry et al., 2008; Shen et al., 2013b, 2012c). In these models, the claystone has been represented as a three phase composite constituted by a clay matrix and quartz and calcite grains. The clay matrix has been further considered as a porous medium composed of a solid phase and spherical

pores (Shen et al., 2013b, 2012c). Some other models have been proposed for modeling the time-dependent behaviours of the claystone (Bikong et al., 2015; Huang et al., 2015; Huang and Shao, 2013; Huang et al., 2014). The models provide an interesting alternative way for modeling heterogeneous rock like materials taking into account effects of micro-structures. However, in order to obtain analytical or semi-analytical formulations, strong assumptions were generally introduced on the description of microstructure. For instance, all mineral inclusions and pores were assumed to be of spherical form and randomly embedded in the solid phase. The real microstructure of most rock like materials is obviously more complex than this simplified representation. In view of not only validating analytical micro-mechanical models but also studying effects of microstructure on macroscopic behaviors, it is needed to develop numerical simulations based a realistic description which should be as close as possible to the real microstructure.

For this purpose, we propose here to apply a numerical method based on the Fast Fourier Transform (FFT). This mathematical technique was successfully applied by Moulinec and Suquet (1994, 1998) as an alternative approach of the finite element method to compute the effective properties of composite materials with a periodic microstructure. This approach was further improved by an accelerated scheme to improve its computational efficiency (Eyre and Milton, 1999; Michel et al., 1999, 2000) and to extend its ability to voids and rigid inclusions (Michel et al., 2001). The main advantage of FFT approach is ability to efficiently consider non-regular geometrical forms of microstructure due to the fact that no volumetric meshing is needed since the heterogeneous material field is discretized into a series of grid points. Different mechanical properties can be assigned on each point according to its location inside the heterogeneous micro-structure. The overall responses at the macroscopic scale are then obtained by the volumetric average on the unit cell of the local stress and strain fields at the microscopic scale (Hill, 1963; Li and Wang, 2008). In this work, Based on the FFT technique, a numerical micro-mechanical model will be proposed to describe the inelastic behavior of the COX claystone. To this end, the clay matrix will described by an elastic plastic model based on a pressure sensitive yield criterion. Then, in order to describe the material softening behavior due to induced damage process, an elastic damage model will be introduced for the calcite grains. Some sensitivity studies will also be presented to show effects of different micro-structures on macroscopic responses. The efficiency of the proposed numerical model will be firstly verified against reference solutions obtained by direct

finite element simulations and through comparisons between numerical results and experimental data.

4.2 Microstructure of COX claystone

The claystone studied here is from the underground research laboratory constructed by Andra in the North-East region of France. The main facilities of the laboratory are located at the depth from 445m to 490m and excavated in a 200m thick sub-horizontal layer of Callovo-Oxfordian formation. The COX claystone is characterized by its low permeability and relatively high mechanical strength. The mineralogical compositions vary with the depth and contain three main phases: clay matrix, calcite grains and tectosilicates mainly composed of quartz grains. A representative microstructure picture of the COX claystone is shown in Figure 4.1 Robinet (2008). At the depth corresponding to the underground research laboratory, the average mineralogical compositions are 40 to 50% of clay minerals, 20 to 27% of calcite and 23 to 25% of quartz. There is also a small quantity of other minerals such pyrite, mica, dolomite, halite and gypse.

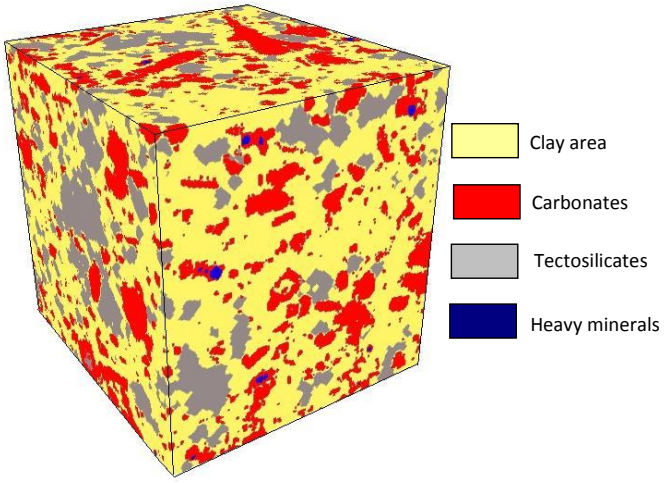

Fig. 4.1 Representative microstructure of COX claystone (Robinet (2008))

The microstructure of the COX claystone is heterogeneous at different scales. In view of micro-macro modeling of its mechanical behaviors, it seems that the following relevant scales should be considered:

- At the nanometer and micrometer scales ($\sim vm$), the clay minerals have a

complex organization with several scales (sheets, particles, aggregates). The size of pores varies from nanometer to micrometer and respectively associated with intra-particular voids (between clay sheets) and inter-particular voids (between particles). It was found that the porosity of the COX claystone contains two representative average sizes, 4nm and 20nm respectively, Andra (2005); Robinet (2008). The total porosity can also vary with the depth.

- At the mesoscopic scale ($vm - mm$), the material is composed of the grains of quartz and calcite embedded in the clay matrix.
- At the macroscopic scale ($mm - cm$), the claystone constituted by the assembly of mineral grains and the clay matrix can be considered as a equivalent homogeneous medium (EHM).

However, in the present work, for the sake of simplicity, the micro-mechanical modeling will be performed on the mesocopic scale. The clay matrix is then considered as a homogeneous continuum whose mechanical behavior is described by an appropriate elastic-plastic model. Therefore, as a first approximation, the heterogeneous claystone at the mesoscopic scale is seen as a matrix-inclusion system. The clay minerals constitute the matrix phase which are reinforced by calcite and quartz grains.

4.3 FFT based numerical method

For the sake of clarity, we consider an inhomogeneous linear elastic material. The unit cell of material is subjected to a uniform macroscopic strain on its boundary $\boldsymbol{E}$. Due to the material heterogeneity, the local stress and strain fields are not uniform. The non-uniform strain field is defined by a periodic fluctuation displacement field $\boldsymbol{u}^*(\boldsymbol{x})$. Therefore, the local strain field inside the unit cell, $\boldsymbol{\varepsilon}(\boldsymbol{u}(\boldsymbol{x}))$, can be expressed by:

$$\boldsymbol{\varepsilon}(\boldsymbol{u}(\boldsymbol{x})) = \boldsymbol{\varepsilon}(\boldsymbol{u}^*(\boldsymbol{x})) + \boldsymbol{E}, \tag{4.1}$$

with the conditions $< \boldsymbol{\varepsilon} >= \boldsymbol{E}$ and $< \boldsymbol{\varepsilon}(\boldsymbol{u}^*(\boldsymbol{x})) >= 0$, the operator $< . >$ denoting the voumetric averaging on the unit cell.

The problem to be solved here is determine the local stress filed using the local constitutive relations and then to evaluate the macroscopic stress by making the

volumetric averaging over the unit cell, as the macroscopic response to the prescribed macroscopic strain. To this end, denote $\mathbb{C}(\boldsymbol{x})$ as the non-uniform local elastic stiffness tensor. The local governing equations are given by:

$$\begin{cases} \boldsymbol{\sigma}(\boldsymbol{x}) = \mathbb{C}(\boldsymbol{x}) : \boldsymbol{\varepsilon}(\boldsymbol{x}) & \forall \boldsymbol{x} \in \Omega \\ \boldsymbol{div}\boldsymbol{\sigma}(\boldsymbol{x}) = 0 & \forall \boldsymbol{x} \in \Omega, \quad u^* \#, \quad \boldsymbol{\sigma} \cdot n - \# \\ \boldsymbol{\varepsilon}(\boldsymbol{x}) = \frac{1}{2}(\nabla \boldsymbol{u}^*(\boldsymbol{x}) + \nabla^T \boldsymbol{u}^*(\boldsymbol{x})) + \boldsymbol{E} & \forall \boldsymbol{x} \in \Omega \end{cases} \tag{4.2}$$

In this relations, the symbol # denotes the periodic condition while $-\#$ the anti-periodic one.

By introducing a homogeneous elastic reference material with a constant stiffness tensor $\mathbb{C}^0$ and after defining a polarization tensor field $\boldsymbol{\tau}(\boldsymbol{x}) = (\mathbb{C} - \mathbb{C}^0) : \boldsymbol{\varepsilon}(\boldsymbol{x})$, the above local problem can be reduced to the periodic Lippman-Schwinger problem Moulinec and Suquet (1998). The solution of this problem in the real space can be determined by using the periodic Green operator $\Gamma^0(\boldsymbol{x})$. One gets:

$$\boldsymbol{\varepsilon}(\boldsymbol{x}) = -\Gamma^0(\boldsymbol{x}) * \boldsymbol{\tau}(\boldsymbol{x}) + \boldsymbol{E}, \tag{4.3}$$

where

$$\boldsymbol{\tau}(\boldsymbol{x}) = (\mathbb{C}(\boldsymbol{x}) - \mathbb{C}^0) : \boldsymbol{\varepsilon}(\boldsymbol{x}). \tag{4.4}$$

The convolution operator in the real space $*$ is difficult to calculate but it can be reduced to a simple product operator in the Fourier space. Indeed, the expression of the Green operator in the Fourier space is explicitly known. Therefore after making the fast Fourier transform, the solution to the local problem can be easily expressed by:

$$\hat{\boldsymbol{\varepsilon}}(\boldsymbol{\xi}) = -\hat{\Gamma}^0(\boldsymbol{\xi}) : \hat{\boldsymbol{\tau}}(\boldsymbol{\xi}) \qquad \forall \boldsymbol{\xi} \neq \boldsymbol{0}, \hat{\boldsymbol{\varepsilon}}(\boldsymbol{0}) = \boldsymbol{E}. \tag{4.5}$$

In this solution, $\hat{\boldsymbol{\tau}}$ and $\hat{\Gamma}^0$ are the polarization tensor and periodic Green operator in Fourier space respectively. Further, the constant stiffness tensor $\mathbb{C}^0$ of the isotropic elastic reference material can be expressed in terms of the two Lamé coefficients λ^0 and μ^0. The Green operator can be explicitly given by:

$$\hat{\Gamma}_{khij}(\boldsymbol{\xi}) = \frac{1}{4\mu^0|\boldsymbol{\xi}|^2}(\delta_{ki}\xi_h\xi_j + \delta_{hi}\xi_k\xi_j + \delta_{kj}\xi_h\xi_i + \delta_{hj}\xi_k\xi_i) - \frac{\lambda^0 + \mu^0}{\mu^0(\lambda^0 + 2\mu^0)}\frac{\xi_i\xi_j\xi_k\xi_h}{|\boldsymbol{\xi}|^4}. \tag{4.6}$$

Therefore, the FFT-based numerical method consists in finding an appropriate non-uniform strain field and the corresponding stress field, which verify the local constitutive relations, equilibrium equations and boundary conditions on the unit cell. To do this, an iterative algorithm is needed. By making use of the Green operator property $\Gamma^0 * (\mathbb{C}^0 : \boldsymbol{\varepsilon}) = \boldsymbol{\varepsilon}$, and based on the previous works by (Moulinec and Suquet, 1994, 1998) , the following iterative algorithm is adopted:

$$
\begin{cases}
\text{Initialization:} & \boldsymbol{\varepsilon}^0(\boldsymbol{x}) = \boldsymbol{E} \qquad \forall \boldsymbol{x} \in \Omega, \\
& \boldsymbol{\sigma}^0(\boldsymbol{x}) = \mathbb{C}(\boldsymbol{x}) : \boldsymbol{\varepsilon}^0(\boldsymbol{x}) \qquad \forall \boldsymbol{x} \in \Omega \\
\text{Iterate } i+1 & \text{the previous } \boldsymbol{\varepsilon}^i \text{and } \boldsymbol{\sigma}^i \text{ being known at each position } \boldsymbol{x} \\
\quad a) & \hat{\boldsymbol{\sigma}}^i = \mathcal{F}(\boldsymbol{\sigma}^i) \\
\quad b) & \text{Verify the convergence and update the stress/strain} \\
\quad c) & \hat{\boldsymbol{\varepsilon}}^{i+1}(\boldsymbol{\xi}) = \hat{\boldsymbol{\varepsilon}}^i(\boldsymbol{\xi}) - \hat{\Gamma}^0(\boldsymbol{\xi}) : \hat{\boldsymbol{\sigma}}^i(\boldsymbol{\xi}) \qquad \forall \boldsymbol{\xi} \neq \boldsymbol{0}, \quad \hat{\boldsymbol{\varepsilon}}^{i+1}(\boldsymbol{0}) = \boldsymbol{E} \\
\quad d) & \boldsymbol{\varepsilon}^{i+1} = \mathcal{F}^{-1}(\hat{\boldsymbol{\varepsilon}}^{i+1}) \\
\quad e) & \boldsymbol{\sigma}^{i+1}(\boldsymbol{x}) = \mathbb{C}(\boldsymbol{x}) : \boldsymbol{\varepsilon}^{i+1}(\boldsymbol{x}) \quad \forall \boldsymbol{x} \in \Omega
\end{cases}
\tag{4.7}
$$

In these relations, $\boldsymbol{x}$ and $\boldsymbol{\xi}$ denote the coordinates in real space and Fourier space, respectively. The symbol $\mathcal{F}$ and $\mathcal{F}^{-1}$ represent correspondingly the FFT and inverse FFT operators. The convergence condition is controlled by the equilibrium equation and performed in Fourier space to avoid the difficulty of the computation for the differential operator:

$$
err^i = \frac{(< \|div\boldsymbol{\sigma}^i(\boldsymbol{x})\|^2 >) \, 1/2}{\| < \boldsymbol{\sigma}^i(\boldsymbol{x}) > \|} = \frac{< \|\boldsymbol{\xi} \cdot \hat{\boldsymbol{\sigma}}^i(\boldsymbol{\xi})\|^2 >^{1/2}}{\|\hat{\boldsymbol{\sigma}}^i(\boldsymbol{0})\|} \leq \omega \tag{4.8}
$$

and the matrix 2-norm is utilized here as the norm of the second order tensor. ω is a chosen value of convergence tolerance.

The choice of the reference stiffness tensor $\mathbb{C}^0$ can significantly affect the rate of convergence. In practice, according to (Moulinec and Suquet, 1998), the best rate of convergence is provided with the following values of Lamé coefficients λ^0 and μ^0)

for the reference material:

$$\begin{aligned}\lambda^0 &= \frac{1}{2}(\inf_{x\in V}\lambda(x)+\sup_{x\in V}\lambda(x))\\ \mu^0 &= \frac{1}{2}(\inf_{x\in V}\mu(x)+\sup_{x\in V}\mu(x))\end{aligned} \tag{4.9}$$

4.3.1 Discrete FFT model

In the above FFT based numerical model, a continuous polarization tensor field should be determined. In practice, in view of its numerical implementation, a discrete FFT based model is defined. We shall determine a discrete distribution of polarization tensor at a limited number of points. Therefore, the unit cell is meshed by a regular grid composed of a limit number of point in each direction in real space. For example, this discrete grid is composed of $N1\times N2\times N3$ voxels in three dimensional case. The coordinates of voxels in real space are denoted by $\boldsymbol{x}_p(i_1,i_2,i_3)$ which are linked to the coordinates in Fourier space, $\boldsymbol{\xi}(i_1,i_2,i_3)$. The number of points in each direction depends on the choice of resolution. The relationships between the two coordinates and the grid information are given by:

$$\boldsymbol{x}_p(i_i,i_2,i_3) = i_k\cdot\frac{T_k}{N_k}, \qquad i_k = 0,1,...,N_{k-1}, \quad k=1,2,3. \tag{4.10}$$

The coordinates of $\boldsymbol{\xi}(i_1,i_2,i_3)$ for the case of N_k is even

$$\boldsymbol{\xi}(i_1,i_2,i_3) = (i_k-\frac{N_k-1}{2})\frac{1}{T_k}, \tag{4.11}$$

and the case of N_k is odd

$$\boldsymbol{\xi}(i_1,i_2,i_3) = (i_k-\frac{N_k}{2}+1)\frac{1}{T_k}, \tag{4.12}$$

where T_k is the period of the model in the kth direction ($k=1,2,3$).

Therefore, the iterative numerical algorithm presented above will be applied to each discrete point $\boldsymbol{x_p}$ in real space or $\boldsymbol{\xi_p}$ in Fourier space.

4.3.2 Application to nonlinear heterogeneous materials

The above numerical method for a linear inhomogeneous material is now extended to nonlinear heterogeneous materials. It is generally convenient to express nonlinear constitutive relations in an incremental form. For this purpose, the total loading path is divided into a limit number of steps N. Starting from the initial conditions, at the end of the step n, the local fields of stress, strain and internal variables $(\boldsymbol{\sigma}^n, \boldsymbol{\varepsilon}^n, \boldsymbol{V}^n)$ are all known. Considering now the loading step $n+1$, an incremental of macroscopic strain $\Delta \boldsymbol{E}^{n+1}$ is applied to the unit cell. The problem to be solved is to find the corresponding macroscopic stress increment $\Delta \boldsymbol{\Sigma}^{n+1}$ by using nonlinear local constitutive relations.

To this end, the iterative algorithm presented above is now applied to each loading step. Consider here the time-independent behavior only. Without loosing the generality, the local nonlinear constitutive relations can be expressed in the following incremental form:

$$\Delta \boldsymbol{\sigma}(\boldsymbol{x}) = \mathbb{C}^{tan}(\boldsymbol{x}) : \Delta \boldsymbol{\varepsilon}(\boldsymbol{x}) \tag{4.13}$$

The fourth order tensor $\mathbb{C}^{tan}(\boldsymbol{x})$ denotes the tangent operator which depends on the loading history and loading direction.

Accordingly, the FFT-based iterative numerical algorithm for nonlinear heterogeneous materials at the loading step $n+1$ is defined by (for the sake of simplicity, the step index $(n+1)$ in omitted in the iteration loop):

$$\begin{cases} \text{Initialization:} & \boldsymbol{\varepsilon}^{(n+1)0}(\boldsymbol{x_p}) = \boldsymbol{\varepsilon}^n(\boldsymbol{x_p}) + \Delta \boldsymbol{E}^{n+1} \qquad \forall \boldsymbol{x}_p \in \Omega, \\ & \boldsymbol{\sigma}^{(n+1)0}(\boldsymbol{x}_p) = \boldsymbol{\sigma}^n(\boldsymbol{x}_p) + \mathbb{C}^{tan(n+1)0}(\boldsymbol{x_p}) : \Delta \boldsymbol{\varepsilon}^{(n+1)0}(\boldsymbol{x_p}) \\ \text{Iterate } i+1 & \text{the previous } \boldsymbol{\varepsilon}^i \text{and } \boldsymbol{\sigma}^i \text{ are known at each position } \boldsymbol{x}_p \\ \quad a) & \hat{\boldsymbol{\sigma}}^i = \mathcal{F}(\boldsymbol{\sigma}^i) \\ \quad b) & \text{Verify the convergence and update the stress/strain} \\ \quad c) & \hat{\boldsymbol{\varepsilon}}^{i+1}(\boldsymbol{\xi}_p) = \hat{\boldsymbol{\varepsilon}}^i(\boldsymbol{\xi}_p) - \hat{\Gamma}^0(\boldsymbol{\xi}_p) : \hat{\boldsymbol{\sigma}}^i(\boldsymbol{\xi}_p) \qquad \forall \boldsymbol{\xi}_p \neq \boldsymbol{0}, \quad \hat{\boldsymbol{\varepsilon}}^{i+1}(\boldsymbol{0}) = \boldsymbol{E}^{(n+1)} \\ \quad d) & \boldsymbol{\varepsilon}^{i+1} = \mathcal{F}^{-1}(\hat{\boldsymbol{\varepsilon}}^{i+1}) \\ \quad e) & \boldsymbol{\sigma}^{i+1}(\boldsymbol{x}_p) = \boldsymbol{\sigma}^n(\boldsymbol{x}_p) + \mathbb{C}^{tan(i+1)}(\boldsymbol{x_p}) : \Delta \boldsymbol{\varepsilon}^{i+1}(\boldsymbol{x_p}) \quad \forall \boldsymbol{x}_p \in \Omega \\ \quad f) & \text{update } \boldsymbol{V}^{i+1} \text{ from } \boldsymbol{\varepsilon}^{i+1} \text{ and } \boldsymbol{V}^i \end{cases} \tag{4.14}$$

4.3.3 Local constitutive relations

Based on the microstructure description of the COX claystone, we consider first the case of a heterogeneous composite composed of an elastic-plastic matrix in which are embedded two linear elastic inclusions. For the two inclusion phases, the tangent operators are constant and defined by their elastic stiffness tensors. The local mechanical behavior of the matrix phase is described by an isotropic elastic-plastic model based on a Drucker-Prager type yield criterion, which is written by:

$$f = q + \alpha^p(\gamma^p)(p - c_p) \leq 0, \tag{4.15}$$

where p and q are two basic stress invariants, namely the mean stress $p = \frac{1}{3}tr(\boldsymbol{\sigma})$ and the equivalent shear stress $q = \sqrt{\frac{3}{2}\boldsymbol{s} : \boldsymbol{s}}$, $\boldsymbol{s}$ being the deviatoric stress tensor. The parameter c_p denotes the material cohesion coefficient. The function $\alpha^p(\gamma^p)$ defines the current frictional coefficient. The variable γ^p denotes the equivalent plastic shear strain and serves as the scalar internal variable. Further, an isotropic plastic hardening law is adopted here and it is given by:

$$\alpha^p(\gamma^p) = \alpha_m^p - (\alpha_m^p - \alpha_0^p)e^{-b\gamma^p} \tag{4.16}$$

The parameters α_0^p and α_m^p represent respectively the initial and ultimate values of the frictional coefficient while the parameter b controls the hardening rate. Moreover, as for most rock like materials, a non-associated plastic flow rule is used here in order to better describe plastic volumetric strain. The plastic potential is given by:

$$Q = q + \beta^p(\gamma^p)p \tag{4.17}$$

The coefficient β^p controls the rate of plastic volumetric strain and is considered as a function of the equivalent plastic shear strain as well:

$$\beta^p(\gamma^p) = \beta_m^p - (\beta_m^p - \beta_0^p)e^{-b_1\gamma^p} \tag{4.18}$$

The parameters β_0^p and β_m^p are respectively the initial and ultimate values of the volumetric dilation coefficient β^p, and b_1 controls its evolution rate.

The time-independent local constitutive relations of the matrix phase can be

written in the following incremental form:

$$\Delta\boldsymbol{\sigma} = \mathbb{C}^m : (\Delta\boldsymbol{\varepsilon} - \Delta\boldsymbol{\varepsilon}^p), \qquad \Delta\boldsymbol{\varepsilon}^p = \Delta\lambda^p \frac{\partial Q}{\partial \boldsymbol{\sigma}}, \qquad \Delta\lambda^p \geqslant 0 \tag{4.19}$$

$\Delta\boldsymbol{\varepsilon}^p$ denotes the incremental plastic strain tensor, $\mathbb{C}^m$ is the elastic stiffness tensor of the matrix. The plastic multiplier $\Delta\lambda^p$ depends on the current plastic state and loading/unloading criterion and it is determined through the plastic consistency condition. The equivalent plastic shear strain increment is defined by $\Delta\gamma^p = \sqrt{\frac{2}{3}(\text{dev}\,\Delta\boldsymbol{\varepsilon}^p) : (\text{dev}\,\Delta\boldsymbol{\varepsilon}^p)}$. It is seen that $\Delta\lambda = \Delta\gamma^p$. After the determination of the plastic multiplier, the tangent elastic-plastic operator of the matrix $\mathbb{C}^{tan}$ takes the form:

$$\begin{cases} \mathbb{C}^{tan} = \mathbb{C}^m - \dfrac{(\mathbb{C}^m : \frac{\partial f}{\partial \boldsymbol{\sigma}}) \otimes (\mathbb{C}^m : \frac{\partial Q}{\partial \boldsymbol{\sigma}})}{\frac{\partial f}{\partial \boldsymbol{\sigma}} : \mathbb{C}^m : \frac{\partial Q}{\partial \boldsymbol{\sigma}} - \frac{\partial f}{\partial \gamma^p}} \; ; & f = 0 \text{ and } \dot{f} = 0 \\ \mathbb{C}^{tan} = \mathbb{C}^m \; ; & \text{else} \end{cases} \tag{4.20}$$

The above local constitutive relations are then used in the iterative algorithm for computing the local stress increment $\Delta\boldsymbol{\sigma}$ and the equivalent shear strain increment $\Delta\gamma$ from the local strain increment $\Delta\boldsymbol{\epsilon}$.

4.4 Assessment of numerical model

In this section, the efficiency of the FFT-based micro-mechanical model is verified through comparisons between numerical results and reference solutions obtained from finite element simulations and experimental data respectively.

4.4.1 Comparison with Finite Element solutions

We consider here a simplified microstructure which is a cubic unit cell containing a centered spherical inclusion, as shown in Figure 4.2a. The unit cell is meshed into discrete points by a regular grid in 3 dimensions. In order to study effects of resolution, three different grids are used here, namely $32\times32\times32$, $64\times64\times64$ and $128\times128\times128$ voxels.

The heterogeneous material in the unit cell is composed of an elastic plastic matrix and an elastic inclusion. The elastic modulus and Poisson's ratio of the inclusion are:

$$E_i = 100GPa, \nu_i = 0.2,$$

The elastic and plastic parameters of the matrix are based on those of the clay matrix in the COX claystone Shen et al. (2013b). The typical values are given in Table 4.1.

Table 4.1 Elastic-plastic parameters of the clay matrix

E_m	ν_m	α_0^p	α_m^p	b	β_0^p	β_m^p	b_1	C_p
3GPa	0.3	0.4	0.9	400	0.1	0.8	400	14MPa

In the first case, the unit cell is subjected to a uniaxial compression along its 3*rd* axis and the prescribed macroscopic strains are:

$$E_{33} < 0 \quad E_{11} = E_{22} = E_{12} = E_{23} = E_{31} = 0. \tag{4.21}$$

The homogenized mechanical response of the unit cell is respectively evaluated by direct simulation using finite element method and the FFT-based micro-mechanical model. The comparison of stress-strain curve between the two solutions is illustrated in Figure 4.2. Note that the finite element solution is here considered as the reference solution. One can note that the numerical result obtained with the FFT-based micro-mechanical model is very close to the reference solution.

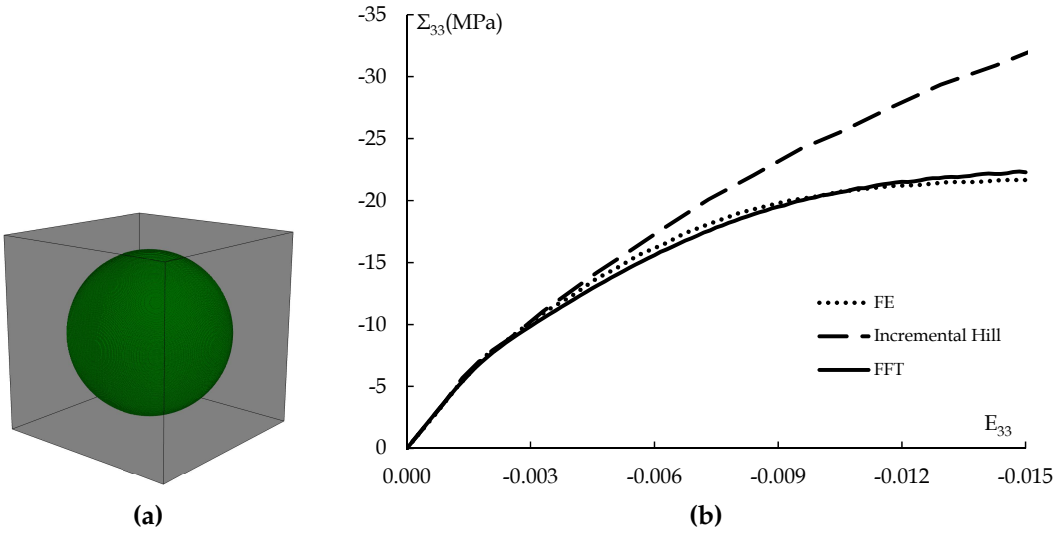

Fig. 4.2 Comparison FFT method with FE solution: (a) Microstructure of the unit cell; (b) Comparison of uniaxial compression test.

4.4.2 Influences of microstructure

Compared with analytical or semi-analytical micro-macro models Shen et al. (2012b, 2013b), the advantage of the FFT-based numerical micro-mechanical model is the ability to investigate different kinds of inclusion geometry and distribution. Some comparative studies are presented here. Consider again a heterogeneous material with an elastic-plastic matrix and linear elastic inclusions. Several kinds of microstructure are considered. The first one corresponds to an random distribution of inclusions in the matrix, as shown in Figure 4.3a in the $3D$ configuration. For the sake of convenience, two sectional drawings in the $2D$ configuration are also presented in Figure 4.3b. On the other hand, some regular distributions of inclusions are also studied, for instance, one sphere in the center and eight $\frac{1}{8}$ spheres in the corner (see Figure 4.4). The white phase stands for the matrix, black for the phase 1 and grey for the phase 2 while the blue phase for the case where the averaged properties of the phases 1 and 2 are used. In this study the interfaces between different phases are assumed to be perfectly bonded which means that the strain and stress are continuous across the interfaces. Imperfect interfaces will be further investigated in the future work by introducing for example a new inter-phase as a very thin bond layer (Monchiet and Bonnet, 2012).

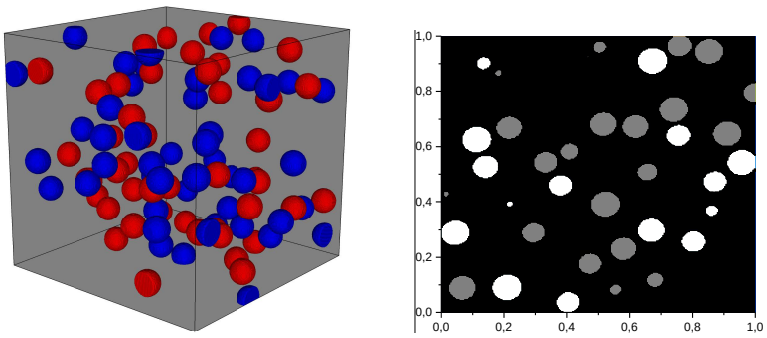

(a) 3D unit cell **(b)** 2D sectional face

Fig. 4.3 Microstructure simulated with the FFT method for two-phase randomly distributed uniform inclusions in the matrix. Spatial resolution: $256 \times 256 \times 256$.

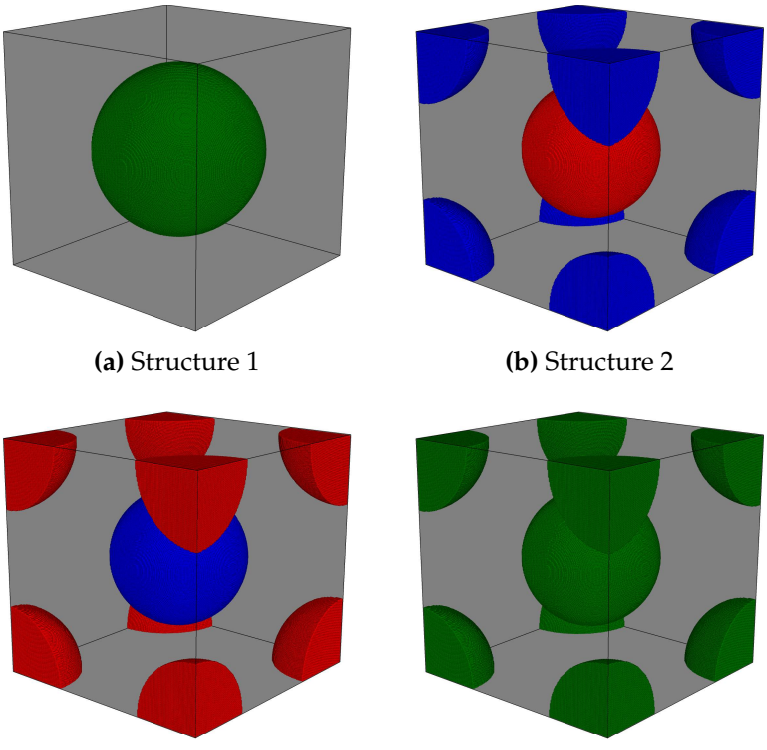

(a) Structure 1 **(b)** Structure 2

(c) Structure 3 **(d)** Structure 4

Fig. 4.4 Regular distributions of inclusions in the unit cell in 3D (blue: phase 1, red: phase 2 and green: averaged properties of phase 1 and phase 2).

The elastic parameters for inclusions are respectively: $E_1 = 95GPa, \nu_2 = 0.27$ for the phase 1 and $E_2 = 30GPa, \nu_2 = 0.15$ for the phase 2, and their averaged properties are $E_i = 62.5GPa, \nu_i = 0.21$. The volume fraction of inclusions is 10% for each phase.

The matrix behavior is characterized by the following elastic and plastic parameters: $E_m = 3GPa, \nu_m = 0.3$, $\alpha_0 = 0.4, \alpha_m = 0.9, b = 400, \beta_0 = 0.1, \beta_m = 0.8, b_1 = 400$.

The macroscopic response of the heterogeneous material is studied for the different kinds of microstructure in a triaxial test with $5MPa$ confining pressure. From Figure 4.5, one can see that the structure with one centered inclusion with the averaged elastic properties of two inclusion phases gives a stiffer mechanical behavior than the other micro-structures with scattered inclusions. On the other hand, the macroscopic mechanical responses are nearly the same for three micro-structures with different distributions of two inclusions phases. This can be explained by the fact that the contrast of elastic properties between the two inclusion phases is small enough so that the change of their relative position in the unit cell does not affect the macroscopic response. However, at the microscopic scale, the local strain and stress distributions can be quite different between the three micro-structures. For instance, the vertical stress distributions are presented in Figures 4.6. One can see that the spatial distribution of inclusions modifies the local stress field.

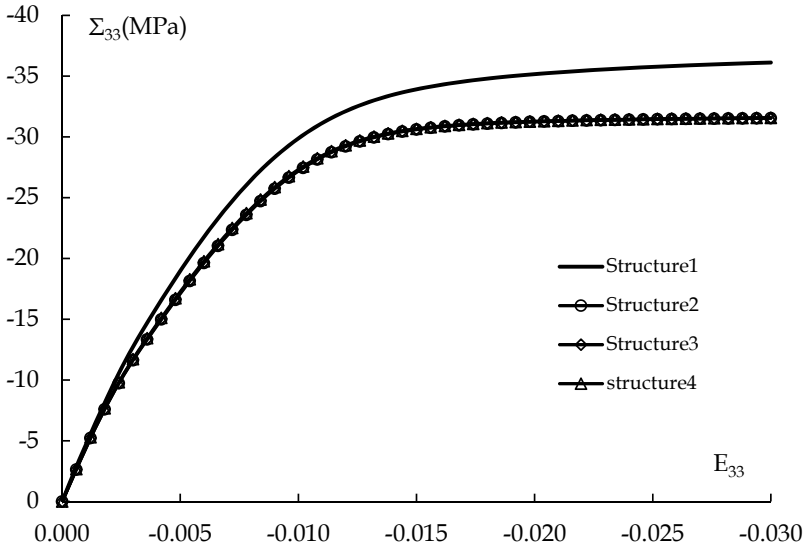

Fig. 4.5 Macroscopic stress-strain curves of composite: comparison between different microstructures with regular distributions of inclusion with a volume fraction f=20%

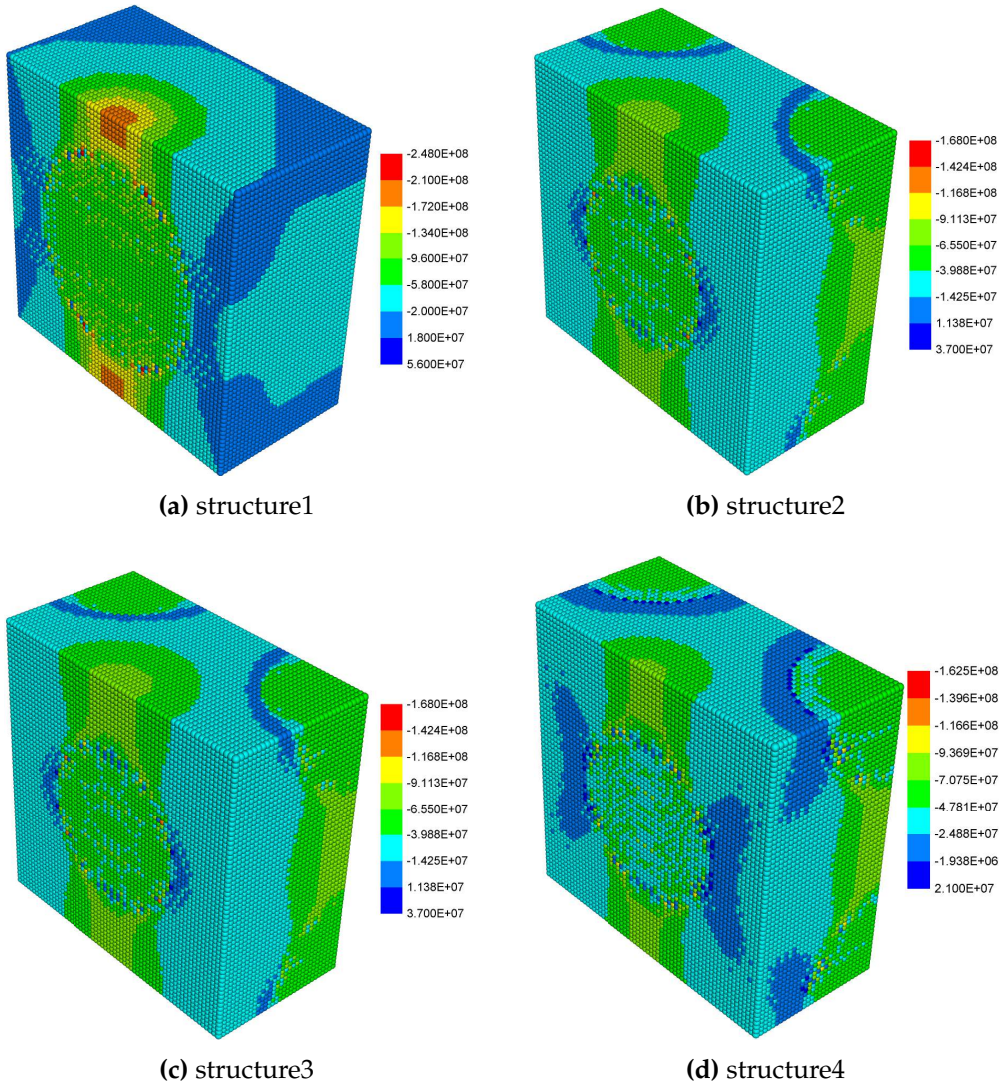

(a) structure1 **(b)** structure2

(c) structure3 **(d)** structure4

Fig. 4.6 Distributions of vertical stress in the unit cell for four different descriptions of microstructrue

For the microstructure with a random distribution of inclusions, macroscopic stress-strain curves are presented in Figure 4.7 for different sizes of inclusion. It is seen that the microstructure with smaller size inclusions gives a stiffer mechanical response. In Figure 4.8, the local stress distributions of axial stress are presented for both uniaxial compression test and triaxial compression test with 5MPa confining pressure. It is seen that strong local stress concentrations can be found around inclusions. In some zone, local tensile stresses are obtained which can be responsible of cracking process. The tensile stress is significantly reduced by the confining pressure effect. It is means that material damage is attenuated under high confining

pressure conditions. This is in agreement with most experimental data for rock like materials.

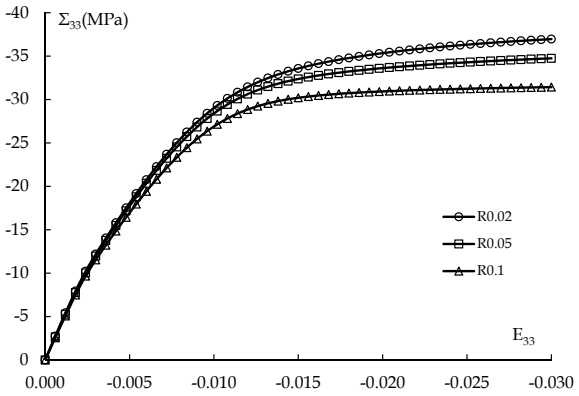

Fig. 4.7 Macroscopic stress-strain curves of composite with random distribution of inclusions with a volume fraction f=20%: effects of inclusion size

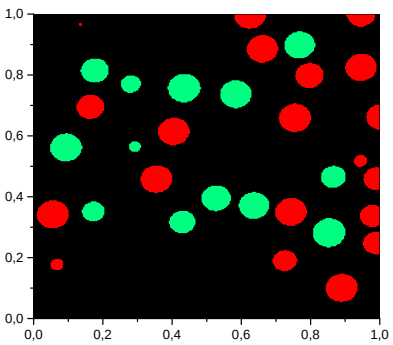

(a) Microstructure

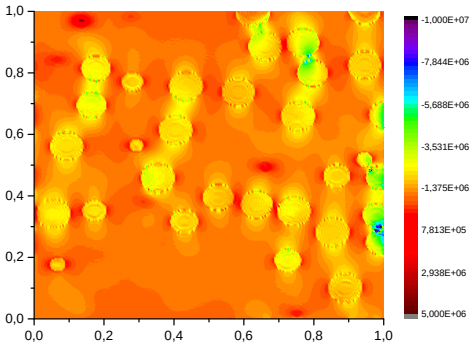

(b) Microscopic stress (Σ_{33}) under uniaxial compression

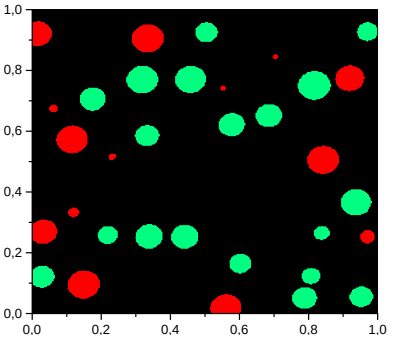

(c) Microstructure

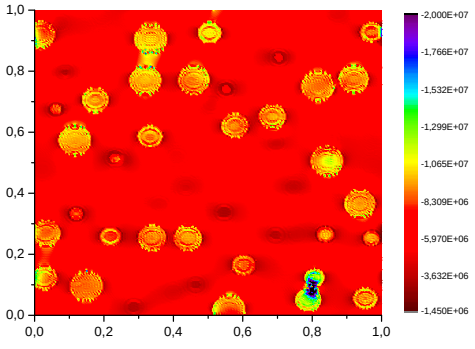

(d) Microscopic stress (Σ_{33}) under triaxial compression 5*MPa*

Fig. 4.8 Local distributions of axial stress in uniaxial and triaxial compression tests, obtained with a resolution of $256 \times 256 \times 256$

Comparison with experimental data

The proposed FFT-based model is now applied to modeling the mechanical behavior of COX claystone. As illustrated in Figure 4.1, as a first approximation, the calcite and quartz grains are randomly distributed in the clay matrix and can be considered as of spherical shape. The elastic properties of calcite and quartz are determined from typical values found in literature Abou-Chakra Guéry et al. (2008). The elastic parameters of the clay matrix are obtained from an inverse procedure of Mori-Tanaka scheme from the experimental values of macroscopic elastic properties of the claystone and those of calcite and quartz. For the determination of the plastic parameters of the clay matrix, the following methodology is adopted. These parameters are first identified by the optimal numerical fitting of stress-strain curves obtained in a uniaxial or triaxial compression test on a sample with a given mineralogical composition. The triaxial compression test on the sample from the depth of $482.2m$ is used for the identification of plastic parameters (see Figure 4.9f). The obtained values are then applied to other tests on samples with different mineralogical compositions. The selected values are given in Table 4.2.

Table 4.2 Typical elastic and plastic parameters for COX claystone

Phase	Clay (f_0)	Calcite (f_1)	Quartz (f_2)
Elastic	$E = 3GPa$ $\nu = 0.3$	$E = 95GPa$ $\nu = 0.27$	$E = 101$ $\nu = 0.06$
Plastic	$\alpha_m^p = 0.7$ $b = 300$ $\beta_0^p = -2.5$ $\beta_m^p = 0.1$ $b_1 = 300$ $c_p = 25MPa$		

Using the proposed FFT-based micro-mechanical model and above parameters, the mechanical responses of the COX claystone in uniaxial and triaxial compression tests are evaluated for samples with different mineralogical compositions. Comparisons between numerical results and experimental data are presented in Figure 4.9. An overall good agreement is obtained. It seems that the numerical micro-mechanical model is able to account for the main features of the mechanical behavior of the claystone such as the volumetric compressibility - dilatancy transition and

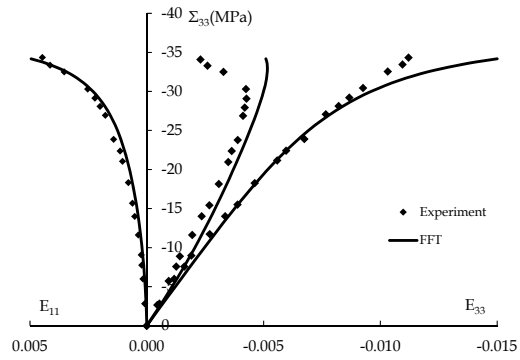

(a) Depth 466.8m, $f_0 = 51\%$, $f_1 = 26\%$, $f_2 = 23\%$

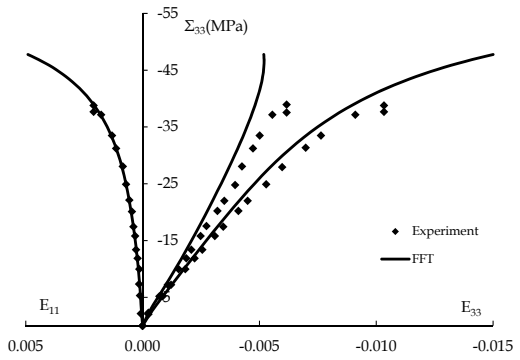

(b) Depth 451.5m, $f_0 = 49\%$, $f_1 = 19\%$, $f_2 = 32\%$

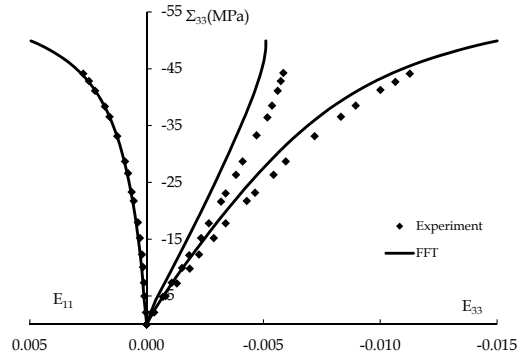

(c) Depth 451.4m, $f_0 = 47\%$, $f_1 = 31\%$, $f_2 = 22\%$

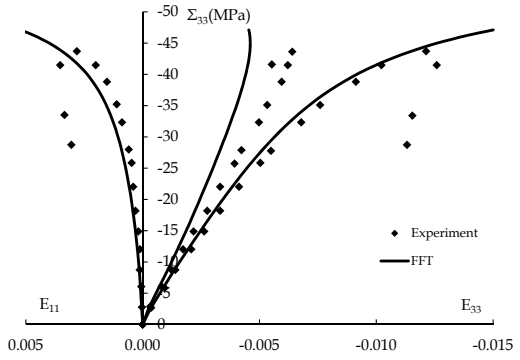

(d) Depth 469.0m, $f_0 = 44\%$, $f_1 = 33\%$, $f_2 = 23\%$

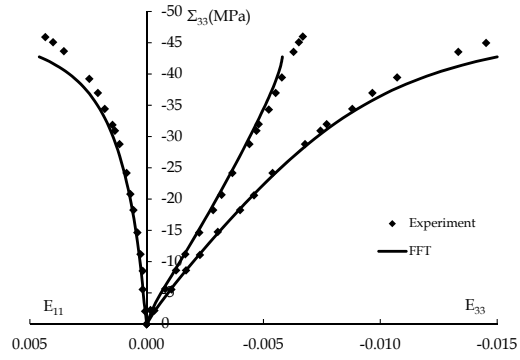

(e) Depth 469.1m, $f_0 = 55\%$, $f_1 = 23\%$, $f_2 = 22\%$

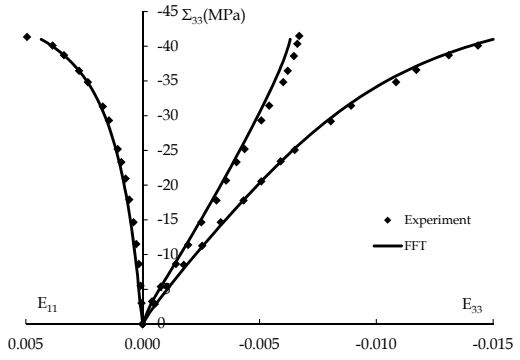

(f) Depth 482.2m, $f_0 = 60\%$, $f_1 = 26\%$, $f_2 = 14\%$

Fig. 4.9 Compression between numerical results and experimental data: (a) uniaxial compression; (b) triaxial compression under 5MPa confining pressure; (c) triaxial compression under 10MPa confining pressure; (d) triaxial compression under 5MPa confining pressure; (e) triaxial compression under 10MPa confining pressure; (f) triaxial compression under 10MPa confining pressure.

confining pressure effects. Compared with analytical and semi-analytical micro-macro models, the present model has the potential ability to consider various kinds of microstructure in order to reproduce as closely as possible real heterogeneous micro-structures of materials. It is the objective of future works to perform FFT-based micro-mechanical modeling on micro-structures issued from microscopic analyses.

4.5 Influence of induced damage

In the micro-mechanical model presented above, only the plastic deformation of the clay matrix is taken into account. However, according to some microscopic analyses with digital image correlation technique, micro-cracks can initiate and propagate in the claystone around interfaces, inside the clay matrix and calcite grains Bornert et al. (2010); Chiarelli et al. (2003). The micro-cracking process affects both mechanical behavior and transport properties such as permeability. The description of whole micro-cracking process is an open issue and will be dealt with in future works. In the present work, it is proposed to use a simplified way to study effects of local micro-cracking process on the macroscopic behavior of the claystone. It is assumed that the mechanical behavior of the calcite phase can be described by an isotropic elastic damage model. For this purpose, a scalar internal variable d is introduced to represent the density of micro-cracks. The elastic stiffness tensor $\mathbb{C}^c$ is affected by the damage process. Under the isothermal condition, its free energy function is written as:

$$w(\boldsymbol{\varepsilon}, d) = \frac{1}{2}\boldsymbol{\varepsilon} : \mathbb{C}^c(d) : \boldsymbol{\varepsilon} \tag{4.22}$$

The state law of the elastic damaged material is then written as:

$$\boldsymbol{\sigma} = \frac{\partial w}{\partial \boldsymbol{\varepsilon}} = \mathbb{C}^c(d) : \boldsymbol{\varepsilon} \tag{4.23}$$

The thermodynamical conjugate force associated with the damage variable is then defined as:

$$Y_d = -\frac{\partial w}{\partial d} = -\frac{1}{2}\boldsymbol{\varepsilon} : \frac{\partial \mathbb{C}^c(d)}{\partial d} : \boldsymbol{\varepsilon} \tag{4.24}$$

The intrinsic mechanical dissipation related to the damage process satisfies the

following inequality:

$$Y_d \dot{d} \geq 0 \tag{4.25}$$

For an isotropic material, the induced damage affects both the bulk and shear modulus of the calcite phase k^c and μ^c:

$$k^c(d) = k_0^c[1-\alpha_1 d], \quad \mu^c(d) = \mu_0^c[1-\alpha_2 d] \tag{4.26}$$

k_0^c and μ_0^c are the initial elastic modulus of the calcite phase. The parameters α_1 and α_2 are introduced to define different damage effects on the two elastic parameters. However, for the sake of simplicity, we take here $\alpha_1 = \alpha_2 = 1$, as largely used in classical damage models (Lemaitre and Desmorat, 2005; Mazars, 1984). Thus, the elastic stiffness tensor of the damaged calcite phase becomes:

$$\mathbb{C}^c(d) = 2\mu^c(d)\mathbb{K} + 3k^c(d)\mathbb{J} = (1-d)\mathbb{C}_0^c \tag{4.27}$$

A damage criterion should be defined to determine the evolution of damage variable. In the framework of thermodynamics, the damage criterion is a scalar valued function of the conjugate damage force Y_d. However, for the sake of simplifying numerical implementation, it is assumed that the damage evolution is controlled by an equivalent strain seen as the damage driving force. Under compression-dominant loading conditions, it is assumed that the damage evolution cannot be introduced by the compressive volume strain but mainly driven by shear strain. Thus the following equivalent shear strain is defined as the damage driving force:

$$F_c = max(F_{c0}, \varepsilon_{eq}^c), \quad \varepsilon_{eq}^c = \sqrt{\frac{1}{2}\boldsymbol{e} : \boldsymbol{e}}, \quad \boldsymbol{e} = \boldsymbol{\varepsilon} - \frac{tr\boldsymbol{\varepsilon}}{3}\boldsymbol{I} \tag{4.28}$$

Based on some previous works (Lemaitre and Desmorat, 2005; Mazars, 1984), then the damage criterion is here used for the calcite phase:

$$f_c = (1 - \frac{1}{exp[B_c * (F_c - F_{c0})]}) - d \leq 0 \tag{4.29}$$

The parameters B_c and F_{c0} respectively controls the damage evolution rate and defines the initial damage threshold. They can be identified from a uniaxial compression test.

The isotropic damage model is now used in the FFT based micro-mechanical

model for describing the local stress-strain relation of the calcite phase. In order to show the effect of induced damage of the calcite on the macroscopic behavior of the composite material, the stress-strain curves in a triaxial compression test are presented in Figure 4.10 with different situations. A two phase composite (matrix and calcite) is here studied and the volume fraction of the calcite phase is 14%. We compare the local mechanical response of the calcite with (black dash line) and without induced damage process (black solid line), as well as its impact on the macroscopic response of the composite. Three cases are illustrated and compared, composite without induced calcite damage (blue line), composite with full damaged calcite (red line) and composite with partially damaged calcite (green line). It can be seen that the overall behavior of the composite without damage is characterized by an asymptotic perfect plastic deformation phase. In the case of full damaged composite, the calcite phase is completely removed and replaced by a void phase. One recovers the elastic-plastic behavior of the matrix. In the case of partially damaged composite, a strain softening behavior is obtained due to the degradation of elastic properties of the calcite. However, due to the interaction between the matrix and inclusions and the compression loading condition, the calcite phase is not completely damaged and there is some residual mechanical strength which is between those of undamaged and fully damaged cases.

A sensitivity study is also performed on the influences of two damage parameters on the macroscopic behavior of composite. Stress-strain curves in a triaxial compression test with different values of F_{c0} and B_c are presented in Figure 4.11. As expected, when the value of F_{c0} is smaller, the damage process occurs earlier. When the value of B_c is higher, the effect of damage is stronger leading to a lower compressive strength (peak stress).

The isotropic damage model is now applied to characterize the local mechanical behavior of calcite in the COX claystone. Triaxial compression tests are studied by using the FFT-based micro-mechanical model. Two examples are presented in Figures 4.12 and 4.13 with comparisons between numerical results and experimental data. It is seen that due to the induced damage process of calcite, one obtains a strain softening behavior after the peak stress. This peak stress followed by a material softening is generally observed in most clayey rocks Andra (2005). Therefore, the micro-mechanical model incorporating local damage process is more close to experimental evidences. However, the simplified model used here should be improved in view of better describing the process of debonding and micro-cracking

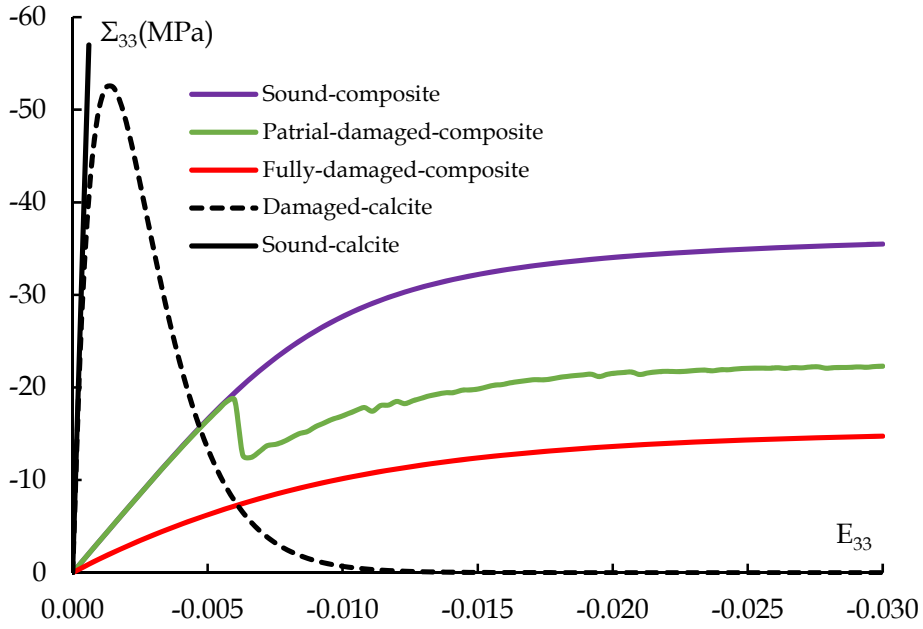

Fig. 4.10 Damage effects in a triaxial compression test, Blue line: undamaged composite; red line: fully damaged composite; green line: partially damaged composite; black solid line: sound calcite phase; black dash line: damaged calcite phase.

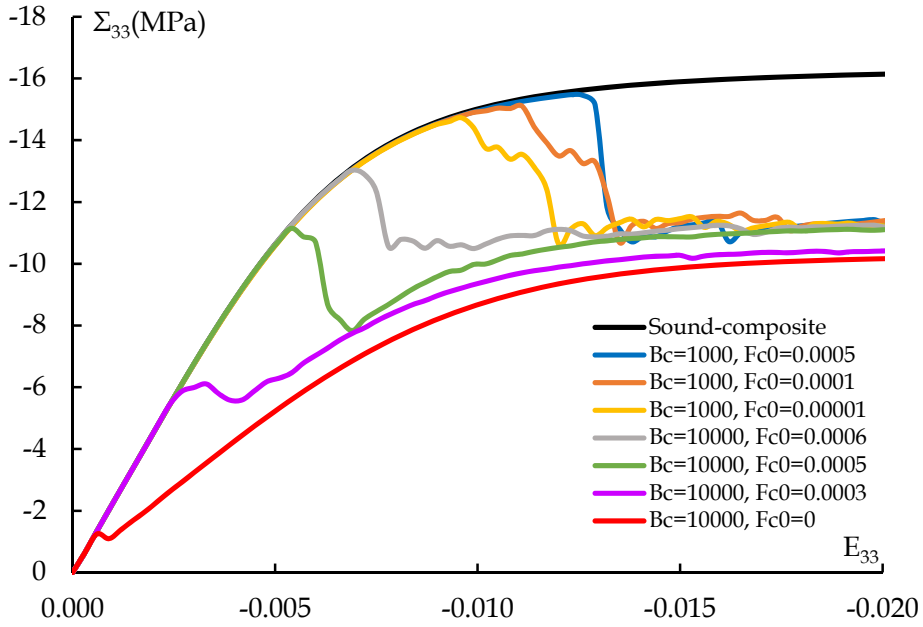

Fig. 4.11 Influences of damage parameters on macroscopic stress-strain responses in a triaxial compression test

in heterogeneous rocks like materials.

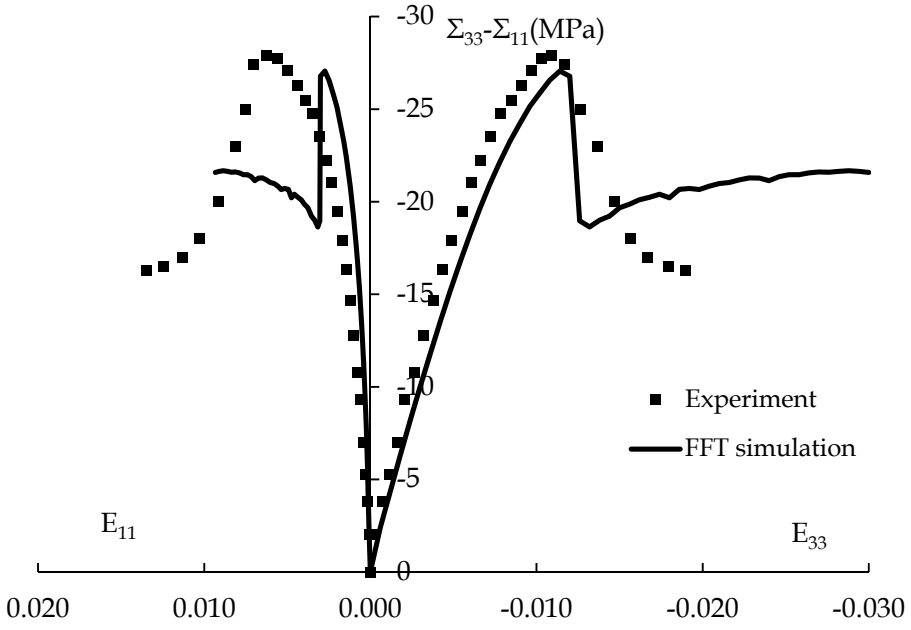

Fig. 4.12 Stress-strain curves in a triaxial compression test with 6MPa confining pressure on COX claystone using FFT-based micro-mechanical elastic plastic damage model

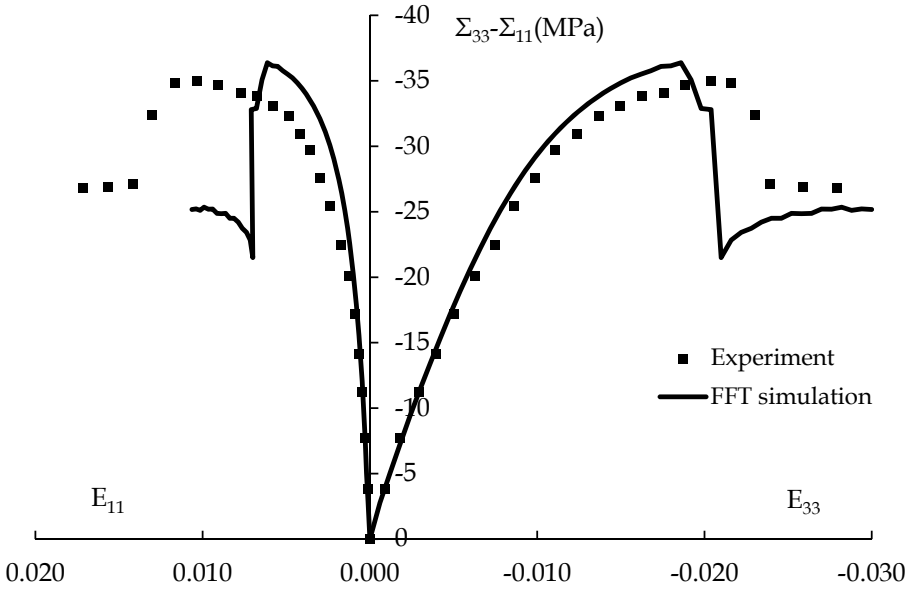

Fig. 4.13 Stress-strain curves in a triaxial compression test with 12MPa confining pressure on COX claystone using FFT-based micro-mechanical elastic plastic damage model

4.6 Conclusion

In this work, a FFT-based numerical micro-mechanical model has been proposed for modeling heterogeneous rock like materials. The non-uniform local strain field due to material heterogeneities has been determined with the help of periodic Green operator and Fourier Transform. The unit cell of heterogeneous materials is meshed by a discrete set of grid points. It is possible to attribute a local constitutive behavior to each point. Therefore, the proposed model is very suitable to heterogeneous materials with irregular and complex micro-structures.

The proposed model has been implemented for rock like materials with elastic-plastic phases. Its efficiency was checked against some reference solutions obtained from direct finite element simulations. Effects of microstructure on macroscopic responses of some specific composite materials have been studied. It was found that the macroscopic response can be affected by the spatial distribution of inclusions and also by the size of randomly distributed inclusions. Compared with analytical or semi-analytical micro-mechanical models, the FFT-based numerical model provides the ability to account for such micro-structural effects on macroscopic responses.

The proposed model has been applied to the COX claystone composed of an elastic-plastic clay matrix and linear elastic calcite and quartz inclusions. An overall agreement has been obtained between numerical results and experimental data. In particular, the proposed model well reproduced the main features of mechanical behaviors of the claystone such as volumetric compressibility - dilatancy transition and confining pressure effects and accounts for the effects of mineralogical compositions. A simple isotropic damage model has also been implemented in the FFT-based micro-mechanical model to describe the local micro-cracking process around mineral inclusions. The material softening behavior of the claystone in the post-peak regime was correctly reproduced. Some other aspects should be investigated in future works, for instance, effects of porosity and interface debonding process.

Chapter 5

Micromechanical analysis of porous materials based on FFT method

5.1 Introduction

Porous materials (rocks, chalk, sandstone, cement based materials, etc.) are widely studied during the last decades for many engineering structures. The pore has a great influence on the permeability and on the material strength. The macroscopic mechanical behavior of porous material is strongly affected by its porosity which is a main property for the durability analysis. In order to account pore's effect, many micromechanical constitutive models have been proposed. Among these models, the most famous and extensively used one is proposed by Gurson (1977). In the framework of kinematical limit analysis theory, a macroscopic criterion was delivered in Gurson (1977) for a von Mises material containing a spherical or cylindrical void with a uniform macroscopic strain rate boundary condition. This most widely used criterion takes into account the porosity f of porous material and improves significantly the phenomenological ones. Based on this pioneering work, a huge number of extensions has been proposed: Introducing heuristic parameters to improve the Gurson's criterion (Leblond et al. (1994); Tvergaard (1981, 1982)); changing the incompressible von Mises type matrix to a compressible one (Drucker-prager type matrix: Guo et al. (2008); Jeong (2002); Maghous et al. (2009); Mises-Schleicher type matrix: Durban et al. (2010); Lee and Oung (2000); Monchiet and Bonnet (2012); Shen et al. (2015b); Green type matrix: Shen et al. (2014a,b, 2013a, 2012a)); considering the void shape from sphere to spheroid (Garajeu and

Suquet (1997); Gologanu et al. (1993, 1994, 1997); Keralavarma and Benzerga (2010); Monchiet et al. (2014); Pardoen (2003); Shen et al. (2011)); taking into account the tension-compression asymmetry and the anisotropy of the matrix (Benzerga et al. (1999); Cazacu and Stewart (2009); Monchiet et al. (2008)). Meanwhile, some criteria have been established for a porous ductile material with von Mises type matrix (Michel and Suquet (1992); Ponte Castaneda (1991); Sun and Wang (1989),etc.) by using variational techniques. Recently, a quasi-lower bound is proposed in Cheng et al. (2014) with a stress variational homogenization and improved by Shen et al. (2015a) by adopting a fully statically admissible microscopic stress field.

In order to establish a macroscopic criterion, a unit-cell is usually necessary to present the studied porous material. For example, a hollow sphere subjected to a uniform macroscopic strain rate boundary condition is studied in the famous Gurson's model. For porous medium with spheroidal void, a spheroidal volume containing a confocal spheroidal void is considered. With the homogenization procedure, the effect of porosity on the effective yield surface of porous materials can be explicitly taken into account, but the influences of interactions between voids and other microstructure informations (void shapes, sizes, orientation and distribution, etc.) are not so easy to be considered simultaneously in a criterion. Numerical studies is an efficient approach to solve this problem. Concerning the three-dimensional computational homogenization for porous medium with multiple voids, the effective behaviors of ductile metals containing spherical voids are studied in Fritzen et al. (2012) on a computational basis. According to the computational results, the GTN model was extended. A computational homogenization study was carried out in Khdir et al. (2015) for the overall yield surface of random porous medium. The influence of pore clustering onto the macroscopic material response has been investigated in Bilger et al. (2005) by using the Fast Fourier Transformation (FFT). The FFT method, different from the FEM, does not require the process of meshing. By discretizing the studied heterogeneous material into a series of grid points, the FFT approach is able to efficiently describe non-regular geometrical forms of complex microstructure. Different mechanical properties can be assigned on each point according to its location inside the heterogeneous microstructure. The overall responses at the macroscopic scale are then obtained by the volumetric average on the unit cell of the local stress and strain fields at the microscopic scale (Hill, 1963; Li and Wang, 2008). This mathematical technique was successfully applied by Moulinec and Suquet (1994, 1998) as an alternative approach of the finite element

method to compute the effective properties of composite materials with a periodic microstructure. This approach was further improved by an accelerated scheme to improve its computational efficiency (Eyre and Milton, 1999; Michel et al., 1999, 2000) and to extend its ability to voids and rigid inclusions (Michel et al., 2001).

In this work, we propose to apply a numerical method based on the Fast Fourier Transform to analyse the effect of microstructure (void shapes, sizes, orientations and distributions,etc.) on the effective behaviors of random porous geomaterials. This chapter is organized as follows: Using the FFT based numerical method, a compressible matrix with one spherical or ellipsoidal void is firstly studied to consider the effect of void shape on the overall behavior of porous geomaterial. More complex microstructures will be consider later to show the influence of void sizes, orientations and distributions. Then a simple damage model will be proposed to describe the material softening behavior due to induced damage process and its evolution.

5.2 FFT based numerical method and the FEM solution

The pores in porous geomaterial are very complex and its shapes are irregular. In order to obtain a closed-form expression of the macroscopic criterion to describe the effective behavior of porous material, the pore shapes are mostly assumed to be spherical or spheroidal in the homogenization methods. The R.V.E. are usually schematized as a hollow sphere or a spheroidal volume containing a confocal spheroidal void to take into account the porosity effect. The pore interaction, orientation and distribution are difficult to be considered in the explicit macroscopic criterion. By using FFT based numerical method presented in Chapter 2, this shortcoming can be overcame simply. The complex microstructure of the porous material can be fully accounted from the experimental image. Based on the Chapter 2 and 3, a comparison between the full field simulation of the FFT method and FEM solution will be provided.

The FFT based method does not require meshing the microstructure but discritizing the unit cell into $N \times N \times N$ regular simple of 3D voxels. The specific material properties according to their positions will be assigned to represent the real structures. In this comparison, the porous material is represented as a cubic unit cell containing a centered spherical pore. Two typical porosity will be considered. The discritization of the 3D unit cell with $128 \times 128 \times 128$ regular voxels are utilized for

FFT based method (5.1-b). For the FEM mesh, 7300 elements and 8886 nodes are used (5.1-a) with a refinement of spherical surface.

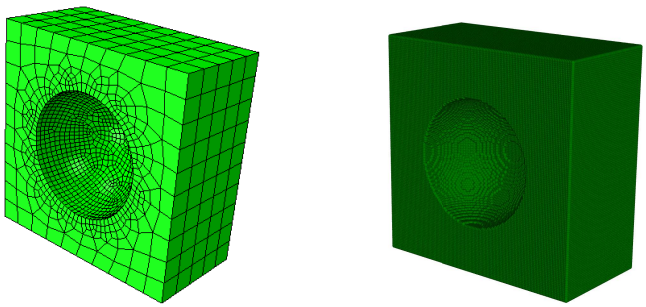

(a) (b)

Fig. 5.1 Microstructure with one spherical void (half display to show the pore inside) with a porosity $f = 10\%$: (a) FEM mesh with refinement for spherical surface; (b) FFT discritization with regular $128 \times 128 \times 128$ voxels.

The solid matrix is characterized by von Mises criterion with an isotropic plastic hardening:

$$f = \sigma_{eq} - (\sigma_0 + H\gamma^m) = 0 \tag{5.1}$$

where σ_0 and H are the initial yield stress and hardening modulus, respectively. σ_{eq} denotes the equivalent stress and computed as $\sigma_{eq} = (\frac{3}{2}\boldsymbol{s} : \boldsymbol{s})^{1/2}$. $\boldsymbol{s}$ is the deviatoric part of the stress $\boldsymbol{\sigma}$. The plastic variable γ is determined by an associated plastic flow rule:

$$\dot{\boldsymbol{\varepsilon}}^p = \dot{\lambda}\frac{\partial f}{\partial \boldsymbol{\sigma}} = \frac{3}{2}\dot{\gamma}\frac{\boldsymbol{s}}{\sigma_{eq}}, \qquad \dot{\gamma} = \dot{\lambda}. \tag{5.2}$$

The material parameters for the two simulations are the same and given in Tab. 5.1.

Table 5.1 Plastic parameters of the solid matrix

$E(GPa)$	ν	$\sigma_0(MPa)$	$H(MPa)$	m
10.0	0.25	45.0	150.0	0.5

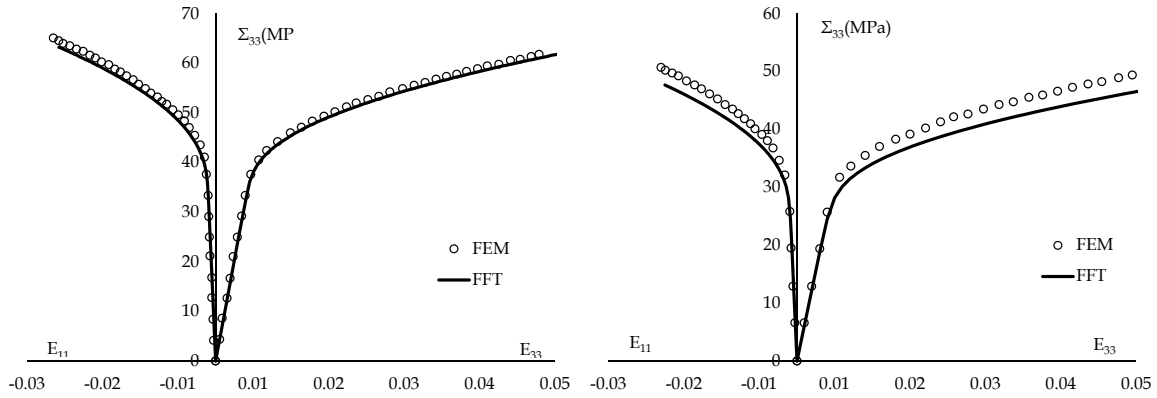

(a) $f = 10\%$ **(b)** $f = 25\%$

Fig. 5.2 Numerical simulations of macroscopic response of porous materials with the FFT method and FEM method.

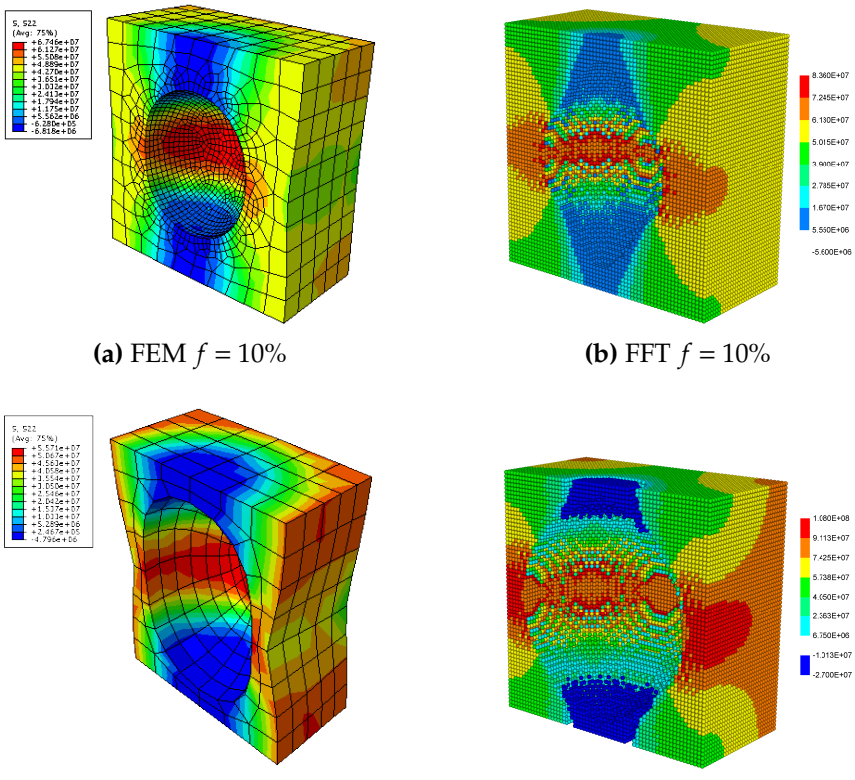

(a) FEM $f = 10\%$ **(b)** FFT $f = 10\%$

(c) FEM $f = 25\%$ **(d)** FFT $f = 25\%$

Fig. 5.3 Microstress distribution along loading path of porous materials with the FFT method and FEM method for two values of porosity.

A uniaxial tension test is applied and the numerical comparison of stress-strain

curve between the two methods is illustrated in Fig. 5.2 for $f = 10\%$ and $f = 25\%$. It is noted that the prediction of the FFT method is consistent with the one of FEM solution. The microscopic distributions of stress along the loading path for both FEM solution and FFT method are compared in Fig. 5.3. It can be seen that the the FFT method produces the local plastic distributions of porous materials nearly uniform with the FEM solution.

5.3 Influences of microstructure on the effective behavior of porous material

The advantage of the FFT-based numerical micro-mechanical model is the ability to investigate different kinds of porous geometry and distribution. Based on the validation of the FFT method, the influences of microstructure on the macroscopic behaviors of porous material are studied in this subsection. The shape, orientation, distribution and number of pores will be considered. A compressible Drucker-Prager type matrix with a non-associated plastic flow rule is used for the purpose of further study on geomaterials. The plastic criterion ϕ and plastic flow rule G take the following forms:

$$\begin{aligned} \phi &= \alpha\sigma_m + \sigma_{eq} - (\sigma_0 + H\gamma^m) \leqslant 0 \\ G &= \psi\sigma_m + \sigma_{eq} - (\sigma_0 + H\gamma^m) \end{aligned} \tag{5.3}$$

The same criterion and plastic potential have been used in (Jiang and Shao, 2012) to describe the macroscopic behaviors of the sandstone which is a typical geomaterial. The same elastic and plastic parameters of the matrix will be adopted to study the influence of the microstructure. These values are given in Tab. 5.2:

Table 5.2 Plastic parameters of the compressible matrix

$E(GPa)$	ν	$\sigma_0(MPa)$	$H(MPa)$	m	α	ψ
28.0	0.385	8.0	180.0	0.25	1.2	0.6

This elastoplastic model and the material parameters will be used in the following computational examples where the unit cell is subjected to a uniaxial compres-

sion along its 3rd axis and the prescribed macroscopic strains $\boldsymbol{E}$ are:

$$E_{33} = \boldsymbol{E} \qquad E_{11} = E_{22} = E_{12} = E_{13} = E_{23} = 0. \tag{5.4}$$

The volume fractions of the void (one or multiple) are all set to be $f = 10\%$.

In order to better show the influence of microstructure on the effective behavior of porous material, we start from the compressible matrix with one pore (spherical or ellipsoidal). After that, a compressible matrix with plenty of pores will be studied.

5.3.1 Compressible matrix with one pore

In this section, we consider firstly a compressible matrix obeying to the criterion in Eq. (5.3) with one pore. There is non interaction of pore. The influence of pore shape and orientation on the macroscopic behavior of the porous geomaterial with a porosity $f = 10\%$ will be taken into account by using the FFT based numerical method. The unit cell is discreted by a regular grid in 3 dimensions with spatical resolution $128 \times 128 \times 128$.

Effect of pore shape

A cubic cell with one pore is firstly generated to study the influence of pore shape. The initial microstructures are illustrated in Fig. 5.4 and three typical pore shapes are considered: sphere, oblate with a aspect ratio $Ar = 3$ and prolate with a aspect ratio $Ar = 2$. The orientation effect of oblate or prolate pore will be studied in the next part. With an uniaxial compression test, the comparison of the overall responses (stress-strain curve) of porous media with different pore shapes is shown in Fig. 5.5. It can be seen that the effective strength of the porous material with prolate void are slightly stiffer than the spherical one. Comparing with the spherical and prolate porous composite, the result for the oblate voided medium is much lower. In order to better analyse the reason, stress distributions at the microscopic scale are compared in Fig. 5.6 for these three cases. Fig. 5.6a illustrates the distributions of local stress σ_{33} for half of the spherical voided composite in three dimensional. Fig. 5.6b-5.6d are the local stress distributions in the middle section of the studied cubic cell. Stress concentration is clearly observed in the region (blue and purple color) perpendicular to the load direction (equatorial circle). On the contrary, the region (red color) along the load direction shows lower stress level comparing with the rest

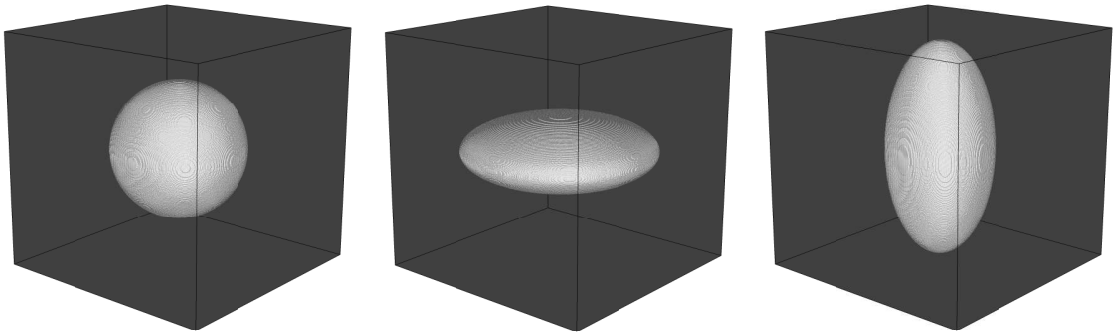

(a) sphere **(b)** oblate **(c)** prolate

Fig. 5.4 Microstructures used for the FFT simulation with different shapes of pore, volume fraction $f = 10\%$ (dark gray: solid matrix, white: pore). (aspect ratio: oblate $Ar = 3$ and prolate $Ar = 2$.)

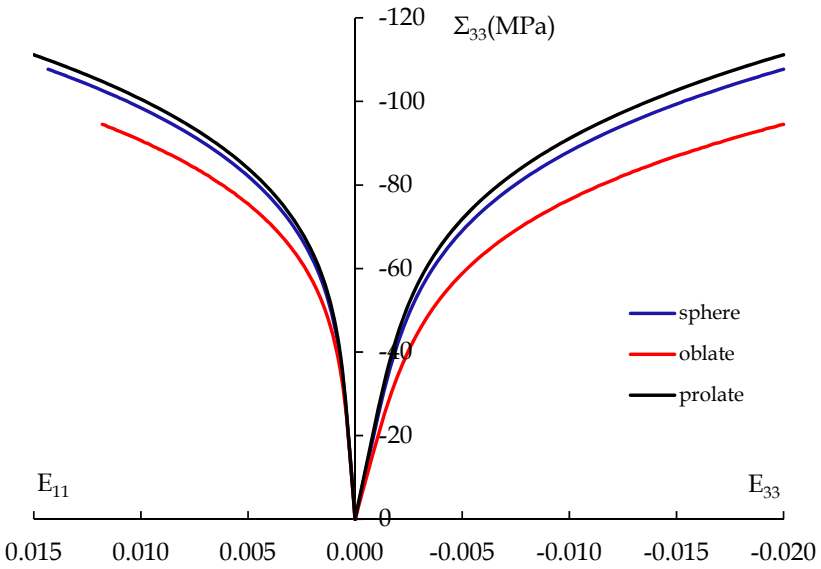

Fig. 5.5 Overall response of porous media with one spherical or ellipsoidal pore (see Fig. 5.4). Black line: prolate pore, blue line: spherical pore and red line: oblate pore.

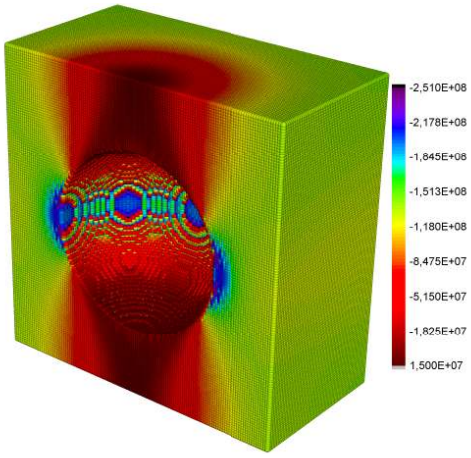

(a) spherical void

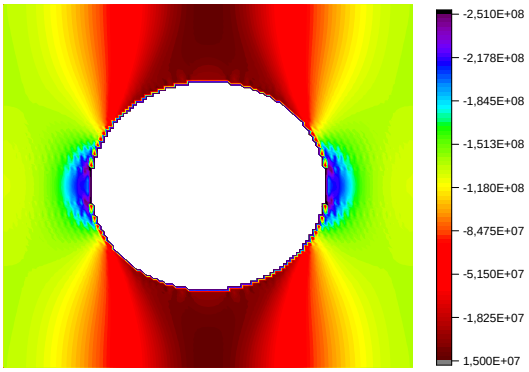

(b) spherical void

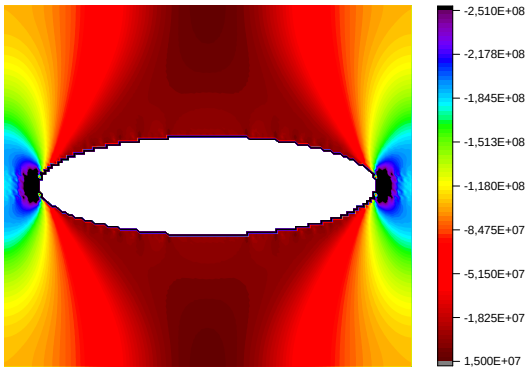

(c) oblate void

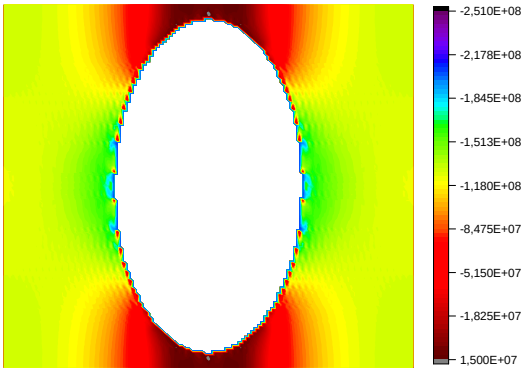

(d) prolate void

Fig. 5.6 Distributions of microscopic stress (σ_{33}) for different shapes of void. (a) spherical void in 3D; (b) spherical void in 2D; (c) oblate void in 2D; (d) prolate void in 2D.

of the matrix paste (green color). The same phenomenon is noticed for the prolate and oblate voids, however, the difference is the amount of stress concentration and the region with lower stress. It is noted that the region on the equatorial circle of the oblate pore has much more stress concentration but large amount of low stress region occurs on the perpendicular direction. Different from the oblate void, the prolate one induces less stress concentration as well as stress dispersion. For the spherical one the stress concentration and dispersion are both moderate. Therefore, considering the stress distribution on the whole field, the overall stress level is lowest for oblate void and highest for prolate. The observation is validated with the prediction of the overall strain stress curve shown in Fig. 5.5.

Effect of ellipsoidal pore orientation

Unlike the spherical pore, the influences of orientation on the macroscopic behavior should be considered for ellipsoidal pore. For the simplicity, a cubic cell having an oblate or prolate pore with different orientations (the angle between the major axis of the ellipsoid and the loading direction: $\theta = 0°, 45°, 90°$) will be considered for a same porosity $f = 10\%$ (see Fig. 5.8). The aspect ratio is the same as the one used in Fig. 5.4 for oblate or prolate pore. The comparisons of the overall responses (stress strain curve) for oblate or prolate pore with different orientations are shown in Fig. 5.7, respectively. It is noted that the highest strength is obtained for both oblate and prolate voided materials when the angle $\theta = 0°$. With $\theta = 90°$, lowest one is found. The influence of oblate void orientation on the effective behavior is larger than the impact of prolate void one. The microscopic stress distributions are shown in Fig. 5.8 in three dimension. Stress concentration (blue and purple color) is observed clearly at the boundary of the equatorial plane for all the cases. As the angle $\theta = 0°, 90°$, the stress distribution is symmetric with respect the 33 axis (vertical) while for the case of $\theta = 45°$ the stress distribution is symmetric alone the 45° degree axis. The stress distributions are therefore different with different microstructures. It is shown that the red region possesses lower stress comparing with the dominant matrix region and the amount of the region determines the overall stress level. It can be seen that for the oblate void, there is less stress concentration and less red region in the case of $\theta = 0°$. The one with $\theta = 90°$ holds much more red region comparing with other two cases. Therefore, it is clearly concluded that the case $\theta = 0°$ is much stiffer and the one $\theta = 90°$ is much softer. It is the same for the prolate pore, but it is noted that the difference of the red region for different angle is not as significant as the

oblate one. Therefore, the overall response for prolate void is the same trend but the difference is slight.

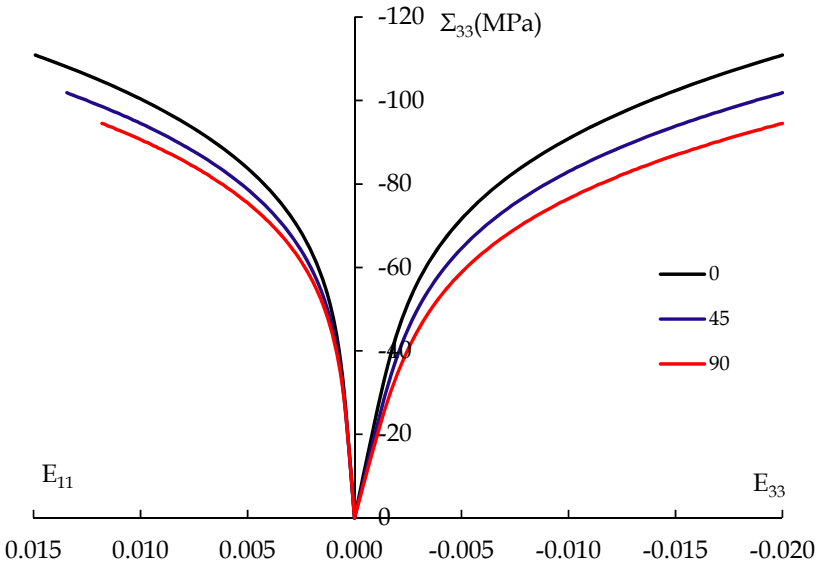

(a) One oblate void with different orientations

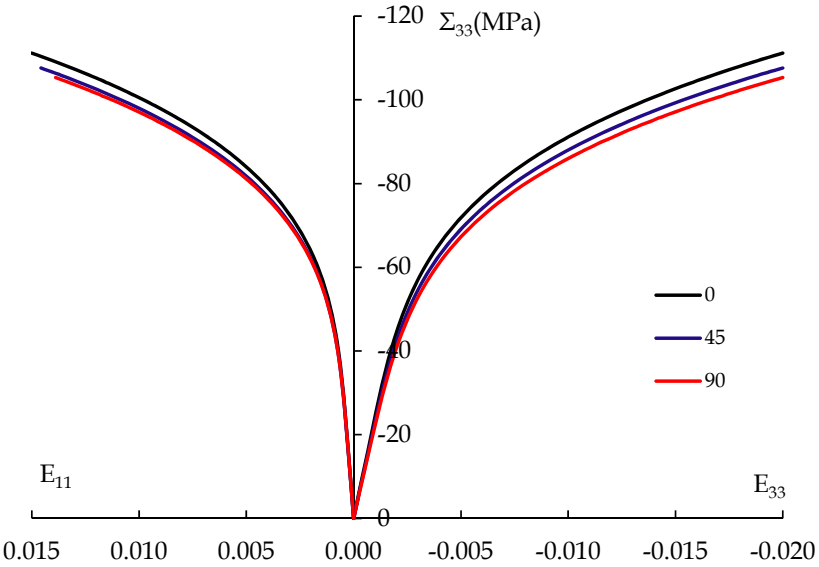

(b) One prolate void with different orientations

Fig. 5.7 Comparisons of stress strain curve of a porous material with one oriented oblate or prolate pore ($\theta = 0°, 45°, 90°$). (aspect ratio: oblate $Ar = 3$ and prolate $Ar = 2$)

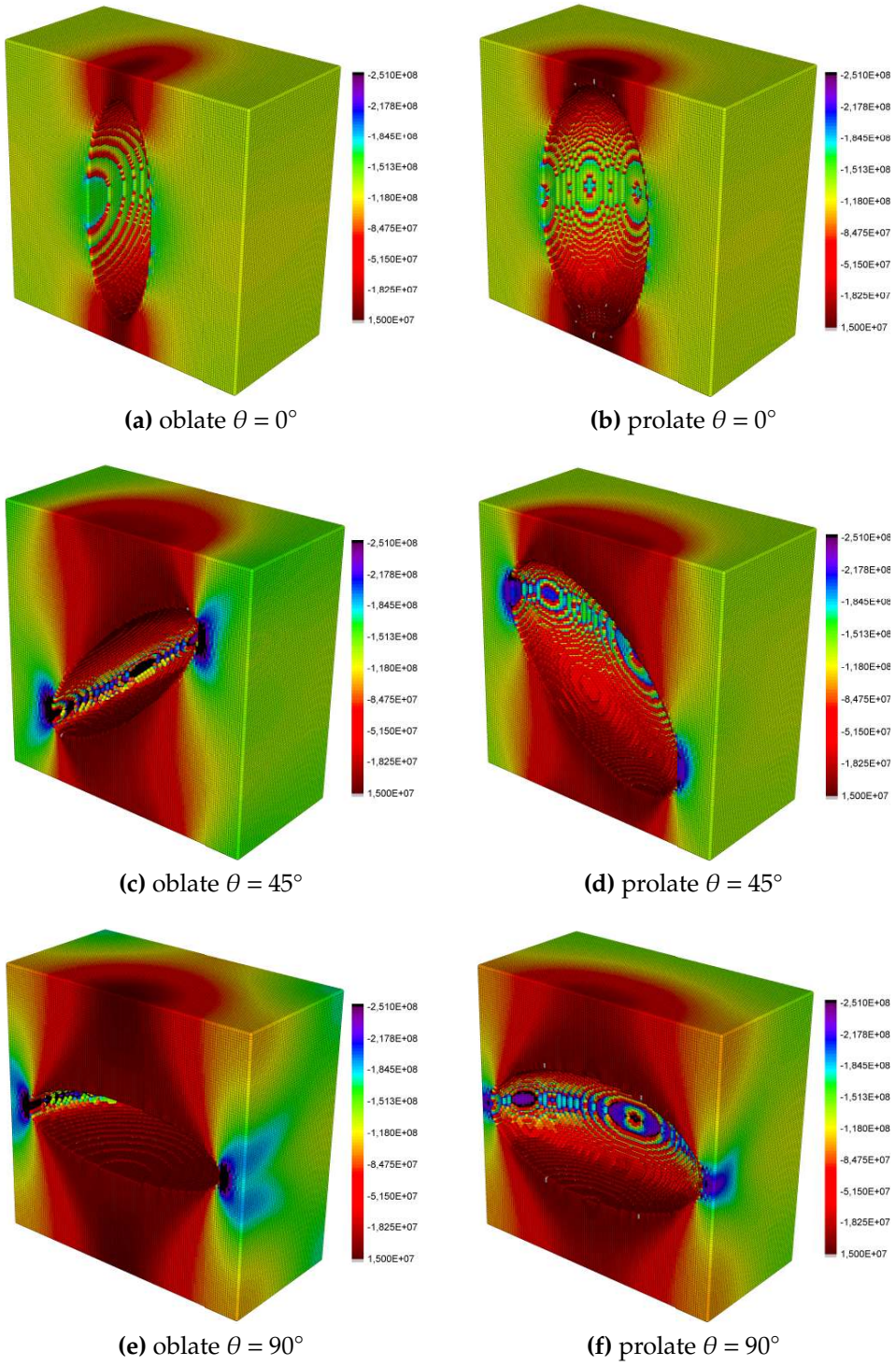

(a) oblate $\theta = 0°$ **(b)** prolate $\theta = 0°$

(c) oblate $\theta = 45°$ **(d)** prolate $\theta = 45°$

(e) oblate $\theta = 90°$ **(f)** prolate $\theta = 90°$

Fig. 5.8 Distribution of microstress σ_{33} in the cubic cell having a oblate or prolate pore with different orientations θ. (aspect ratio: oblate $Ar = 3$ and prolate $Ar = 2$).

5.3.2 Compressible matrix with plenty of pores

In porous materials, specially for porous geomaterials, the type and the distribution of pores are very complex. In the representative volume element, different shapes, sizes, orientations may exist simultaneously. Based on the above section for one pore, a cubic cell contains plenty of pores will be studied in this section to consider these effects on the overall behavior by using FFT based numerical method.

Randomly oriented distributed pores

For a general case, we will firstly consider a porous material containing randomly oriented distributed pores. By using the technique presented in Chapter 3, the generated microstructure are illustrated in Fig.5.9 with a same porosity $f = 10\%$: Fig.5.9a shows a cubic cell with randomly distributed spherical pores having the the same radius; the randomly oriented distributed ellipsoidal pores are illustrated in Fig.5.9b and Fig.5.9c, for case of oblate voids and prolate ones both with aspect ratio $Ar = 3$. In each case, the number of pores is 40.

The effects of the randomly distributed pores on the overall behavior is studied in this subsection with the same numerical model. The comparison of the effective properties (stress strain curve) for different microstructures on the overall behavior is shown in Fig. 5.10 (dashed line). It can be seen that the porous composite containing randomly distributed prolate voids with same aspect ration provides the highest response while the oblate the lowest. Comparing with the case of the cubic cell having one pore (solid line) with the same porosity, an evident difference is found in Fig.5.10. The microscopic stress distributions are shown in Fig. 5.11 in three dimension and two dimension. The location of the section Fig.5.11b-5.11d in the cubic cell is shown in Fig. 5.11a. Considering one void, the stress concentration is observed at the horizontal side of the void (blue and purple color) and lower stress region at the vertical side (red color). The interactions between the nearby pores are clearly shown.

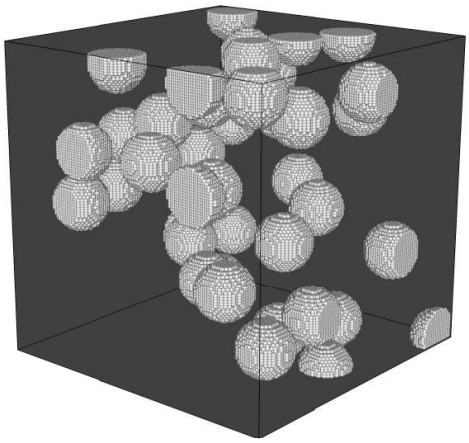

(a) sphere void

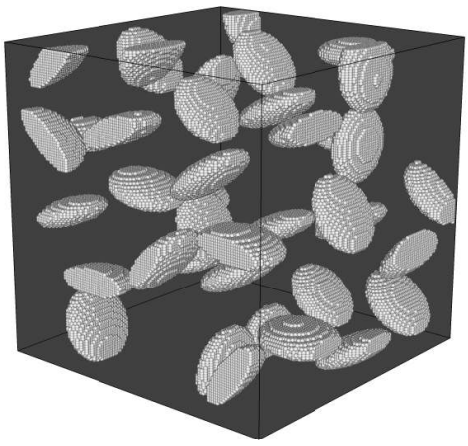

(b) oblate void

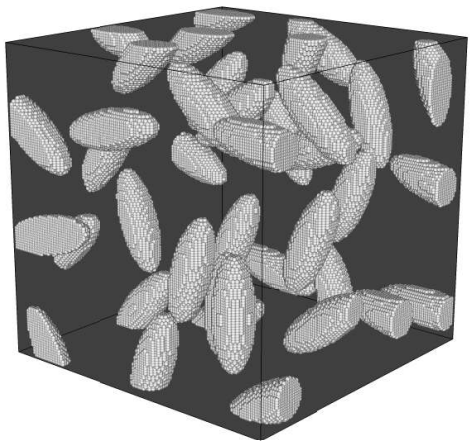

(c) prolate void

Fig. 5.9 Microstructures with randomly oriented distributed pores. Aspect ratio: oblate and prolate $Ar = 3$.

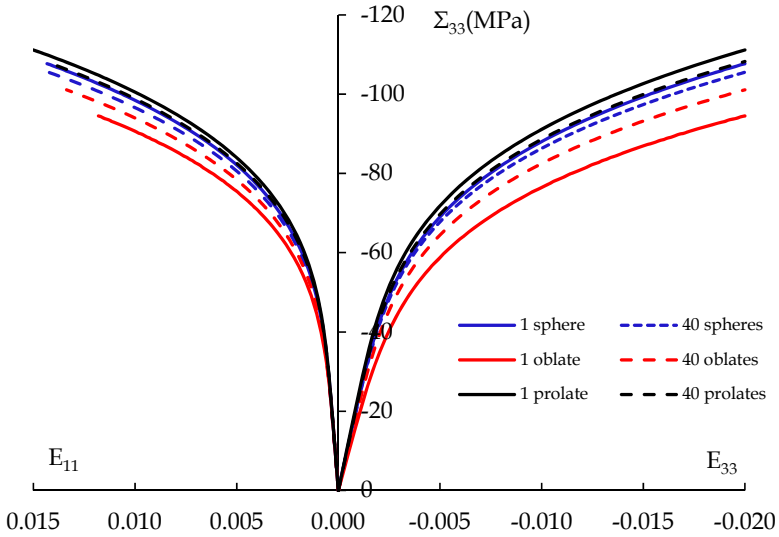

Fig. 5.10 Comparisons of stress strain curve for porous materials with randomly oriented distributed voids: solid line: microstructure in Fig5.4; dashed line: microstructure in Fig5.9

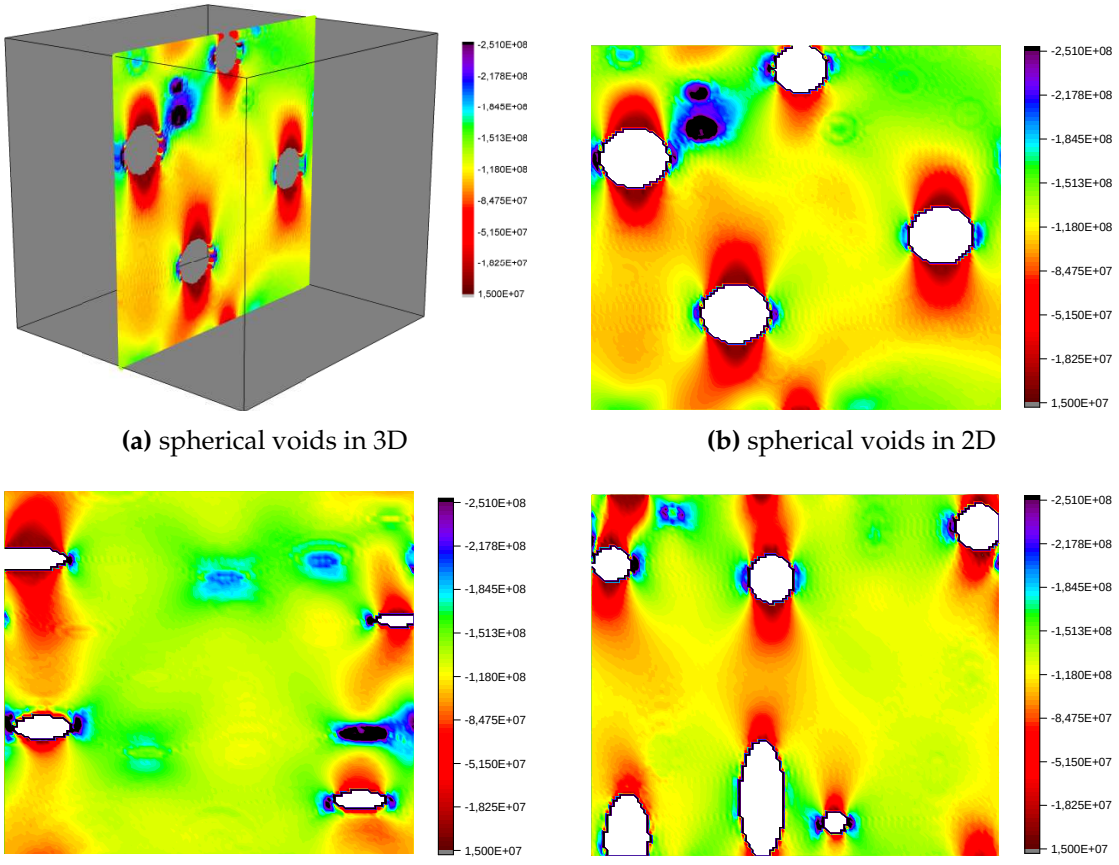

(a) spherical voids in 3D

(b) spherical voids in 2D

(c) oblate voids

(d) prolate voids

Fig. 5.11 Distributions of microscopic stress σ_{33} for different randomly distributed voids.

Uniformly oriented ellipsoidal pores

Due to the history of generation, some geomaterials may have uniform direction of pores which makes the composite being anisotropic. Fig.5.12 illustrates the microstructures having 40 randomly distributed ellipsoidal pores with uniform orientation with respect to the load direction. Three typical angles are considered: $\theta = 0°, 45°, 90°$. All the pores have the same aspect ratio. In order to study the effects of orientations, the same numerical model and loading condition are implemented on those microstructures with material properties stated above. The computational results are shown in Fig.5.13 for oblate and prolate voids, respectively. It is shown that the microstructures with uniform directions exhibit a very different overall response for different void directions. It is indicated that the microstructure with $\theta = 0°$ provides much stiffer effective properties, and the one with $\theta = 90°$ obtains much softer overall response comparing with the other two cases. The numerical simulations show clearly that the effective strength of the anisotropic composite is highly path dependent. The microscopic stress distribution is illustrated in Fig. 5.14 for both oblate and prolate voids with the three angles. The stress concentration is quite the same as the analysis for the previous examples, and the amount of the red region determines the overall response. It is clearly indicated that the microstructure with $\theta = 90°$ has much more red region, and $\theta = 45°$ is the next. It is also noted that the amount for the oblate one is significant. The observation on the microscopic scale provides a way to analyze the macroscopic behavior and makes the results be physically explained.

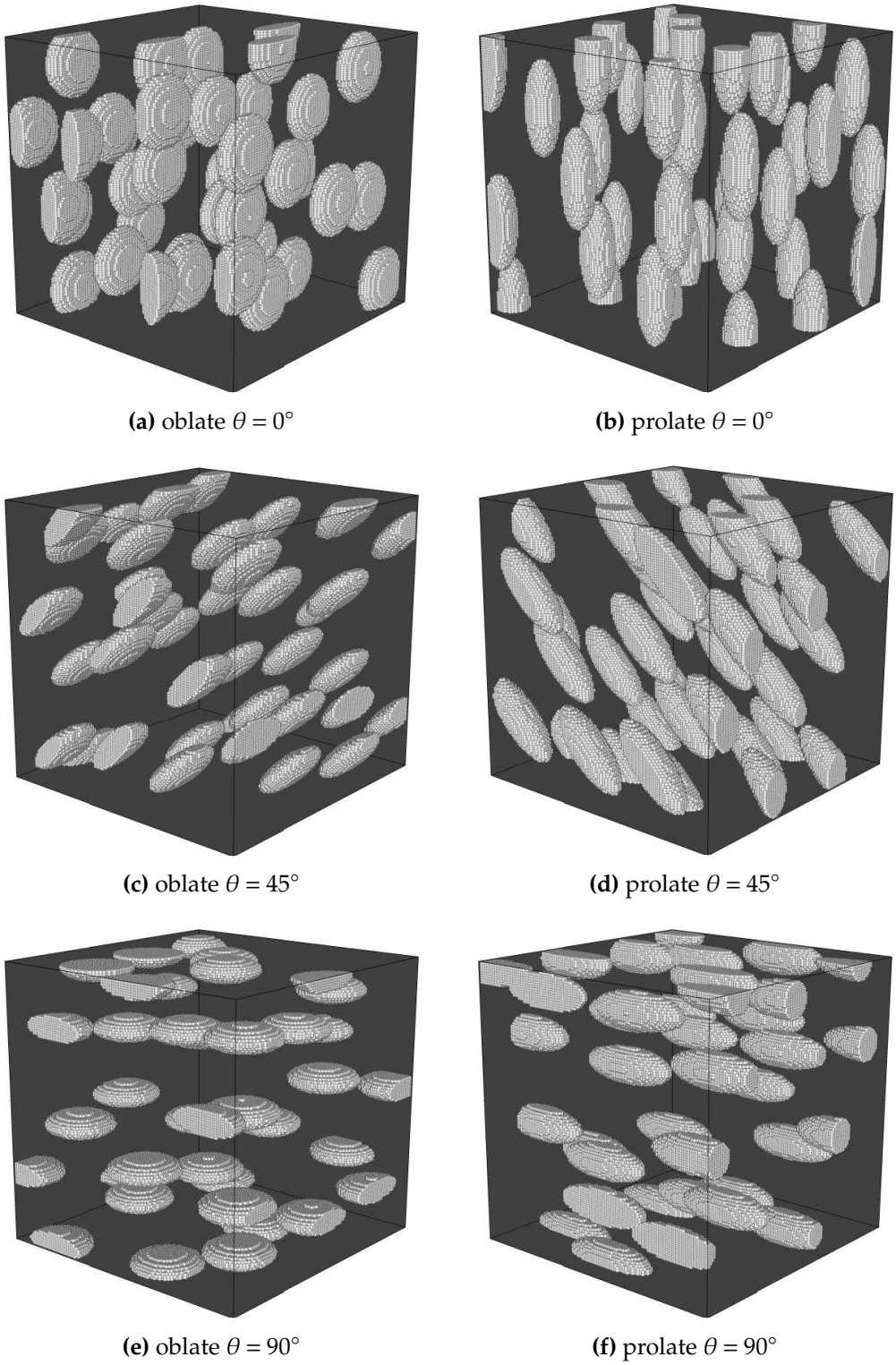

(a) oblate $\theta = 0°$ **(b)** prolate $\theta = 0°$

(c) oblate $\theta = 45°$ **(d)** prolate $\theta = 45°$

(e) oblate $\theta = 90°$ **(f)** prolate $\theta = 90°$

Fig. 5.12 Microstructure having randomly distributed ellpsoidal pores with uniform orientation.

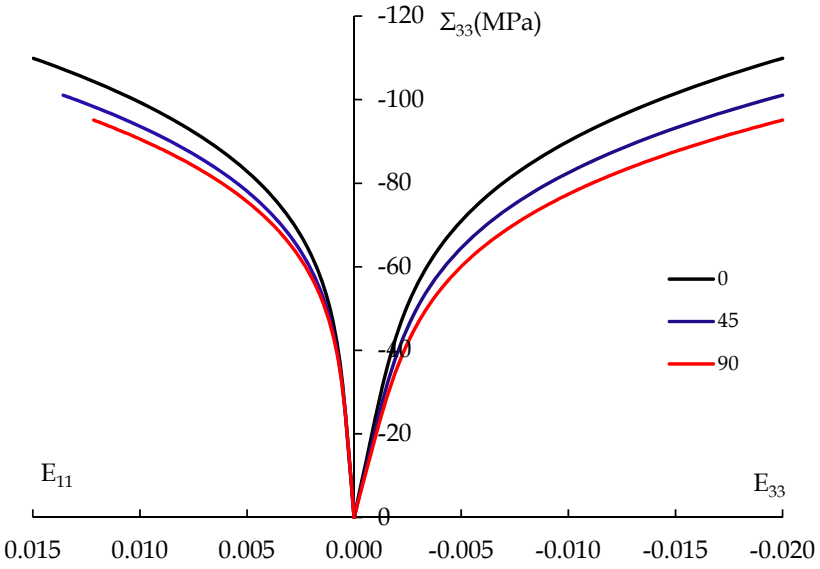

(a) uniform oblates

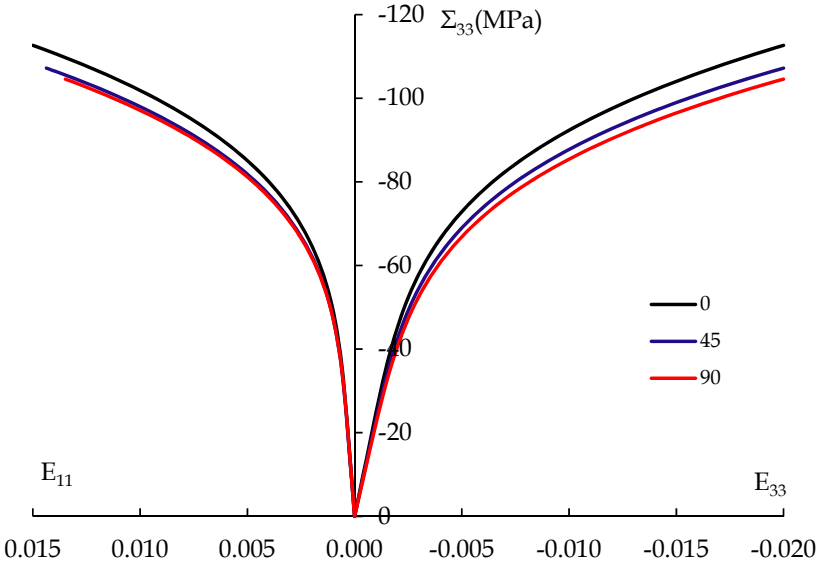

(b) uniform prolates

Fig. 5.13 Effective response predicted by the FFT method for uniform oriented oblate and prolate voids (see Fig5.12).

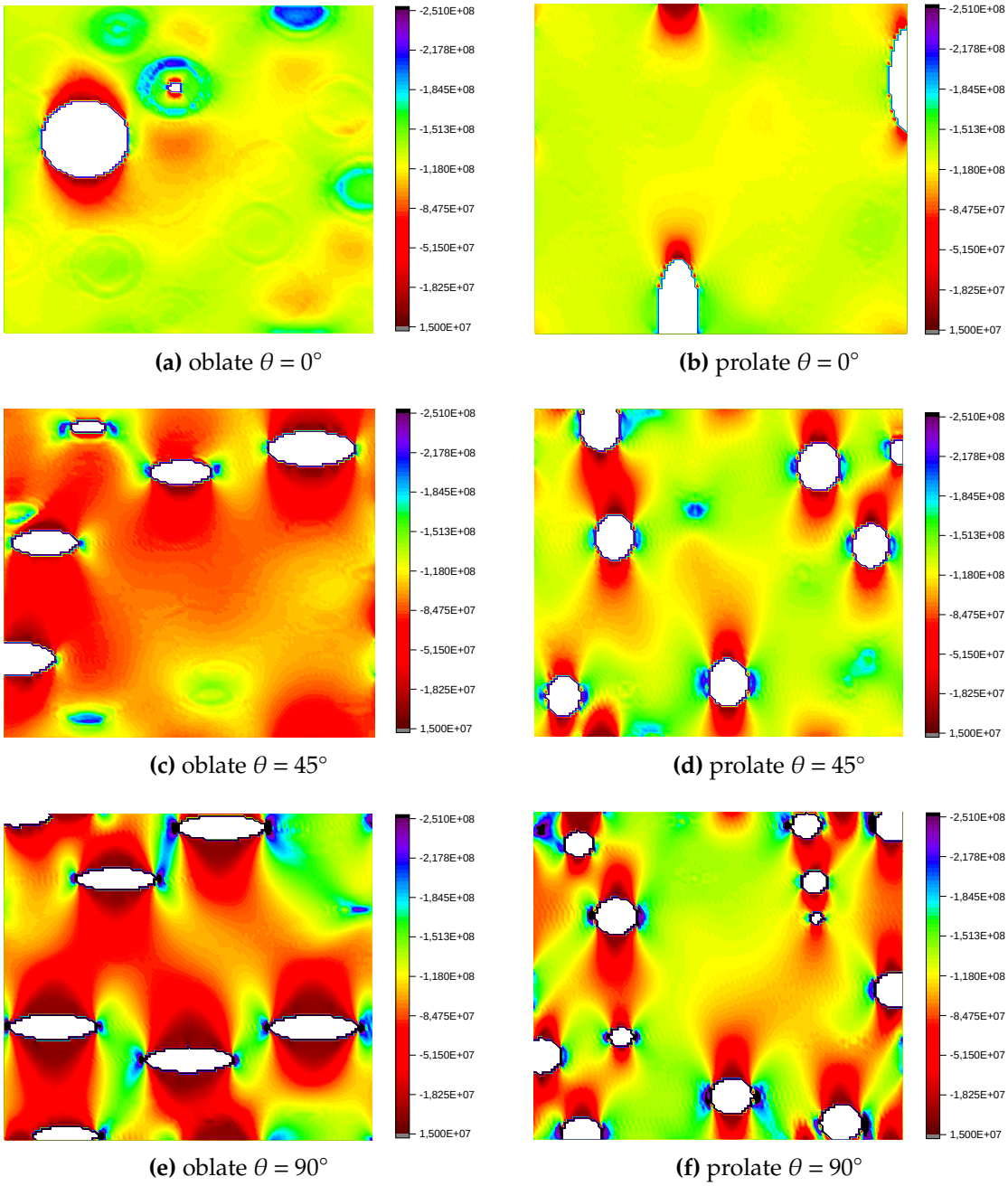

(a) oblate $\theta = 0°$ **(b)** prolate $\theta = 0°$

(c) oblate $\theta = 45°$ **(d)** prolate $\theta = 45°$

(e) oblate $\theta = 90°$ **(f)** prolate $\theta = 90°$

Fig. 5.14 Distributions of microscopic stress for randomly distributed ellipsoidal pores with uniform orientation.

5.4 Application to a sandstone

After the consideration of the pore effects, the FFT based numerical model is then applied to simulate a so-called "Vosges sandstone" geomaterials. This geomaterial has been studied in the (Jiang and Shao, 2012) by using FFT based method. In this study, a more reasonable R.E.V. will be considered. The FFT based numerical model is then extended to consider the damage with a plastic softening process. At the last part, the evolution of pores is investigated by taking into account the material degradation and propagation induced by the high plastic deformation.

5.4.1 Elastoplastic models of sandstone

The sandstone is a typical porous quasi-brittle rock with a porosity $f = 20\%$. A non-associated Druker-Prager model is proposed in (Jiang and Shao, 2012) to characterize the mechanical behaviors of the solid matrix. The plastic criterion ϕ and flow rule G coupled with the material parameters are given by:

$$\begin{aligned} \phi &= \alpha\sigma_m + \sigma_{eq} - R(\gamma) \leqslant 0 \\ G &= \psi\sigma_m + \sigma_{eq} - R(\gamma) \quad , \\ R(\gamma) &= \sigma_0 + H\gamma^m \end{aligned} \tag{5.5}$$

The elastic de plastic parameters are recalled in the following table:

Table 5.3 Plastic parameters of the compressible matrix

$E(GPa)$	ν	$\sigma_0(MPa)$	$H(MPa)$	m	α	ψ
28.0	0.385	8.0	180.0	0.25	1.2	0.6

The representative volume element used in (Jiang and Shao, 2012) is a cubic cell with one spherical void in the center and eight $\frac{1}{8}$ spherical one in the corner. As mentioned above, in reality, there are plenty of pores in the geomaterial sandstone. The R.V.E. of a cubic cell having randomly distributed spherical voids with a same porosity is used in this study. Adopting the same parameters rectified in (Jiang and Shao, 2012), the comparisons of these two numerical predictions and experimental data are shown in Fig. 5.15 with different confining pressures. Black lines denote the

results of (Jiang and Shao, 2012), the red ones present the predictions obtained in this study with a randomly distributed voids. It is noted that the macroscopic behavior is strongly effected by the microstructure with the same material parameters. The void size and distribution has a great influence.

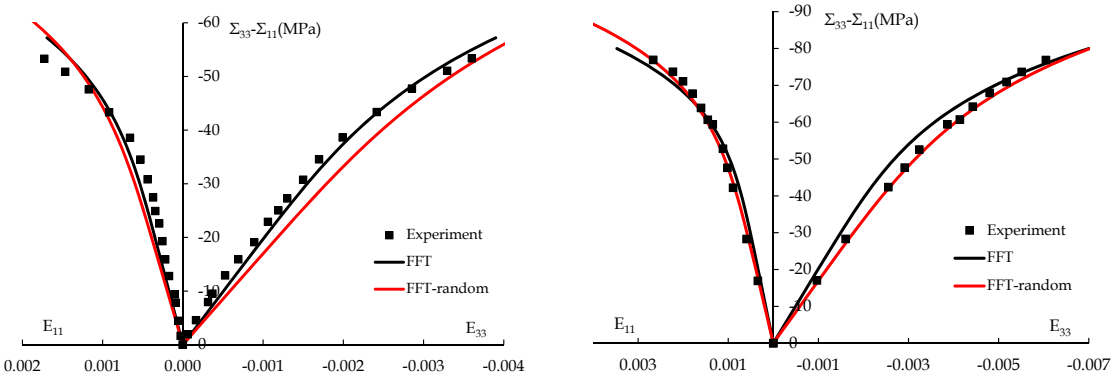

(a) 5MPa confining pressure **(b)** 10MPa confining pressure

(c) 20MPa confining pressure **(d)** 40MPa confining pressure

Fig. 5.15 Comparison of triaxial compression tests between numerical simulation and experiment of sandstone. Black solid line: results of (Jiang and Shao, 2012); red solid line: unit cell with randomly distributed pores; square dot: experimental data.

5.4.2 A simple damage model with plastic softening

With the increase of loading, the plastic deformation will accumulate. According to some microscopic analyses with digital image correlation technique, micro-cracks can initiate and propagate. The micro-cracking process affect the mechanical behaviors. In this section, we will propose a simple damage model to extend the work of (Jiang and Shao, 2012).

In order to account the damage induced in the matrix of the porous material, a plastic softening $S(\gamma)$ is introduced in the hardening $R(\gamma)$ in (5.5).

$$R(\gamma) = H \cdot S(\gamma) \cdot \gamma^m, \tag{5.6}$$

where γ is the accumulated plastic deformation in the solid matrix. The plastic softening $S(\gamma)$ is defined by:

$$S(\gamma) = 0.1 + e^{-(\frac{\gamma}{\eta})^n}, \tag{5.7}$$

in which η and n is the material parameters.

The FFT based was adapted to evaluate damage growth in porous materials with a plastic softening. The plastic criterion ϕ and non associated plastic flow rule G are given in (5.5). The numerical simulation follows the same material parameters used above. The new introduced parameter η depends on the confining pressure. The computational results are compared with the experimental data in Fig.5.16. It can be seen that the numerical results agree with the experimental data and predict a damage evolution to capture the main features of the mechanical behaviors of the studied porous geomaterials. This is a mathematical method to introduced the induced damage. A more physical damage model will be present later.

5.4.3 A damage model due to the pore evolution

As mentioned in the above section, micro cracks will generate in the porous material when the stress or plastic deformation exceed a critical value. The pores or cracks will grow and coalesce. Based on the elastoplastic model presented in 5.4.1, a FFT based damage model will be proposed by considering the pore evolution. The main advantage of the FFT based numerical approach is able to efficiently consider non-regular geometrical forms of microstructure. The heterogeneous material field is discretized into a series of grid points. Each point has a mechanical property according to its location in the heterogeneous microstructure. Taking advantage of these properties of FFT based approach, we assume that the point located in the solid matrix will lose its capability of supporting force when the accumulated plastic deformation γ in this point exceed a critical value ϵ_0.

$$\gamma \geq \epsilon_0, \tag{5.8}$$

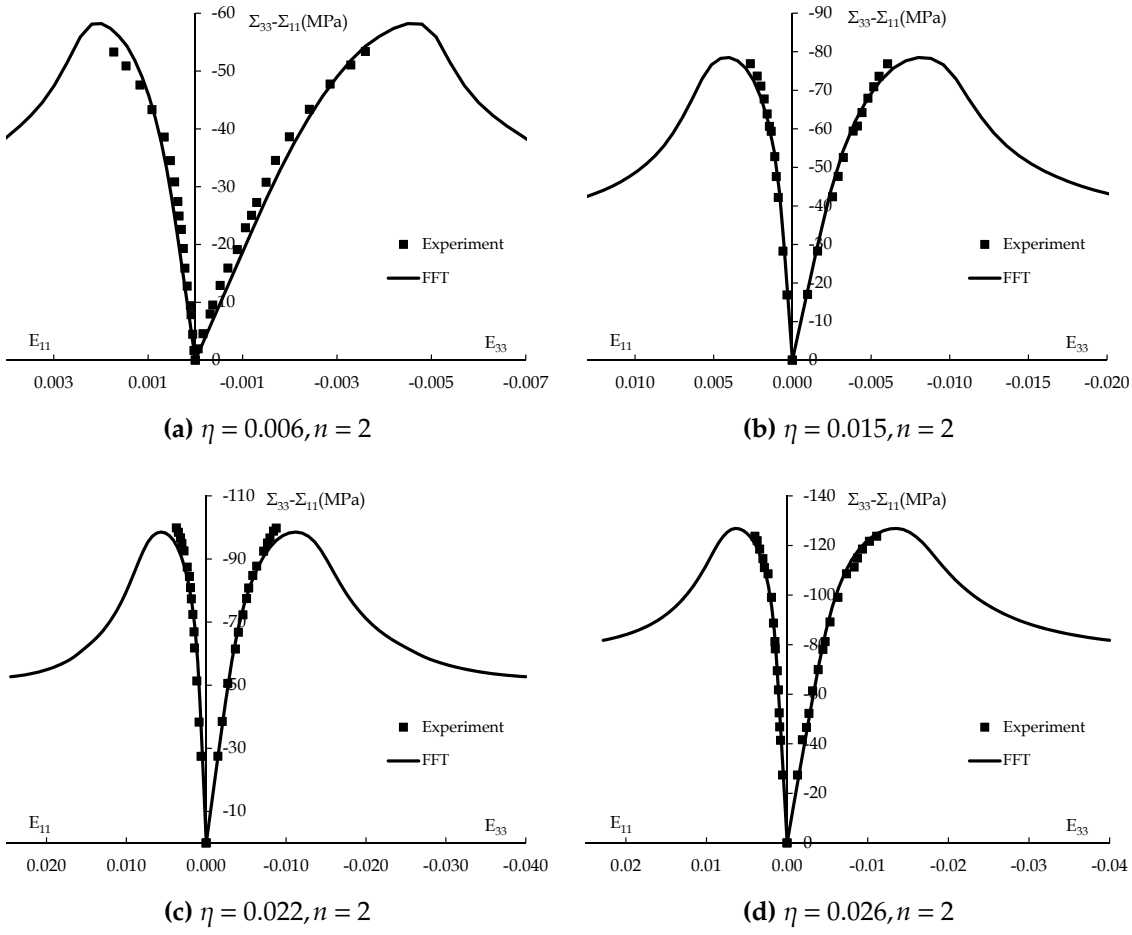

(a) $\eta = 0.006, n = 2$ **(b)** $\eta = 0.015, n = 2$

(c) $\eta = 0.022, n = 2$ **(d)** $\eta = 0.026, n = 2$

Fig. 5.16 Plastic softening predicted by the FFT method. (a) 5MPa confining pressure; (b) 10MPa confining pressure; (c) 20MPa confining pressure; (d) 40MPa confining pressure. Solid line: numerical prediction; square dot: experimental data.

That is to say, the properties in these points satisfying the condition (5.8) will be replaced by the ones of pore. This point becomes a pore. It is obvious that other more reasonable, more efficient and more realistic damage evolution laws exist for porous geomaterials. In the present study, the criterion (5.8) is adopted for simplicity. The growth and coalescence of pores are all controlled by this law during the compression tests. Different microstructure will be considered for the damage procedure.

- A cubic cell with a centered spherical pore

A cubic cell with a centered spherical pore is firstly simulated and the numerical results are compared with the experimental data in Fig. 5.17. The confining pressure changes the material properties. The critical values ϵ_0 changes with the confining pressure. It shows that the numerical results agree with the experimental data before the ultimate strength and then the pore evolution occurs. The macroscopic strength decreases slightly at the first stage but dramatically afterwards until the material is fully deteriorated.

- A cubic cell with plenty of spherical pores

The FFT method provides a powerful tool to analyze the microstructure evolution at the microscopic scale. In order to illustrate clearly the pore evolution in the microstructure and consider the effect of the interaction between the pores, a microstructure with plenty of pores are simulated in this subsection. A cubic cell with $N = 50$ randomly distributed spherical pores are generated in Fig.5.18-a with a porosity $f = 1\%$. The growth and coalescence of pores are illustrated for some representative stages in Fig. 5.18. Using the FFT based numerical method, the pore propagation and coalescence are clearly observed. It can be seen that the pore growth extensively developed at the primary stage and coalescence occurs only at the region with very close pores (see Fig. 5.18a and 5.18b). In the medium stage, the coalescence are largely developed at the space with a pore clustering, but not entirely connected (see Fig. 5.18c and 5.18d). At the final stage (see Fig. 5.18e and 5.18f), extensively coalescence takes place between different cluster of pores and different deteriorated regions are expands to the boundary of the unit cell. These connected damaged regions make the whole field being degraded. It is noted that the one pore far away from other cluster of ones remains single to grow and not effected by others. In short, from microscopic level, the pores increase slowly at the primary stage since only self-growth is developed. Later, coalescence takes place between different cluster of pores. Finally, the propagation and growth extensively

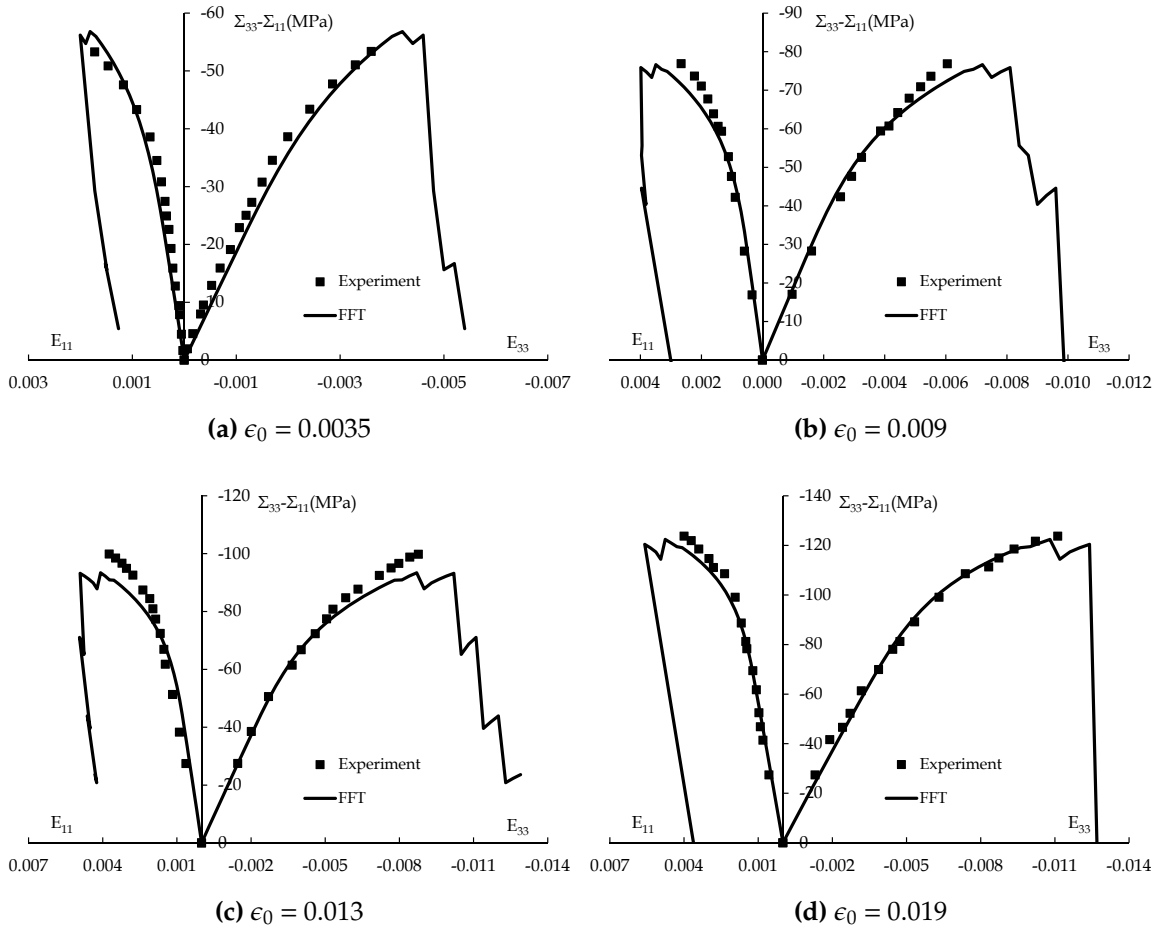

(a) $\epsilon_0 = 0.0035$ **(b)** $\epsilon_0 = 0.009$

(c) $\epsilon_0 = 0.013$ **(d)** $\epsilon_0 = 0.019$

Fig. 5.17 Stress strin curve predicted by FFT based damaged model with one centered spherical pore. (a) 5MPa confining pressure; (b) 10MPa confining pressure; (c) 20MPa confining pressure; (d) 40MPa confining pressure. Solid line: numerical prediction; square dot: experimental data.

occurs due to the connection between different deteriorated region. From the view of macroscopic scale, the overall response totally agrees with the microscopic analysis of physical mechanism. Therefore, the FFT based numerical method is not only an efficient numerical homogenization approach but also a powerful tool for micromechanical analysis for porous materials.

5.5 Closing remarks

In this chapter, the FFT based numerical method is applied to describe the macroscopic behavior of porous materials with a full field microscopic analysis. The generation of microsctructures for different void shapes and distributions are discussed. Firstly, the results predicted by FFT based method is compared with the FEM ones as the reference solution obtained by ABAQUS for a porous material with a centered pore. After the validation, the effects of the microstructures on the macroscopic behaviors of porous materials are investigated in details. Different microstructure are generated by numerical method. The influence of pores shape, size, distribution, orientation are studied and compared from macroscopic behavior and microscopic stress distributions. Then the proposed model is applied to describe the effective behavior of sandstone. Two microstructures (R.E.V.) of sandstone are studied: a cubic cell with a spherical cell in the center and eight $\frac{1}{8}$ spherical one in the corner; another one with randomly distributed pores with a same porosity. Comparing these two results with experimental data, the effect of pore interaction are shown clearly. Based on this elastoplastic model, a damage model is then introduced to simulate the material degradation. Taking advantage of the FFT based method, the induced damage due to the generated pore is clearly illustrated during the loading process at the microscopic level.

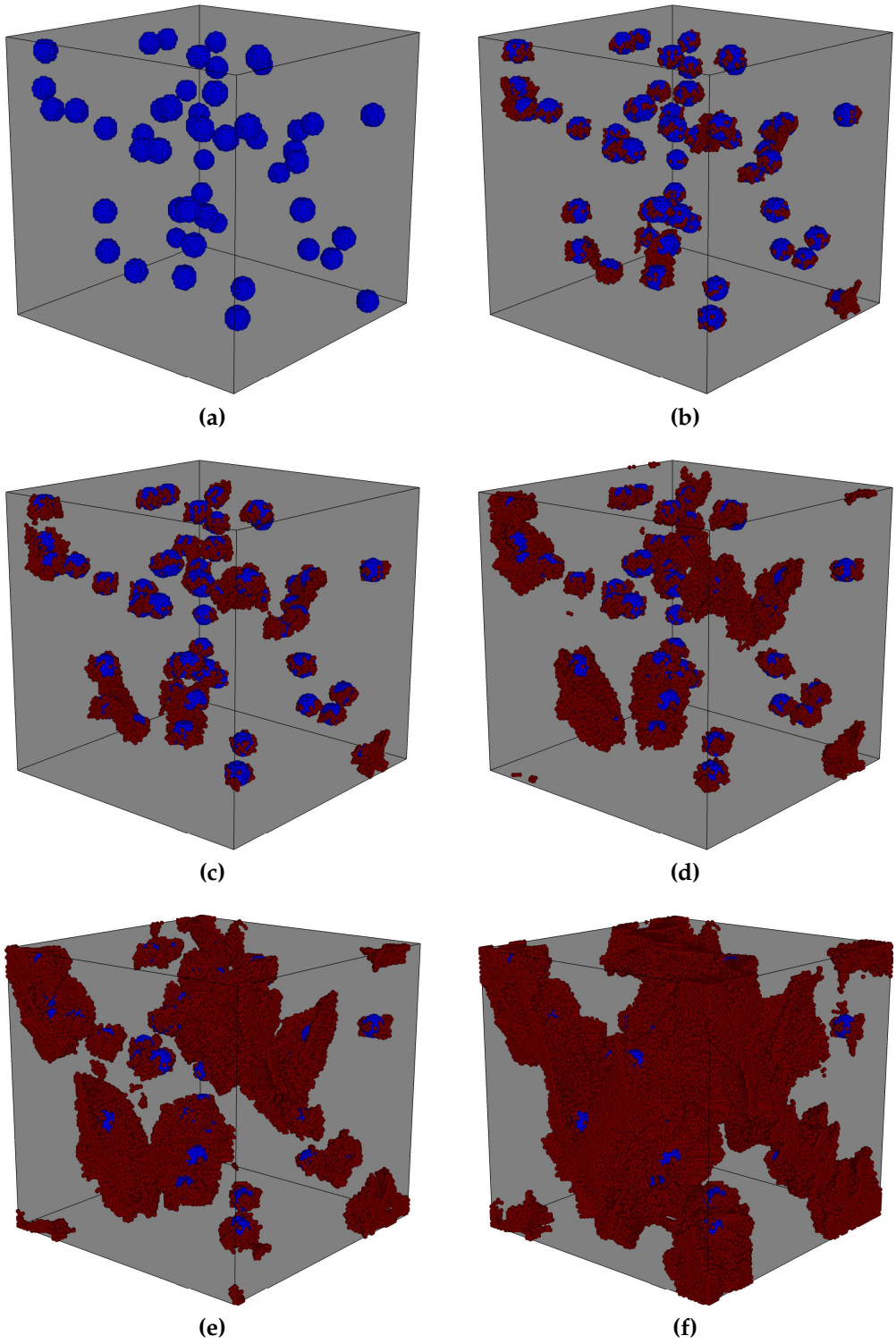

Fig. 5.18 Damage evolution in a microstructure having 50 randomly distributed pores with a porosity $f = 1\%$, predicted by the FFT method.

Chapter 6

Conclusions and future works

The objective of this thesis is to apply the numerical method based on Fast Fourier Transforms (FFT) to take into account the effects of microstructure on the macroscopic mechanical behaviors of heterogeneous composite materials. The procedure of discretizing unit cell into a set of grid voxels makes it possible to assign local constitutive equation for each voxel. Therefore, heterogeneous materials with irregular and complex microstructures can be simply simulated with suitable numerical models. The applications are performed to the matrix-inclusion type composite materials and porous media by considering the shapes, sizes, distributions and orientations of inclusions and pores.

At the preliminary stage of the research, the computational method was validated by some reference solutions from direct finite element method and the initial work of this method with the periodic unit cell problems. As a strain based scheme, the numerical approach showed a significant convergence-rate dependence on the phase contrast of composite materials. The computational program was firstly optimized to a parallel computing code by the open MPI library and the efficiency was highly improved. The microstructures generated by the FFT method was extended from matrix with one inclusion into more complex ones. For example, multiple inclusions with regular distributions and randomly distributions. The spherical shape is also extended into ellipsoidal one with random or uniform orientations. Meanwhile, different types of numerical models are developed for individual constituent phase, for example, perfectly elastic, elastoplastic with Von Mises, associated or non associated Drucker Prager criterion with isotropic hardening, and damage process.

With the previous preparations, the computational approach was firstly applied on matrix-inclusion type composites to investigate the effects of microstructure on

the effective mechanical behaviors. The influence of the shape, size, distributions and orientations were examined with the analysis at the microscopic scale.The microscopic distributions of stress and strain were fully display in two dimensional and three dimensional output figures. The overall strain stress relations for different cases are physically explained from the microscopic level, for example, the stress concentration on the material interfaces or boundaries, the interactions between different inclusions. With these investigations, the numerical method was then applied on a specific clayey rocks consisting of an elastoplastic matrix reinforced by perfectly elastic mineral inclusions. The effects of confining pressure and mineralogical compositions were taken into account and compared with experimental data. The progressive damage process was introduced to model microcrack around the mineral grains and to account the material softening behavior in the post-peak regime. The comparison with experimental data verified the efficiency and accuracy of the FFT based method.

In the last part, the strain-based FFT method was applied on the porous geomaterials with a specific application on the mechanical behaviors of sandstone. The study is devoted to analyse the effect of microstructure (void shapes, sizes, orientations and distributions,etc.) on the effective behaviors of random porous geomaterials. A pressure sensitive non associated Drucker Prager criterion was proposed on the solid matrix. The effects of one spherical or ellipsoidal void was firstly studied and then extended into more complex structure with randomly oriented distributed pores. With the comparison between the experimental data of sandstone, the pore evolution was investigated by introducing a damage process with material softening. A simple damage criterion was proposed to simulate pore evolution of microstructure by taking into account the deteriorate around the pores and the interacted regions. A three dimensional full field analysis was exhibited to show the pore growth and the deteriorate process of the microstructure.

During the research, the FFT method exhibited high efficiency and accuracy in many respects, however, numerical improvements are still open to discuss in future work. Except the accelerated scheme, discretizing microstructure with adaptable grid of points will dramatically reduce the computational costs and increase the efficiency. For example, fine grid on the material boundaries and less grid on the uniform region. Furthermore, the feature of making directly use the image of real structure should be put more effort. On the other hand, further study should be considered on the porous material by taking into account the effects of complex

distributions of pores which is difficult for the analytical solution. Moreover, the future research is also recommended to other aspects, for example, crack propagation, interface debonding *etc*.

References

Abou-Chakra Guéry, A., Cormery, F., Shao, J. F., and Kondo, D. (2008). A micromechanical model of elastoplastic and damage behavior of a cohesive geomaterial. *International Journal of Solids and Structures*, 45:1406–1429.

Abou-Chakra Guéry, A., Cormery, F., Shao, J. F., and Kondo, D. (2009). A multiscale modeling of damage and time-dependent behavior of cohesive rocks. *International Journal for Numerical and Analytical Methods in Geomechanics*, 33:567–589.

Abou-Chakra Guéry, A., Cormery, F., Shao, J.-F., and Kondo, D. (2008). A micromechanical model of elastoplastic and damage behavior of a cohesive geomaterial. *Int.J.Solids Struct*, 45(5):1406–1429.

Aboudi, J., Arnold, S., and Vednarcyk, B. (2012). *Micromechanics of Composite Materials: A Generalized Multiscale Analysis Approach*. Elsevier, 1st edition edition.

Andra (2005). *Referentiel du site Meuse-Haute Marne*. Report, AAA.

Andra (2012). *Referentiel du comportement THM des formations sur le site de Meuse-Haute-Marne*. Report, D.RP.AMFS.12.0024.

Benzerga, A., Besson, J., and Pineau, A. (1999). Coalescence-controlled anisotropic ductile fracture. *J. Eng. Mater. Technol.*, 121:221–229.

Bikong, C., Hoxha, D., and Shao, J. (2015). A micro-macro model for time-dependent behavior of clayey rocks due to anisotropic propagation of microcracks. *International Journal of Plasticity*, 69:73–88.

Bilger, N., Auslender, F., Bornert, M., Michel, J. C., Moulinec, H., Suquet, P., and Zaoui, A. (2005). Effect of a nonuniform distribution of voids on the plastic response of voided materials: a computational and statistical analysis. *International Journal of Solids and Structures*, 42:517–538.

Bornert, M., Bretheau, T., and Gilormini, P. (2001). *Homogénéisation en mécanique des matériaux 1*. Hermes Science Publications.

Bornert, M., Vales, F., Gharbi, H., and Nguyen, M. D. (2010). Multiscale full-field strain measurements for micromechanical investigations of the hydromechanical behaviour of clayey rocks. *Strain*, 46:33–46.

Castañeda, P. P. (2005). *Heterogeneous materials. Lecture Notes*. Department of Mechanics, Ecole Polytechnique.

Cazacu, O. and Stewart, J. B. (2009). Analytic plastic potential for porous aggregates with matrix exhibiting tension-compression asymmetry. *Journal of the Mechanics and Physics of Solids*, 57:325–341.

Chaboche, J. L., Kanouté, P., and Roos, A. (2005). On the capabilities of mean-field approaches for the description of plasticity in metal matrix composites. *International Journal of Plasticity*, 21:1409–1434.

Cheng, L., De Saxce, G., and Kondo, D. (2014). A stress-based variational model for ductile porous materials. *International Journal of Plasticity*, 55:133–151.

Chiarelli, A.-S., Shao, J.-F., and Hoteil, N. (2003). Modeling of elastoplastic dammage behavior of a claystone. *Int.J.Plasticity*, 19:23–45.

Doghri, I. and Ouaar, A. (2003). Homogenization of two-phase elasto-plastic composite materials and structures. study of tangent operators, cyclic plasticity and numerical algorithms. *International Journal of Solids and Structures*, 40:1681–1712.

Durban, D., Cohen, T., and Hollander, Y. (2010). Plastic response ofporous solids with pressure sensitive matrix. *Mechanics Research Communications*, 37:636–641.

Dvorak, G. J. (1992). Transformation field analysis of inelastic composite materials. *Proceedings: Mathematical and Physical Sciences*, 473:311–327.

Dvorak, G. J. and Benveniste, Y. (1992). On transformation strains and uniform fields in multiphase elastic media. *Proceedings: Mathematical and Physical Sciences*, 437:291–310.

Eshelby, J. D. (1957). The determination of the elastic field of an ellipsoidal inclusion, and related problems. *Proceedings of the Royal Society of London*, 241(1226):376–396.

Eyre, D. J. and Milton, G. W. (1999). A fast numerical scheme for computing the response of composites using grid refinement. *The European Physical Journal Applied Physics*, 6:41–47.

Fritzen, F., Forest, S., Böhlke, T., Kondo, D., and Kanit, T. (2012). Computational homogenization of elasto-plastic porous metals. *International Journal of Plasticity*, 29:102–119.

Garajeu, M. and Suquet, P. (1997). Effective properties of porous ideally plastic or viscoplastic materials containing rigid particles. *J. Mech. Phys. Solids*, 45:873–902.

Gologanu, M., Leblond, J., and Devaux, J. (1993). Approximate models for ductiles metals containing non-spherical voids - case of axisymmetric prolate ellipsoidal cavities. *J. Mech. Phys. Solids*, 41(11):1723–1754.

Gologanu, M., Leblond, J., and Devaux, J. (1994). Approximate models for ductile metals containing non-spherical voids–cas of axisymmetric oblate ellipsoidal cavities. *ASME J.Eng. Mat. Tech.*, 116:290–297.

Gologanu, M., Leblond, J., Perrin, G., and Devaux, J. (Springer Verlag, New York 1997). Recent extensions of gurson's model for porous ductile metals. In: P.Suquet, Editor. *Continuum Micromechanics*, pages 61–130.

Guo, T., Faleskog, J., and Shih, C. (2008). Continuum modeling of a porous solid with pressure-sensitive dilatant matrix. *J.Mech.Phys.Solids*, 56:2188–2212.

Gurson, A. (1977). Continuum theory of ductile rupture by void nucleation and growth: part1-yield criteria and flow rules for porous ductile media. *J. Engrg. Mater. Technol.*, 99:2–15.

Hashin, Z. and Shtrikman, S. (1963). A variational approach to the theory of the elastic behavior of multiphase materials. *Journal of the Mechanics and Physics of Solids*, 11:127–140.

Hill, R. (1952). Elastic properties of reinforced solids: some theoretical principles. *Proceedings of the Physical Society*, A65:349–352.

Hill, R. (1963). Elastic properties of reinforced solids: some theoretical principles. *Journal of the Mechanics and Physics of Solids*, 11:357–372.

Hill, R. (1965). Continuum micro-mechanics of elastoplastic polycrystals. *Journal of the Mechanics and Physics of Solids*, 13:89–101.

Hoxha, D., Giraud, A., Homand, F., and Auvray, C. (2007). Saturated and unsaturated behaviour modelling of meuse haute marne argillite. *International Journal of Plasticity*, 23(5):733–766.

Huang, Y., Abou-Chakra-Guery, A., and Shao, J. (2015). Incremental variational approach for time dependent deformation in clayey. *International Journal of Plasticity*, 64:88–103.

Huang, Y. and Shao, J. (2013). A micromechanical analysis of time-dependent behavior based on subcritical damage in claystones. *Int. J. of Damage Mechanics*, 22:773–790.

Huang, Y., Shen, W., Shao, J., Abou-Chakra-Guery, A., and Jia, Y. (2014). Multiscale modelling of time-dependent behavior of claystones with a viscoplastic compressible porous matrix. *Mechanics of Materials*, 79:25–34.

Jeong, H. (2002). A new yield function and a hydrostatic stress-controlled model for porous solids with pressure-sensitive matrices. *Int. J. Solids Struct.*, 39:1385–1403.

Jiang, T., Abou-Chakra Guery, A., Kondo, D., and Shao, J. F. (2009). Multi-scale modeling for inelastic behavior of a cohesive geomaterial. *Mechanics Research Communications*, 36:673–681.

Jiang, T. and Shao, J. F. (2009). On the incremental approach for nonlinear homogenization of composite and influence of isotropization. *Computational Materials Science*, 46:447–451.

Jiang, T. and Shao, J. F. (2012). Micromechanical analysis of the nonlinear behavior of porous geomaterials based on the fast fourier transform. *Computers and Geotechnics*, 46:69–74.

Jiang, T. and Shao, J. F. (2013). A non-uniform transformation field analysis for frictional cohesive geomaterials. *European Journal of Mechanics-A/Solids*, 42:97–111.

Jiang, T., Shao, J. F., and Xu, W. Y. (2011). A micromechanical analysis of elastoplastic behavior of porous materials. *Mechanics Research Communications*, 38:437–442.

Kanouté, P., Boso, D., Chaboche, J., and Schrefler, B. (2009). Multiscale methods for composites: A review. *Archives of Computational Methods in Engineering*, 16:31–75.

Keralavarma, S. and Benzerga, A. (2010). A constitutive model for plastically anisotropic solids with non-spherical voids. *Journal of the Mechanics and Physics of Solids*, 58:874–901.

Khdir, Y.-K., Kanit, T., Zaïri, F., and Naït-Abdelaziz, M. (2015). A computational homogenization of random porous media: Effect of void shape and void content on the overall yield surface. *European Journal of Mechanics A/Solids*, 49:137–145.

Kröner, E. (1977). Bounds for efective elastic moduli of disordered materials. *Journal of the Mechanics and Physics of Solids*, 38:137–155.

Lebensohn, R., Rollett, A., and Suquet, P. (2011). Fast fourier transform-based modelling for the determination of micromechanical fields in polycrystals. *Journal of Materials*, 63:13–18.

Leblond, J., Perrin, G., and Suquet, P. (1994). Exact results and approximate models for porous viscoplastic solids. *International Journal of Plasticity*, 10(3):213–235.

Lee, J. and Oung, J. (2000). Yield functions and flow rules for porous pressure-dependent strain-hardening polymeric materials. *J.Appl.Mech.*, 67:288–297.

Lemaitre, J. and Desmorat, R. (2005). *Engineering Damage Mechanics: Ductile, Creep, Fatigue and Brittle Failures*. Springer-Verlag Berlin and Heidelberg GmbH & Co. KG.

Li, J., Tian, X. X., and Abdelmoula, R. (2012). A damage model for crack prediction in brittle and quasi-brittle materials solved by the fft method. *International Journal of Fracture*, 173:135–146.

Li, S. F. and Wang, G. (2008). *Introduction to Micromechanics and Nanomechanics*. World Scientific.

Maghous, S., Dormieux, L., and Barthèlèmy, J. (2009). Micromechanical approach to the strength properties of frictional geomaterials. *European Journal of Mechanics A/Solid*, 28:179–188.

Mazars, J. (1984). Application de la mécanique de l'endommagement au comportement nonlinéaire et à la rupture du béton de structure. *Thése de doctorat d'état de l'Université Paris VI*.

Michel, J. C., Moulinec, H., and Suquet, P. (1999). Effective properties of composite materials with periodic microstructure: a computational approach. *Computer Methods in Applied Mechanics and Engineering*, 172:109–143.

Michel, J. C., Moulinec, H., and Suquet, P. (2000). A computational method based on augmented lagrangians and fast fourier transforms for composites with high contrast. *Computer Modeling in Engineering and Sciences*, 1:79–88.

Michel, J. C., Moulinec, H., and Suquet, P. (2001). A computational scheme for linear and non-linear composites with arbitrary phase contrast. *International Journal for Numerical Methods in Engineering*, 52:139–160.

Michel, J.-C. and Suquet, P. (1992). The constitutive law of nonlinear viscous and porous materials. *Journal of the Mechanics and Physics of Solids*, 40:783–812.

Michel, J. C. and Suquet, P. (2003). Nonuniform transform field. *International Journal of Solids and Structures*, 40:6937–6955.

Michel, J. C. and Suquet, P. (2004). Computational analysis of nonlinear composite structures using the nonuniform transformation field analysis. *Computer Modeling in Engineering and Sciences*, 193:5477–5502.

Milton, G. W. (2002). *The Theory of Composites*. Cambridge University Press, Cambridge.

Monchiet, V. and Bonnet, G. (2012). A polarization-based fft iterative scheme for computing the effective properties of elastic composites with arbitrary contrast. *International Journal for Numerical Methods in Engineering*, 89:1419–1436.

Monchiet, V., Cazacu, O., Charkaluk, E., and Kondo, D. (2008). Macroscopic yield criteria for plastic anisotropic materials containing spheroidal voids. *International Journal of Plasticity*, 24:1158–1189.

Monchiet, V., Charkaluk, E., and Kondo, D. (2014). Macroscopic yield criteria for ductile materials containing spheroidal voids: An eshelby-like velocity fields approach. *Mechanics of Materials*, 72:1–18.

Mori, T. and Tanaka, K. (1973). Average stress in matrix and average elastic energy of materials with misfitting inclusions. *Acta Metallurgica*, 21:571–574.

Moulinec, H. and Silva, F. (2014). Comparison of three accelerated fft-based schemes for computing the mechanical response of composite materials. *International Journal for Numerical Methods in Engineering*, 97:960–985.

Moulinec, H. and Suquet, P. (1994). A fast numerical method for computing the linear and nonlinear mechanical properties of composites. *Comptes Rendus de l'Académie des Sciences*, t.318:1417–1423.

Moulinec, H. and Suquet, P. (1998). A numerical method for computing the overall response of nonlinear composites with complex microstructure. *Computer Methods in Applied Mechanics and Engineering*, 157:69–94.

Moulinec, H. and Suquet, P. (2003). Comparison of fft-based methods for computing the response of composites with highly contrasted mechanical properties. *Physica B*, 338:58–60.

Mura, T. (1987). *Micromechanics of defects in solids*. Martinus Nijhoff Publishers, Dordrecht, second, revised edition.

Nemat-Nasser, S. and Hori, M. (1999). *Micromechanics: Overall Properties of Heterogeneous Materials*. North-Holland Series in Applied Mathematics and Mechanics Series. Elsevier Science & Technology Books.

Nguyen, T. K., Sab, K., and Bonnet, G. (2008). Green's operator for a periodic medium with traction-free boundary conditions and computation of the effective properties of thin plates. *International Journal of Solids and Structures*, 45:6518–6534.

Niandou, H., Shao, J. F., Henry, J. P., and Fourmaintraux, D. (1997). Laboratory investigation of the mechanical behaviour of tournemire shale. *International Journal of Rock Mechanics and Mining Sciences*, 34:3–16.

Pardoen, T. andHutchinson, J. (2003). Micromechanics-based model for trends in toughness of ductile metals. *Acta Mater*, 51:133–148.

Pierard, O. and Doghri, I. (2006). A study of various estimates of the macroscopic tangent operator in the incremental homogenization of elastopplastic composites. *International Journal for Multiscale Computational Engineering*, 4:521–543.

Pietruszczak, S., Lydzba, D., and Shao, J. F. (2002). Modelling of inherent anisotropy in sedimentary rocks. *International Journal of Solids and Structures*, 39:637–648.

Ponte Castaneda, P. (1991). The effective mechanical properties of nonlinear isotropic composites. *J. Mech. Phys. Solids*, 39:45–71.

Ponte Castañeda, P. and Willis, J. R. (1995). The effect of spatial distribution of effective behavior of composite materials and cracked media. *Journal of the Mechanics and Physics of Solids*, 43:1919–1951.

Reuss, A. (1910). Berechnung der fließgrenze von mischkristallen auf grund der plastizitätsbedingung für einkristalle. *Journal of Applied Mathematics and Mechanics / Zeitschrift für Angewandte Mathematik und Mechanik*, 9:49–58.

Robinet, J. (2008). *Mineralogie, porosite et diffusion des solutes dans l'argilite du Callovo-Oxfordien de Bure (Meuse/Haute-Marne, France) de l'echelle centimetrique a micrometrique.* Phd, thesis, Université de poitiers, France.

Salager, S., François, B., and Nuth, M. Laloui, L. (2013). Constitutive analysis of the mechanical anisotropy of opalinus clay. *Acta Geotechnica*, 8:137–154.

Shao, J.-F., Jia, Y., Kondo, D., and Chiarelli, A.-S. (2006). A coupled elastoplastic damage model for semi-brittle materials and extension to unsaturated conditions. *Mech.Mater.*, 38(3):218–232.

Shen, W., He, Z., Dormieux, L., and Kondo, D. (2014a). Effective strength of saturated double porous media with a drucker-prager solid phase. *Int. J. Numer. Anal. Meth. Geomech.*, 38:281–296.

Shen, W., Lanoye, E., Dormieux, L., and Kondo, D. (2014b). Homogenization of saturated double porous media with eshelby-like velocity field. *Acta Geophysica.*, 62(5):1146–1162.

Shen, W., Lin, J., Zhu, Q., Monchiet, V., and Kondo, D. (2011). Macroscopic yield criterion for ductile materials containing randomly oriented spheroidal cavities. *International Journal of Damage Mechanics*, 20:1198–1216.

Shen, W., Oueslati, A., and De Saxce, G. (2015a). Macroscopic criterion for ductile porous materials based on a statically admissible microscopic stress field. *International Journal of Plasticity*, 70:60–76.

Shen, W., Pastor, F., and Kondo, D. (2013a). Improved criteria for ductile porous materials having a green type matrix by using eshelby-like velocity fields. *Theoretical and Applied Fracture Mechanics*, 67-68:14–21.

Shen, W., Shao, J., Dormieux, L., and Kondo, D. (2012a). Approximate criteria for ductile porous materials having a green type matrix: Application to double porous media. *Computational Materials Science*, 62:189–194.

Shen, W., Shao, J., Kondo, D., and De Saxce, G. (2015b). A new macroscopic criterion of porous materials with a mises-schleicher compressible matrix. *European Journal of Mechanics A/Solids*, 49:531–538.

Shen, W., Shao, J., Kondo, D., and Gatmiri, B. (2012b). A micro-macro model for clayey rocks with a plastic compressible porous matrix. *International Journal of Plasticity*, 36:64–85.

Shen, W. Q., Kondo, D., Dornieux, L., and Shao, J. F. (2013b). A closed-form three scale model for ductile rocks with a plastically compressible porous matrix. *Mechanics of Materials*, 59:73–86.

Shen, W. Q., Shao, J. F., Kondo, D., and Gatmiri, B. (2012c). A micro-macro model for clayey rocks with a plastic compressible porous matrix. *International Journal of Plasticity*, 36:64–85.

Sun, Y. and Wang, D. (1989). A lower bound approach to the yield loci of porous materials. *Acta Mech.*, 5:237–243.

Suquet, P. (1995). Overall properties of nonlinear composites: a modified secant moduli theory and its link with ponte castaneda's nonlinear variational procedure. *Comptes Rendus de l'Académie des Sciences*, IIb:563–571.

Suquet, P. (1996a). Overall properties of nonlinear composites: Remarks on secant incremental formulations. In Pineau, A. and Zaoui, A., editors, *Micromechanics of Plasticity and Damage of Multiphase Materials*, pages 149–156. Kluwer Academic Publishers.

Suquet, P. (1996b). Overall properties of nonlinear composites: Secant moduli theories and variational bounds. In Markov, K., editor, *Continuum Models of discrete systems 8*, pages 290–299. World Scientific.

Tvergaard, V. (1981). Influence of voids on shear bands instabilities under plane strain conditions. *Int. J. Fracture*, 17:389–407.

Tvergaard, V. (1982). Material failure by void coalescence in localized shear bands. *Int. J. Solids Structures*, 18(8):659–672.

Voigt, W. (1889). Ueber die beziehung zwischen den beiden elasticitätsconstanten isotroper körper. *Annalen der Physik*, 274:573–587.

Appendix A

Green's function G^0 and operator Γ^0

A.1 Green's function G^0

The Green's function, $G_{ij}(x,x')$, is interpretated as the displacement in the ith direction at x generating from a point force in the jth direction at x' where the point force is represented by a delta function, $\delta_{ij}\delta(x-x')$.

As is known that the Green's function in a uniform elastic domain Ω satisfies the equilibrium equation pointwisely,

$$C^0_{ijkl}G_{kp,lj}(x,x') + \delta_{ip}\delta(x-x') = 0, \quad \forall x \in \Omega \tag{A.1}$$

The polarization field can be considered as a point force with a magnitude $\tau_{pq,q}$ somehow applying in the whole filed Ω, therefore, the idea of making use of this pointwise equation to resolve the second problem proposed in (2.16) is to integral this equation in the whole filed Ω .

Multiplying $\tau_{pq,q}$ the equation (A.1) and integraling x' in the field Ω takes the form

$$\int_\Omega (C^0_{ijkl}G_{kp,lj}(x,x') + \delta_{ip}\delta(x-x'))d\Omega = 0, \quad \forall x \in \Omega \tag{A.2}$$

Assuming $\tau_{pq,q}(x') = F_p(x')$ and the three dimension Dirac delta function is defined as

$$\int_\Omega \delta(x-x')d\Omega = \begin{cases} 1 & if\ x' \in \Omega \\ 0 & if\ x' \notin \Omega \end{cases} \tag{A.3}$$

The equation is simplified as

$$\int_\Omega C^0_{ijkl} G_{kp,lj}(x,x') F_p d\Omega + F_i = 0, \quad \forall x \in \Omega \tag{A.4}$$

Using Green's theory on the first term

$$\int_{\partial\Omega} C^0_{ijkl} G_{kp,l}(x,x') n_j F_p d\Omega + F_i = 0, \quad \forall x \in \Omega \tag{A.5}$$

If the body encloses the point x', then the force F must be balanced by the traction on the surface S and leads

$$\sigma_{ij}(x) = \int_\Omega C^0_{ijkl} G_{kp,l}(x,x') F_p d\Omega, \tag{A.6}$$

and the strain field can be then determined by Hook's law

$$\varepsilon_{ij}(x) = \int_\Omega G_{kp,l}(x,x') F_p d\Omega, \tag{A.7}$$

and the displacement is thus

$$u_i(x) = \int_\Omega G_{ip}(x,x') \tau_{pq,q}(x') d\Omega, \tag{A.8}$$

A.2 Green's operator Γ^0

As stated previously, according to the properties of the Fourier transform, the problem (2.15) can be transformed into the Fourier spaces correspondingly:

$$\begin{cases} \hat{\sigma}_{ij}(\xi) = i C^0_{ijkl} \xi_h \hat{u}^*_k(\xi) + \hat{\tau}_{ij}(\xi) \\ i \hat{\sigma}_{ij}(\xi) \xi_j = 0 \end{cases} \tag{A.9}$$

and the strain-displacement relation takes the form in Fourier space:

$$\hat{\varepsilon}_{kh}(\xi) = \frac{i}{2}(\xi_h \hat{u}^*_k(\xi) + \xi_k \hat{u}^*_h(\xi)). \tag{A.10}$$

where ξ is the coordinates in Fourier spaces, and the subscript i is different from the complex number $i = \sqrt{-1}$.

Combine the two equations of (A.9) to eliminate the stress term $\hat{\sigma}_{ij}$:

$$\begin{aligned} i\hat{\sigma}_{ij}(\boldsymbol{\xi})\xi_j &= i\xi_j(iC^0_{ijkh}\xi_h\hat{u}^*_k(\boldsymbol{\xi}) + \hat{\tau}_{ij}(\boldsymbol{\xi})) \\ &= -C^0_{ijkh}\xi_h\xi_j\hat{u}^*_k(\boldsymbol{\xi}) + i\hat{\tau}_{ij}(\boldsymbol{\xi})\xi_j \\ &= -K^0_{ik}(\boldsymbol{\xi})\cdot\hat{u}^*_k + i\hat{\tau}_{ij}(\boldsymbol{\xi})\xi_j, \end{aligned} \tag{A.11}$$

where $K^0_{ik}(\boldsymbol{\xi}) = C^0_{ijkh}\xi_h\xi_j$, which denotes the acoustic tensor of the homogeneous medium. As is known $i\hat{\sigma}_{ij}(\boldsymbol{\xi})\xi_j = 0$, the right side of the equation gives:

$$K^0_{ik}(\boldsymbol{\xi})\cdot\hat{u}^*_k = i\hat{\tau}_{ij}(\boldsymbol{\xi})\xi_j, \tag{A.12}$$

then

$$\hat{u}^*_k = iN^0_{ki}(\boldsymbol{\xi})\hat{\tau}_{ij}(\boldsymbol{\xi})\xi_j, \tag{A.13}$$

where $N^0(\boldsymbol{\xi})$ denotes the inverse of $K^0(\boldsymbol{\xi})$. Considering the symmetry of $\boldsymbol{\tau}$, which makes $iN^0_{ki}\hat{\tau}_{ij}\xi_j = iN^0_{kj}\hat{\tau}_{ji}\xi_i$, therefore, $\hat{u}^*$ takes form:

$$\hat{u}^*_k = \frac{i}{2}(N^0_{ki}(\boldsymbol{\xi})\xi_j + N^0_{kj}(\boldsymbol{\xi})\xi_i)\hat{\tau}_{ij}(\boldsymbol{\xi}), \tag{A.14}$$

then substitute $\hat{u}^*_k$ into equation (A.10) then

$$\begin{aligned} \hat{\varepsilon}_{kh}(\boldsymbol{\xi}) &= \frac{i}{2}(\xi_h\hat{u}^*_k + \xi_k\hat{u}^*_h) \\ &= \frac{i}{2}(\xi_h\cdot\frac{i}{2}(N^0_{ki}(\boldsymbol{\xi})\xi_j + N^0_{kj}(\boldsymbol{\xi})\xi_i)\hat{\tau}_{ij} + \xi_k\cdot\frac{i}{2}(N^0_{hi}\xi_j(\boldsymbol{\xi}) + N^0_{hj}(\boldsymbol{\xi})\xi_i)\hat{\tau}_{ij}) \\ &= -\frac{1}{4}(N^0_{hi}(\boldsymbol{\xi})\xi_j\xi_k + N^0_{ki}(\boldsymbol{\xi})\xi_j\xi_h + N^0_{hj}(\boldsymbol{\xi})\xi_i\xi_k + N^0_{kj}(\boldsymbol{\xi})\xi_i\xi_h)\hat{\tau}_{ij} \\ &= -\Gamma^0_{khij}(\boldsymbol{\xi})\hat{\tau}_{ij}(\boldsymbol{\xi}), \end{aligned} \tag{A.15}$$

where

$$\Gamma^0_{khij}(\boldsymbol{\xi}) = \frac{1}{4}(N^0_{hi}(\boldsymbol{\xi})\xi_j\xi_k + N^0_{ki}(\boldsymbol{\xi})\xi_j\xi_h + N^0_{hj}(\boldsymbol{\xi})\xi_i\xi_k + N^0_{kj}(\boldsymbol{\xi})\xi_i\xi_h), \tag{A.16}$$

and

$$\hat{\tau}_{ij}(\boldsymbol{\xi}) = < \tau_{ij}(\boldsymbol{x})e^{-i\xi x} >, \tag{A.17}$$

where the polarization field $\tau(\boldsymbol{x})$ is transformed as $\hat{\tau}(\boldsymbol{\xi})$ in Fourier space according to the definition of Fourier transform (see equation (2.1)) at each point $\boldsymbol{x}$ of the

R.V.E. With the explicit form of Γ^0 the problem then can be solved in Fourier space, whereafter, the resolution of the auxiliary problem can be obtained by the inverse Fourier transform.

As stated above, the Green's operator can be determined explicitly based on the properties of the reference material. If the reference medium is simply isotropic with Lamé coefficients λ^0 and μ^0, the stiffness tensor $\mathbb{C}^0$ can be expressed in the form

$$C^0_{ijkh} = \lambda^0 \delta_{ij}\delta_{kh} + \mu^0(\delta_{ik}\delta_{jh} + \delta_{ih}\delta_{jk}), \tag{A.18}$$

therefore, the analytical form of Green's operator in Fourier space becomes

$$\hat{\Gamma}_{khij}(\boldsymbol{\xi}) = \frac{1}{4\mu^0|\boldsymbol{\xi}|^2}(\delta_{ki}\xi_h\xi_j + \delta_{hi}\xi_k\xi_j + \delta_{kj}\xi_h\xi_i + \delta_{hj}\xi_k\xi_i) - \frac{\lambda^0+\mu^0}{\mu^0(\lambda^0+2\mu^0)}\frac{\xi_i\xi_j\xi_k\xi_h}{|\boldsymbol{\xi}|^4}. \tag{A.19}$$

Appendix B

Further discussion on effects of porosity on porous materials

B.1 Void shape effects with different volume fraction

The effect of void shape is taking into consideration on the attributes of the present method handling with microstructures. A modified Drucker-Prager criterion is studied to model a pressure sensitive matrix material with an isotropic hardening and takes the form of the yield criterion (Guo et al., 2008):

$$\sigma_{eq} + 3\alpha\sigma_m = \sigma_0 + H\gamma^m, \tag{B.1}$$

where σ_{eq} is the effective stress and σ_0 is the mean stress. σ_0 is the initial yield stress with the hardening modulus H and hardening variables γ (refer to previous section), and α relates to the friction angle ψ by

$$tan\psi = 3\alpha, \tag{B.2}$$

and α controls the pressure sensitivity. The Young's modulus are chosen by a constant ratio with initial yield stress $E/\sigma_0 = 0.0045$ and Poisson ratio is $\nu = 0.25$. The friction angle ψ and initial yield stress $\sigma_0$are chosen 17^o and $45MPa$, respectively. A power law with a constant hardening modulus H is introduced as $150MPa$ with $m = 0.3$.

A set of examples taking into account the void shape is performed based on these material parameters and uniaxial tension tests are applied. The curves of

the effective strain (E_e) and the normolized effective stress (Σ_e/σ_0) for pore volume fraction from 0.001 to 0.3 are shown in Fig. B.1 and three shapes of void are considered *i.e.* sphere, prolate and oblate (Fig. 5.9). The figure shows the influence of void shape highly depends on the pore volume fraction and the effect of void shape is considerable for the higher value of volume fraction. The spherical void provides much stiffer effective properties than the oblate one but more compliant than the prolate one. The figure shows the effect of void shape is gradually enhanced with the augment of the void volume fraction.

B.2 Effects of random distributed voids with different volume fraction

The void distribution is also investigated with the same assumption for the solid matrix, in other words, it is assumed to be the pressure sensitive with the modified Drucker-Prager criterion with isotropic hardening. The material parameters are remain the same and uniaxial tension tests are performed for void volume fraction f from 0.001 to 0.3. The microstructures simulated is referred to Fig. 5.4 and the number of inclusions are set to be 40. To be specific the prolate void has two types of distributions, the first one is that the orientation of their major-axes are uniform along the third direction (loading path) and the second one is that their orientations are randomly distributed. The curves of the effective strain and normalized effective stress are shown in Fig. B.2. It is shown that the effective properties of spherical voids are much stiffer than that of the oblate ones and the prolate void material gives much stiffer than spherical and oblate ones. It is noted that the prolate with random direction is more compliance than the ones with uniform direction. The figure shows also that the pore volume fraction has significant influence on the effects of void distributions.

B.3 Distributions of microscopic variables

As full field simulation the FFT method is powful to display the microscopic variables on the entire field in details. The material parameters are remain the same as aforementioned and the void volume fraction is chosen $f = 0.1$. Two uniaxial tension tests are employed to examine the distributions of microscopic variables.

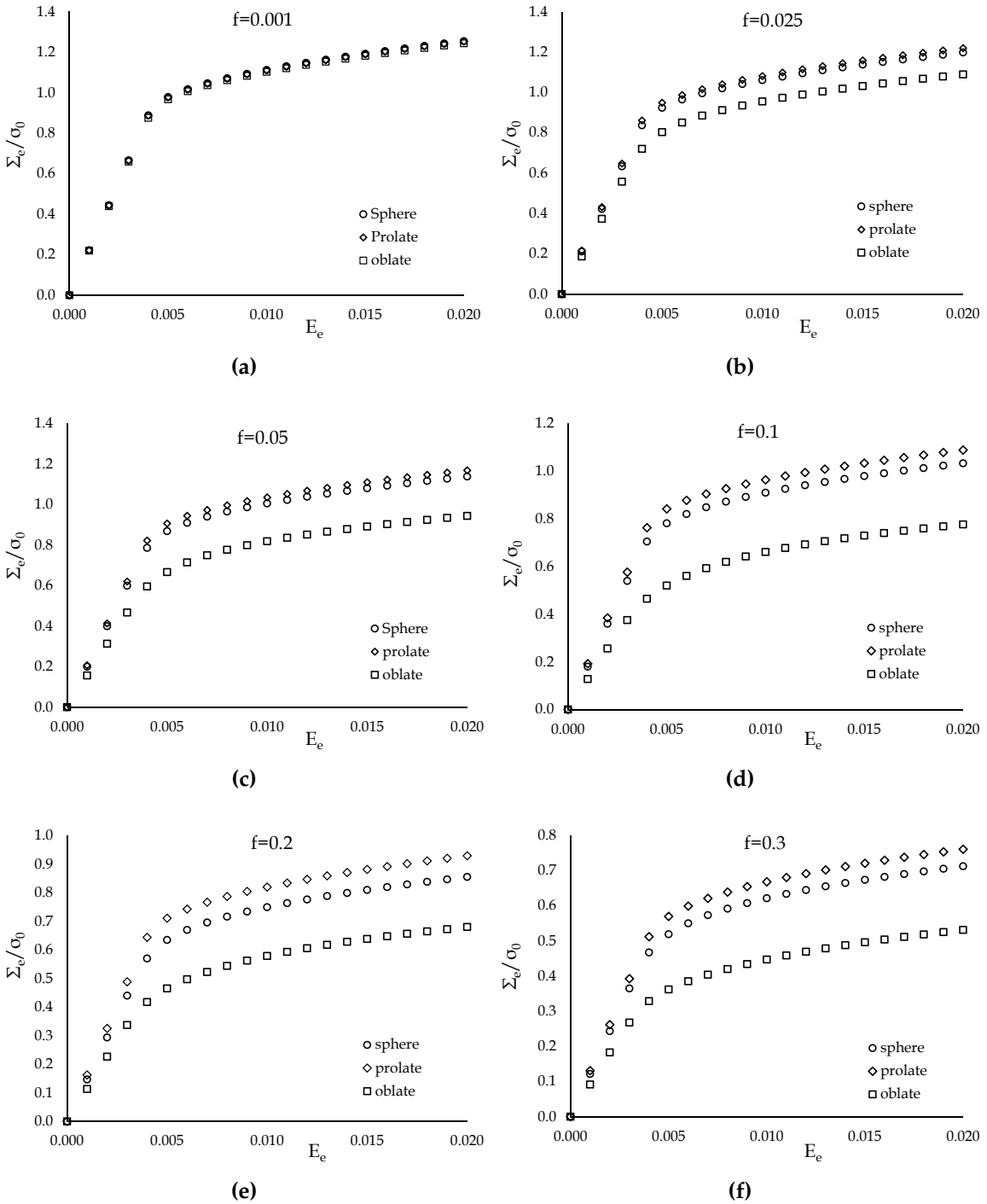

Fig. B.1 Effective strain vs effective stress curves illustrating the effects of void shape on different volume fraction under uniaxial tension. (a) $f = 0.001$; (b) $f = 0.025$; (c) $f = 0.05$; (d) $f = 0.1$; (e) $f = 0.2$; (f) $f = 0.3$. Circle line: sphere; diamond line: prolate; square line: oblate.

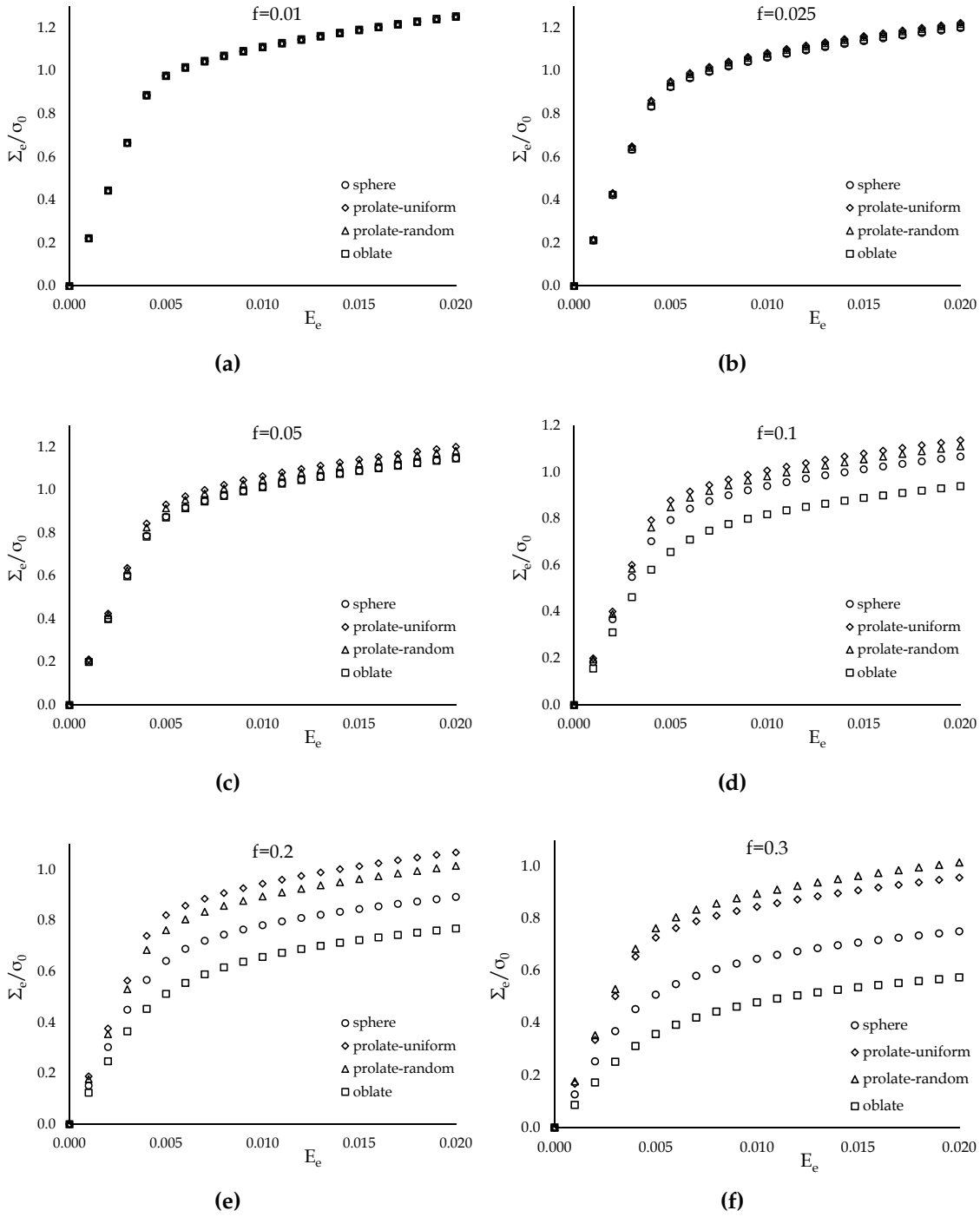

Fig. B.2 Effective strain vs effective stress curves displaying the effects of void shape with random distributions on different volume fraction under uniaxial tension. (a) $f = 0.001$; (b) $f = 0.025$; (c) $f = 0.05$; (d) $f = 0.1$; (e) $f = 0.2$; (f) $f = 0.3$. Circle line: sphere; diamond line: prolate with uniform orientation; triangle line: prolate with random orientation; square line: oblate with random orientation.

The fist study considers the influence of the number for the spherical void and the comparison is implemented for $N = 40$ and $N = 100$. The second study investigates the effects of the void shape and arrangement, and the void number is $N = 100$ for all tests. Fig. B.3 shows the microscopic stress σ_{33} distributions of porous materials with randomly scattered pores for the same pore volume fraction on the loading direction. The left one (Fig. B.3a) studied 40 randomly spherical pores with uniform radium $R = 0.08$ and the right one (Fig. B.3b) examines 100 randomly spherical voids with uniform radium $R = 0.06$. It is noted that the regions with highly concentration (dark orange) are the pore parts and the stress values are shown from the color scale that no stress possesses. The boundaries of voids clearly exhibit stress concentrations and the stress interactions between nearby pores are noticeably observed. Prolate and oblate voids with randomly arrangement and orientation are studied in Fig. B.4. It shows that the microscopic stress distributions are becoming more interacted with the complexity of microstructures. The distributions of the Fig. B.4a and B.4b are quite similar but the randomness of the orientation of the voids creates more interactions and the stress concentrations appears much more. The case with oblate voids with random orientation shown in Fig. B.4c reproduces much more stress concentration such that the stresses in the whole field are more uniform and the color exhibits that the average value is smaller than the former two cases. It explains the results of the effects of void shape aforementioned that the oblate case provides much compliant effective properties. It is worthy mentioning that such sort of complex microstructures are intractable for the FEM simulations and the computational cost might be very high to have a refine mesh for such complexity.

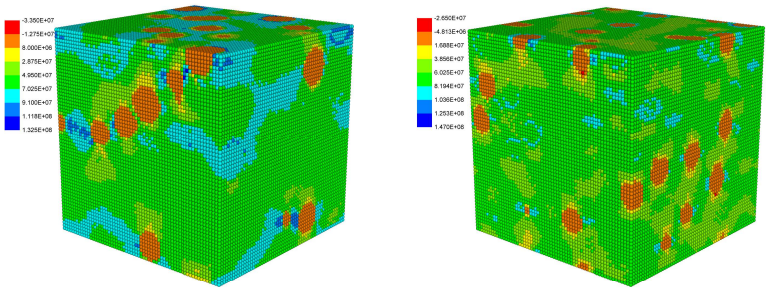

(a) (b)

Fig. B.3 Microscopic stress σ_{33} (loading path) distributions of porous materials with different size R, number N and distribution of voids for pore volume fraction $f = 10\%$.(a) $N = 40$, $R = 0.08$; (b) $N = 100$, $R = 0.06$.

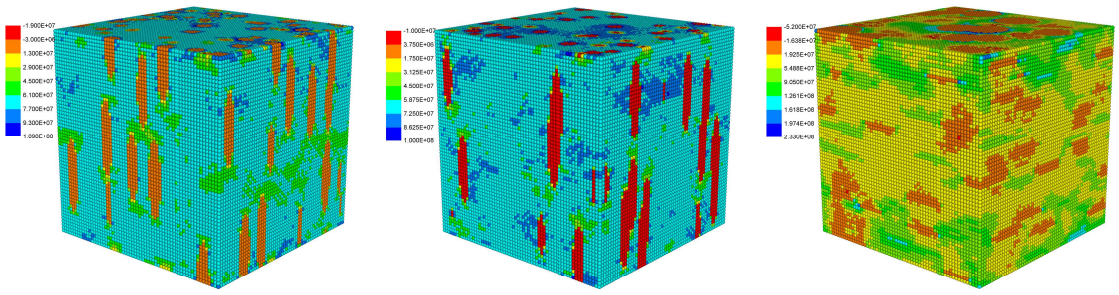

(a) (b) (c)

Fig. B.4 Microscopic stress σ_{33} (loading path) distributions of porous materials with different randomly distributed shapes and different orientations of voids for pore volume fraction $f = 10\%$.(a) prolate pores with uniform orientations; (b) prolate pores with random orientations; (c) oblate pores with random orientations.